Active River Area (ARA) Framework Refinement: Developing Frameworks for Terrace and Meander Belt Delineation and Defining Optimal Digital Elevation Model for Future ARA Delineation

by

Shizhou Ma

Submitted in partial fulfilment of the requirements
for the degree of Master of Environmental Studies

at

Dalhousie University
Halifax, Nova Scotia
August 2020

Table of Contents

List of Tables

List of Figures

Abstract

The Active River Area (ARA) is a spatial approach for identifying the extent of functional riparian areas, with five components (floodplains, terraces, riparian wetlands, meander belts, material contribution zones). Given the limitations in terms of input data quality and methodology, this framework cannot specifically differentiate terraces from floodplains and identify the river meander extent. To address these limitations in the ARA framework, this study developed a floodplain and terrace separation framework and a meander belt delineation framework. Their applicability was tested in two study watersheds in New Brunswick. Moreover, to determine the optimal input DEM for future ARA studies, this study developed an accuracy-efficiency tradeoff analysis framework and assessed ARA outputs derived from a range of DEM inputs for accuracy and efficiency. It has been found that 5-m smoothed LiDAR DEM is best able to balance final ARA accuracy and data processing efficiency and ultimately recommended for future ARA delineations.

List of Abbreviations Used

ARA	Active River Area
AMSL	Above Mean Sea Level
CART	Classification and Regression Tree
CHU	Canadian Hydrological Unit
DEM	Digital Elevation Model
DNR	Department of Nature Resources
DSM	Digital Surface Model
ELG	Department of Environment and Local Government
ERD	Department of Energy and Resource Development
FPDEMS	Feature Preserving DEM Smoothing algorithm
GCP	Ground Control Point
GIS	Geographic Information System
LiDAR	Light Detection and Ranging
MCL	Meander Centerline
MCZ	Material Contribution Zone
ME	Mean Error
NBHN	New Brunswick Hydrographic Network
NED	National Elevation Datasets
NHD	National Hydrologic Dataset
NHN	National Hydrology Network
NCC	Nature Conservancy of Canada
RMSE	Root Mean Square Error
SGS	Sequential Gaussian Simulation
SNB	Service New Brunswick
SRTM	Shuttle Radar Topography Mission
TMI	Topography Moisture Index
TNC	The Nature Conservancy
TIN	Triangulated Irregular Network
USGS	United States Geological Survey

Acknowledgements

First and foremost, I would like to express my deepest gratitude to my supervisor Dr. Karen Beazley, for her continuous support and guidance throughout the production of this thesis. Over the past two years, Karen has provided irreplaceable support on my research and thesis writing. I cannot imagine how I would have struggled to finish the MES program within the two-year time frame without her help.

I am also grateful to my committee member Patrick Nussey from the Nature Conservancy of Canada for introducing me this interesting research project and sharing invaluable perspectives throughout my thesis research process. Meanwhile, I must thank the other committee member Chris Greene for helping me build important data processing skills and providing thoughtful refinement advice on my thesis drafts. Special thanks should also go out to my external examiner Arlene Olivero from The Nature Conservancy, for reviewing this thesis.

I would also like to extend my appreciation to Dalhousie Faculty of Graduate Studies for providing the financial support and the essential data processing software.

Finally, I want to thank my parents for providing irreplaceable love and encouragement from China. Their love and comfort were really important to me.

Chapter 1. Introduction

1.1. Motivation

Riparian areas are the interface between aquatic and terrestrial systems along inland watercourses (Naiman & Décamps, 1997). These areas cover a small proportion of the landscape mosaic but play important roles in both terrestrial and aquatic ecosystems. Riparian plant communities support numerous functions including sediment deposition on floodplains and woody debris supply, which has an influence on channel complexity and instream habitat features (NRC, 2002). Ecologically intact riparian areas naturally retain and recycle energy and organic materials and sustain broadly based riparian food webs which help support a diverse assemblage of aquatic and riparian species (NRC, 2002; Smith et al., 2008). The movement of water and the associated movement of sediment, energy and other organic materials within riparian areas makes freshwater ecosystems one of the most biologically diverse and rich systems in the world (Master et al., 1998; Smith et al., 2008).

Riparian areas are some of the most degraded ecosystems worldwide (Nilsson & Berggren, 2000). The effects of human activities on riparian areas range from changes in the hydrologic regime to the removal of vegetation (NRC, 2002). The construction of dams, levees and culverts disconnects rivers from their floodplains, leading to the disruption of physical and ecological processes. More than 3,700 hydropower dams are currently planned or under construction all over the world (Zarfl et al., 2005). Several countries (e.g. China, India, etc.) are planning and/or building extensive inland water-transfer schemes, which require river channelization and the installation of culverts and

dams (Shumilova et al., 2018). The alteration of streamside vegetation due to agriculture, grazing, and urbanization removes the binding effect of roots upon the soil and causes an increase in flow velocities near the bank (NRC, 2002). Such alterations lead to accelerated channel erosion during subsequent periods of high flow.

Given the important role of riparian areas in both terrestrial and aquatic ecosystems and the degradation caused by human disturbances, effective riparian conservation is warranted and should include the conservation and restoration of physical and ecological processes of the river and its adjacent land area (Dorren et al., 2004; Smith et al., 2008). The initial stage of effective riparian conservation and restoration is to define and delineate the extent of functional riparian area, which is important for both ecological and managerial reasons (Naiman & Décamps 1997; Ilhart et al., 2000). By understanding the extent of the riparian area and how the river interacts with these adjacent lands, planners and managers can better recognize the processes involved with protection and restoration efforts and how to design these efforts to more effectively conserve the physical and ecological processes within riparian areas (Smith et al., 2008).

The Active River Area (ARA) framework, developed by The Nature Conservancy (TNC) in 2008 (Smith et al., 2008), offers a lens through which conservation planners can effectively define and delineate functional riparian areas. To facilitate spatially-explicit delineation of key riparian areas within which physical and ecological processes take place, the framework separates the active river area into five components based on the valley setting and geomorphic stream type: floodplain, terrace, meander belt, riparian wetland, and material contribution zone (Smith et al., 2008). Accurate and timely delineation of these key active river areas is critical to effective planning and

management to protect and conserve ecological structures and processes as well as human infrastructure and activities within and adjacent riparian areas (Naiman & Décamps, 1997; Smith et al., 2008). Attention to active river area conservation and management is increasingly important with continued human encroachments into riparian landscapes and increased frequency and severity of floods and other events related to climate changes.

1.2. Problem to be Addressed

Among the five ARA components, floodplains, terraces and meander belts together cover significant part of a river valley and each plays a key role in maintaining river health through the dynamic hydrological exchange of energy and organic materials between river flows and riparian corridors (Bridge, 2003; Harvey and Gooseff, 2015). Floodplains and terraces play distinct roles in terms of channel width adjustment and sediment source-to-sink dynamics and have long been altered by human activities (i.e. agriculture and urban development) because of their relatively flat surfaces and proximity to rivers (Yan et al., 2017). The analysis of regional terrace development and preservation can provide insight into historic and contemporary sediment routing through channel-floodplain networks (Stout and Belmont, 2014). Distinguishing these two components is important but challenging to accomplish. Measurements in the field are time and resource intensive and often unfeasible over large regions. As a consequence, the development of methods for identifying them using elevation data is being explored (Stout and Belmont, 2014; Yan et al., 2017). Scientists have tried to differentiate terraces from modern floodplains with the aid of Shuttle Radar Topography Mission (SRTM) Digital Elevation

Model (DEM) data (Burns et al., 2012; Su et al., 2010; Marangelo et al., 2010), however the commonly used 10-m and 30-m SRTM DEM data appear to be too coarse in spatial resolution to delineate terraces with confidence (Marangelo and Farrell, 2010). Increasingly fine spatial resolution data are becoming available for some regions (e.g., Light Detection and Ranging (LiDAR)-derived DEM data as fine as 1-m resolution) and may prove to be more useful than the previously described data. To date, such fine-resolution data have not been applied to terraces and floodplain separation in ARA studies, and thus the optimal spatial resolution of elevation data for confidently differentiating terraces from floodplains while achieving high computational efficiency remains unclear. Without such clarification, an effective method for delineating and distinguishing floodplains and terraces remains elusive, and as such, the efficacy of ARA framework is limited (Marangelo and Farrell, 2010; Nussey and Noseworthy, 2020).

For decades the quantification of the extent of the meander belt has been considered a major challenge in the field of fluvial geomorphology (Howett, 2017). Meander belts are the most active part of the active river area (Smith et al., 2008), and any landscape features situated within its extent may be subject to erosion by the channel (Parish Geomorphic, 2004). Accordingly, the width of meander belts should be accurately delineated to inform the extent of fluvial erosion processes for conservation and hazards management practices (Kline and Dolan, 2008). Unfortunately, standardized means of accurate delineation are difficult to derive because of the dynamic and diverse range of meander belt widths along and between river systems. Although the ARA framework includes the meander belt as a key ARA component, no ARA studies to date have attempted to delineate their extent, as there is no existing standard or ARA-specific

assessment tool (Marangelo and Farrell, 2010). Accordingly, an effective method for accurate quantification of the extent of meander belt also remains elusive, and further limits the efficacy of ARA framework and its application across broad landscapes and regions.

The most extensive application of the ARA framework application to date was conducted by TNC scientists for the Northern Appalachian Ecoregion in the northeastern United States of America (USA) (TNC, 2015). Although laudable for its application of key ARA components across a larger geographic area, its limitations in terms of accuracy and confidence in riparian basezone (i.e. floodplain, terrace and meander belt) delineation are acknowledged (Smith et al., 2008; Marangelo and Farrell, 2010). Refinements of methods and data spatial resolution for delineating these components are required for more precise application in the Northern Appalachian Ecoregion and other geographies. More specifically, the Nature Conservancy of Canada (NCC) is undertaking a process of extending the application of the ARA framework into the Canadian portion of the ecoregion in which it was applied in the USA (i.e. Northern Appalachian Ecoregion). In Canada, it is referred to as the Acadian Ecoregion, encompassing Nova Scotia, New Brunswick, Prince Edward Island, and parts of southern Quebec. The ARA framework represents an ecologically representative means of delineating important riparian components for planning purposes related to conservation and hazard management. For its effective refinement and application across these and other large geographical settings, the development of accurate and reliable, yet time and resource efficient, methods and data for distinguishing floodplains from terraces and delineating meander belts are required.

1.3. Research Questions and Objectives

The goal of this thesis is to contribute to the refinement of methods for applying the ARA framework across large (eco-) regions by addressing methodological and data spatial resolution limitations in ARA delineation. These refinements should benefit future applications of the ARA delineation process in the Acadian Ecoregion of southeastern Canada and in other geographic regions with similar characteristics. To achieve this goal, two study areas in New Brunswick were chosen as pilot watersheds based on data availability and their representative topographical characteristics. Through test applications in these watersheds the following three research questions will be addressed:

1) Is there a generalizable way to explicitly differentiate terraces from modern floodplains based on high spatial resolution DEM data (i.e. LiDAR-derived DEM)? If so, which LiDAR-derived DEM resolution can allow the user to confidently differentiate terraces from modern floodplains?
2) Is there a generalizable way to explicitly define and characterize the lateral extent of meander belts?
3) Does LiDAR-DEM data perform better than SRTM-DEM data in terms of ARA delineation? If so, what is the optimal input LiDAR-DEM spatial resolution, with respect to efficacy, computational intensity and final output accuracy, for the ARA delineation?

To answer these three research questions, the following five sub-objectives will be achieved:

1) Develop ARA-based method for terrace and floodplain separation, to be tested in two pilot watersheds in New Brunswick to see whether high-spatial resolution

LiDAR DEM can allow users to confidentially separate the terrace from floodplain;

2) Delineate the extent of the ARA components based on the standard ARA methods for riparian basezone (i.e. floodplain and terrace), riparian wetland and material contribution zone with the aid of multi-resolution LiDAR DEM (i.e. 3-, 5-, 10-, 15-, 30-m), 30-m SRTM-DEM, and 1:10,000 New Brunswick Hydrographic Network (NBHN) in two pilot watersheds in New Brunswick;
3) Compare the ARA results derived from LiDAR-DEMs and 30-m SRTM DEM (based on 1:10,000 NBHN) with each other and to those derived from 30-m SRTM-DEM and 1:50,000 National Hydrology Network (NHN) as provided by NCC to identify similarities and differences in terms of their area and spatial extent;
4) Develop ARA-based method for meander belts delineation, to be tested in two pilot watersheds in New Brunswick; and,
5) Identify optimal DEM for future applications of the ARA framework across broad regions based on output accuracy and data processing effort (e.g., computational time and power).

1.4. Context

Based on the ARA conceptual framework, TNC has created a ARA assessment tool designed for Geographic Information Systems (GISystems) and applied this tool to delineate the active river area for the entire eastern portion of the United States based on 30-m and 10-m SRTM DEM data and 1:100, 000 National Hydrologic Dataset (NHD)

(TNC, 2015). In order to make the extent of active river area available for the entire eastern portion of North America and benefit the regional riparian and freshwater conservation planning, scientists from NCC have replicated their work for the active river area delineation across the Acadian Ecoregion based on 30-m SRTM DEM and 1:50,000 NHN (Nussey and Noseworthy, 2020). Despite this progress, both TNC and NCC acknowledge limitations to these assessments, associated with spatial resolution of the data, and other methodological challenges, as introduced in section 1.2. Nonetheless, several TNC Chapters in the U.S. have applied the ARA framework as part of their local conservation planning (Marangelo and Farrell, 2010; Kusnierz et al., 2010). Despite limitations of the tool, they have found it useful for identifying and prioritizing aquatic systems and adjoining lands that support healthy river processes, for more effective riparian conservation and restoration practices. The Vermont chapter of TNC worked with conservation partners in the Lewis Creek Watershed to address conservation needs for riparian management (Marangelo and Farrell, 2010). The Maine Chapter and their local partners identified priority areas for regional riparian ecosystem conservation and restoration throughout the Penobscot River Watershed (Kusnierz et al., 2010). Refinements to TNC's spatial ARA assessment tool will further support accuracy and confidence in the modelled outputs for application in riparian conservation and management contexts.

1.5. Active River Area Conceptual Framework

As described by Naiman et al. (1993), riparian conservation based on isolated components (e.g. restoration of specific stream sections) is ecologically incomplete.

Consideration must be given to maintaining energy and sediment movement and inner variabilities of riparian corridors along the river network. Without the protection and restoration of key physical and ecological processes and their containing areas, efforts to protect riparian areas are likely to fall short of their goals and expectations (Smith et al., 2008). By explicitly considering processes such as hydrological connectivity and sediment movement along the river corridor, the ARA framework identifies key places where these processes occur: floodplains, terraces, riparian wetlands, meander belts, and material contribution areas (Smith et al., 2008). Each of these five ARA components play an independent role in terms of maintaining hydrological connectivity and sediment transportation in active river areas.

1) Floodplains are generally expansive and low slope areas, often with multiple channels and deep deposits of sediments and other organic materials (Smith et al., 2008). Lateral and vertical connectivity between the channel and floodplain has a strong influence on hydrological connectivity and sediment regimes both within the river and on the floodplain. High connectivity leads to regular floodplain inundation, which is an important process that determines flood water, sediment and organic material storage, transportation regimes, and nutrient uptake (Noe and Hupp, 2005).
2) Terraces are former floodplains from when the river was flowing at higher levels (Ward 2002; Stout and Belmont, 2014). These features are typically formed of deposited materials from large landscape events such as uplift or glacial retreat (Stout and Belmont, 2014). Terraces provide important roles in temporarily storing waters during very large flood events (Smith et al., 2008), and in response

to unique environmental conditions that influence sediment and water fluxes (Anderson and Anderson, 2010). Terraces may collapse and deliver sediment to the channel when flood waters undermine the base, resulting in widespread channel adjustment (Smith et al., 2008).

3) Riparian wetlands are generally low-gradient areas with inundated or hydric soils that support wetland plant species, and thus they are typically areas of high groundwater level and plant diversity (Smith et al., 2008). In the upper watershed, riparian wetlands are common in the broad, flat headwater areas and can serve as important retention and source areas of water, sediment and organic materials for downstream reaches (Smith et al., 2008). With their typically larger sizes in the lower watershed, riparian wetlands can perform substantial water, sediment and woody debris storage outside of the channel (Smith et al., 2008).
4) Meander belts are the areas where river channels migrate or meander over time as influenced by erosion and sediment deposition (Smith et al., 2008). Continuous erosion and deposition lead to the movement of water, sediment and other organic materials across meander belts as well as in the vertical direction relative to the level of the floodplains (Smith et al., 2008).
5) Material contribution zones (MCZs) refer to the headwater and certain upland and steep slope areas directly adjacent to the stream channels. These areas are neither floodplains nor riparian wetlands but still actively contribute to river systems through erosion and input of large woody debris and other organic materials, which deeply influence hydrology connectivity and channel structure (Smith et al., 2008).

These five ARA components often overlap and interact with each other (Smith et al., 2008). For example, many floodplains include riparian wetlands and meander belts often overlap areas of low floodplains. The lower watershed generally responds to upstream riparian wetlands input of water, sediment and debris via extensive floodplain inundation and sediment storage (Smith et al., 2008). Such overlaps and interactions allow active transport and exchange of energy and organic materials among different ARA components and ultimately contribute to diverse riparian functions (Smith et al., 2008). Thus, the key to functional riparian conservation is to explicitly restore and conserve the status and function of the various ARA components and maintain the linkages among the components. The ARA framework supports functional riparian conservation planning by providing a visualization of the riparian area as an interconnected system and highlighting where and how key physical and ecological processes occur within riparian areas (Smith et al., 2008). Such outputs that show the spatial extent of the five key riparian components delineated by applying the ARA framework can guide actions for conservation planning and design and ultimately benefit regional riparian protection, restoration and management practices.

1.6. Riparian Area Delineation in the Literature

The ARA framework was developed because of challenges associated with the status quo of riparian area delineation. It builds upon and integrates key findings from a long history of research in the fields of fluvial geomorphology. It also provides a means of addressing long-recognized shortcomings in certain standardized and commonly applied practices. Key among these are the use of fixed-width buffers rather than more

ecologically relevant functional riparian area delineation, and the development of effective digital methods and models for their accurate delineation.

1.6.1. Fixed-Width Buffer Guideline

Delineating the extent of ripairan area is not a straitforward task and may require the understanding of small scale environmental conditions since riparian functional attributes depend on site-specific variations such as landscape composition and the local environmental setting (Naiman & Décamps 1997). Because of this, many riparian conservation projects apply a "fixed-width buffer guideline", which is administratively and operationally simple (Richardson et al., 2012), to define and delineate the extent of riparian areas. It has been indicated, however, that fixed-width buffer guidelines for riparian delineation involve generalizations that may result in gross inaccuracies; they are not the ideal solution to riparian problems because "they are neither economically nor ecologically optimal along the entire stream network" (Kuglerová et al., 2014, p75).

Fixed-width buffer guidelines do not consider the relationships between the riparian functions and the distance from water, nor do they incorporate the potential importance of small-scale spatial heterogeneity (Kuglerová et al., 2014), and thus, fixed-width buffers may leave some riparian components out of the delineation. For instance, wide floodplains or low terraces that extend beyond the standard buffer width will not be included in riparian area delineations based on the standard; alternatively, lands that are arguably not riparian are likely be included in a fixed-width buffer, such as lands that are adjacent to small order streams but too distant to be influenced by or to influence the stream (Aunan et al., 2005). Because of the limitations and drawbacks of the fixed-width

buffer guidelines, riparian conservation and restoration projects that apply fixed-width buffers may fail in meeting their conservation goals (Kuglerová et al., 2014).

1.6.2. Objective-Based Riparian Area Delineation

Considering the limitations of fixed-width buffer guidelines, several updated riparian area delineation approaches apply more objective-based criteria (Fernández et al., 2012). Some are based on the physical properties of riparian areas, such as soil characteristics or flooding frequency. A study by Palik et al. (2004) identified riparian areas based on extent of wetlands and floodplains and the land area influenced by infrequent, ecosystem-altering floods, with the aid of hydric soil indicators and 100-year flood probability data. The researchers clearly indicated that the results derived from the hydric soil characteristics are more accurate than those results based on fixed-width buffer analysis. Other studies were based on biotic properties such as vegetation (D. M. Richardson et al., 2007) or amphibians (Perkins & Hunter. Jr., 2006). Crawford et al. (2007) applied two different survey methods (i.e. area-constrained daytime searches and nighttime visual encounter searches) to identify appropriate riparian buffer width for the conservation of stream amphibians. The authors recommended that identifying riparian width as 92.6 m in southern Appalachian streams is enough for protecting stream amphibians and other wildlife dependent on riparian areas. Whereas these methodologies are based solely on the single properties of riparian areas rather than the whole riparian area, functional riparian area delineation should ideally consider the riparian area as a dynamic system and should highlight the interactions among different component within riparian areas (Smith et al., 2008).

1.6.3. Functional Riparian Area Delineation

Given the importance of riparian areas and the current limitation in riparian area delineation, it is necessary to develop a conceptual framework which considers the "processes and attributes of flow and sediment regimes, physical habitat structure, water quality, energy sources and transfer, and biological interactions" (Smith et al., 2008, p3). To date, scientists have developed various methods for the functional riparian area delineation, but the development of a standard conceptual framework for functional riparian area delineation is still an open research topic (Salo et al., 2016; Luke et al., 2019).

Ilhart et al. (2000) first developed a definition of 'functional riparian areas' as "the three-dimensional ecotones of interactions that include terrestrial and aquatic ecosystems, that extend down into groundwater, up above the canopy, outward across the floodplain, up the near-slopes that drain to the water, laterally into the terrestrial ecosystem, and along the watercourse at variable width" (Ilhart et al., 2000, p8). This definition highlights the functional aspects of riparian area because it recognizes the riparian area by ecological structures and functions that occur at various scales. Riparian ecological functions are determined by the structural components of stream size, vegetative type, soil characteristics, and river valley (Naiman & Décamps, 1997), which are deeply constrained by river geomorphology. Thus, analyzing river geomorphology and the relationships between stream and valley morphology and riparian ecological functions can be an effective means of functional riparian area delineation.

Field surveys provide a practical and straightforward approach to study river geomorphology for the functional riparian area delineation (Verry et al., 2004).

Identifying the floodplain, terrace, and slope between the floodplain and terrace in the field is an effective way to define riparian areas (Ilhart et al. 2000). Several studies have mentioned that, through on-the-ground riparian area delineation, they have successfully identified the river stream, floodplain, and terraces (Hudson & Colditz, 2003; Polvi et al., 2011; Verry et al., 2004), and thus they have ultimately delineated the functional riparian area. However, on-the-ground functional riparian area delineation is a time-consuming and subjective approach and is less likely to be applied at regional geographical scales or larger (Holmes & Goebel, 2011; Yang, 2007).

1.6.4. Computer-Based Functional Riparian Area Delineation

At larger geographical areas, spatial analysis using GISystems may be used to overcome the challenges associated with intensive field work. Most of the existing spatial methods require DEM data as an input for the delineation of functional riparian areas. For instance, Fernández et al. (2012) delineated hydrologically meaningful potential riparian areas for the entire Cantabrian rivers network in Spain by creating several floodplain surfaces with the aid of DEM data. Benda et al. (2011) delineated the riparian area including active and former river and side channels, wetlands, floodplains and terraces of the Pas River Catchment based on multipliers of DEM derived 'bankfull' depth (which they defined as the depth of water in a channel of an elevation similar to the uppermost eroded banks).

Although spatial methods and elevation data have helped many researchers successfully delineate the extent of functional riparian areas at different spatial scales, limited studies have tested the performance of different spatial resolutions of input DEM data in terms of relative accuracy for functional riparian area delineation or made efforts

to identify the most optimal input DEM spatial resolution to run delineation models. Riparian area delineation executed in GISystems and based on coarse input DEM data may result in gross inaccuracies, and thus accuracy-efficiency tradeoff analyses should be carried out to identify optimal input DEM data spatial resolution to accurately and precisely delineate the extent of functional riparian areas, while remaining computationally feasible.

1.7. Structure of the Thesis

Following from the description of the purpose of the research and a brief overview of relevant riparian delineation studies provided in this first chapter, subsequent chapters will present the methods, results and discussion. In chapter 2, research objectives (1), (2) and (3) are achieved. The extents of ARA are delineated based on multi-resampled LiDAR DEMs, 30-m SRTM DEM, and 1:10,000 NBHN. The ARA results are compared with each other and to those derived from 30-m SRTM DEM and 1:50,000 NHN as delineated by NCC in terms of area and spatial extent. Additionally, a floodplain and terrace separation framework is explained. In chapter 3, a novel meander belt delineation framework is introduced and tested in the two study watersheds in order to achieve research objective (4). Chapter 4 achieves research objective (5) by analyzing the effect of DEM quality on the accuracy of topographic and hydrological indices and final ARA extent, and developing an accuracy-efficiency tradeoff analysis framework. Chapter 5 synthesizes key findings from the study as a whole, illustrates the challenges and limitations, and provides suggestions for future studies.

Chapter 2. ARA Delineation with Multi-Spatial Resolution LiDAR-DEM and SRTM-DEM Data

2.1 Introduction

The need to delineate the extent of functional riparian area to preserve ecological integrity of the riparian and freshwater ecosystems has been widely acknowledged (Naiman and Décamps, 1997; Smith et al., 2008). Several digital techniques have been developed for functional riparian area delineation, most of which are based on theory introduced by Ilhart et al. (2000) and Verry et al. (2004) through analyzing river topographic control on riparian hydrology and valley landform to predict flood-prone areas and the likely extent of the riparian area surrounding a stream or river. The applied algorithms differ among studies, including manual delineation of riparian area from digital topography (Holmes & Goebel, 2011), path distance allocation (Strager et al., 2000; Smith et al., 2008), elevation above the channel (EAC) (Abood et al., 2012; Benda et al., 2011), spatial disaggregation and aggregation procedures (Alber & Piégay, 2011) and flow accumulation (Shoutis et al., 2010).

The ARA framework based on path distance allocation provides a spatially explicit delineation of areas that provide space for key physical and ecological processes and disturbance regimes and necessary for the accommodation of ecological functions (Smith et al., 2008). Theoretically, the spatial extent of the ARA components is directly influenced by hydrology regime and sediment transport capacity, which are heavily controlled by stream and valley morphology (Smith et al., 2008). The use of GISystems, DEMs, and digitized hydrological networks can effectively achieve delineation of the active river area by synthesizing river geomorphology into a spatial ARA framework

(Robinson, 2017). However, as indicated in Chapter 1, almost all existing ARA-based studies were carried out with 10-m or 30-m SRTM DEM data and the national scale hydrological network (i.e. NHD and NHN) and failed in separating terraces from modern floodplain and/or achieving high accuracy ARA results.

Terraces are remnants of the former floodplains, formed from autogenic processes in downcutting rivers (Finnegan and Dietrich, 2011), or in response to unique environmental conditions that influence sediment and water fluxes (Anderson and Anderson, 2010). There are two main types of alluvial terraces differentiated by their formation process and geomorphic features: strath terrace and fill terrace (Pazzagila, 2013). Strath terraces are the result of a river downcutting through bedrock, characterized by a thin mantle of alluvium capping a planed bedrock surface. In contrast, fill terraces are the result of an existing valley being filled with alluvium, characterized by a thick alluvial deposit that buries the flat river valley bottom (Stout and Belmont, 2014). The formation process and geomorphic features of the two main types of terraces inform that terraces consist of a flat or gently sloping geomorphic surface, which are located higher than the modern floodplains. Thus, the elevation and geomorphic information of terraces provided by DEM data can be used as key indicators to separate them from modern floodplains. However, floodplain and terrace separation using GISystems is a data quality dependent procedure (Stout and Belmont, 2014). Use of low-spatial resolution DEM data with low horizontal and vertical precision is typically insufficient to identify subtle transitions between floodplains and terraces in slope and planform (Stout and Belmont, 2014).

To effectively separate the terrace from the modern floodplain based on their elevation differences and geomorphic features, high-spatial resolution DEMs obtained from LiDAR should be applied (Abood et al., 2012). LiDAR, in the simplest description, is an active remote sensing system that measures the return time of laser pulses to determine the distance from the instrument to some targets (Barber & Shortridge, 2005), which can be processed to produce very precise elevation data (Suárez et al., 2005). LiDAR-derived DEMs are high-resolution data (always in 1-m) (Vaze and Teng, 2007; Poppenga et al., 2009). At this spatial resolution, a DEM provides a detailed representation of the Earth's topography (Poppenga et al., 2009), that can benefit river valley topographic modelling and terrace delineation. Many new techniques that take advantage of high-spatial resolution LiDAR-derived DEMs are emerging for separating terraces from modern floodplains (MacMillan et al., 2003; Demoulin et al., 2010; Stout and Belmont, 2014). For example, Stout and Belmont (2014) developed a spatial tool named TerEx to semi-autonomously select, map and measure fluvial terraces based on local relief derived from DEM data. The authors found that the tool functions best when applied with high-spatial resolution DEMs (3-m or finer spatial resolution). Clubb et al. (2017) presented a digital method for identifying floodplains and terraces based on two thresholds (i.e. local gradient, and elevation compared to the nearest channel) calculated statistically from DEMs. In this study, the authors detected that 1-m LiDAR DEM derived terraces have a stronger spatial correlation with field-mapped terraces compared to 10-m SRTM DEM derived terraces. Although LiDAR-derived DEM data have been successfully applied to identify terraces based on other algorithms, the performance of LiDAR-DEM data in terms of ARA-based terrace delineation, to date, remains unclear.

In order to test the feasibility, an ARA-based separation framework should be developed to assess whether the use of high-spatial resolution LiDAR DEM data will allow the user to confidently differentiate terraces from modern floodplains.

The standard ARA framework has been successfully applied to delineate riparian basezones (i.e. floodplains and terraces), riparian wetlands, and material contribution zones. However, to achieve higher accuracy ARA results, continued refinement of input data quality is still expected given that quality and accuracy of the output is dependent on the quality of the inputs (Smith et al., 2008). To date, no existing ARA studies have tested whether high-resolution LiDAR DEM data can achieve higher accuracy in ARA results as compared to low-resolution LiDAR DEM data and commonly used SRTM DEM data.

In order to address these two gaps in ARA studies, this study tests: (i) the performance of high-resolution LiDAR DEM data (i.e. in 3-m and 5-m resolution) in terms of separating terraces from floodplains based on the ARA framework; and (ii) whether high-resolution LiDAR DEM data can achieve higher accuracy than low-resolution LiDAR DEM and commonly used SRTM DEM in ARA results. To do so, the extents of the riparian basezones (i.e. floodplains and terraces), riparian wetlands, and material contribution zones in the two study areas are delineated based on five spatial resolutions (i.e. 3-, 5-, 10-, 15-, 30-m) of resampled LiDAR-derived DEM data, 30-m SRTM DEM, and 1:10,000 NBHN. The ARA results (i.e. area and spatial extent) are compared with each other and to those derived from 30-m SRTM DEM and 1:50,000 NHN as delineated by NCC. The differences in terms of spatial extent of these ARA components will inform whether high-resolution LiDAR DEM data and NBHN achieve

high accuracy results as compared to low-resolution LiDAR DEM, SRTM DEM, and the NHN.

2.2. Materials and Method

In this section, the physical conditions of the two study areas will be described, followed by a description of the data applied in the ARA delineation. The developed floodplain and terrace separation framework will then be explained. Additionally, the standard ARA method applied for different ARA components (i.e. riparian basezone, riparian wetland, and material contribution zone) delineation will be introduced in different sub-sections. The same ARA delineation procedure is applied to five resolutions of resampled LiDAR DEM and 30-m SRTM DEM separately. Finally, the ARA combination framework will be introduced to illustrate how to integrate different ARA components together and define the final active river area extent.

2.2.1 Watersheds

From various provincial- and national-scale watershed layers, the NCC developed the Canadian Hydrological Unit (CHU) system to divide and subdivide the Acadian Ecoregion into successively smaller hydrological units (Noseworthy et al., 2019). The CHU system is a nested hierarchical drainage system (i.e. the hydrologic units are arranged or nested within each other), from the largest geographic area (i.e. CHU-2 drainage basins) to the smallest (i.e. CHU-12 cataloging units). The CHU-12 layer was created by NCC through piecing together the various provincial-scale watershed layers (Noseworthy et al., 2019). The higher-level drainage units were derived by grouping the CHU-12 units. For example, in order to determine the boundary of larger hydrological

units, CHU-12 units were grouped into CHU-10 units which were then grouped into CHU-8 units, and so on (Noseworthy et al., 2019). In order to delimit the scope for test purposes while maintain a hydrologically meaningful boundary, the two study areas in this study were selected from the CHU-6 level watersheds category.

2.2.2 Study Area

The two study areas, the Lower St. John River Watershed and the Miramichi River Basin Watershed (Fig. 2-1), are in New Brunswick, where full 1-m LiDAR-derived DEM coverage is available. The Lower St. John River Watershed (Fig. 2-1a) drains an area of 14343 km^2. Evaluating the descriptive statistics of the 1-m LiDAR DEM data (Fig. 2-2a), elevations in the watershed range from -5m to 553 m above mean sea level (AMSL). The main stem of the systems is the Lower St. John River; this main stem is fed by many significant tributaries, including the Nashwaak, Oromocto, and Kennebecasis Rivers. The flatness of this watershed has resulted in the formation of large lakes such as Grand Lake and Washademoak Lake (Kidd et al., 2011). This watershed has longer, and warmer growing seasons compared to other watersheds at a similar latitude (Zelazny, 2007) from the heat sink effect of the large lakes. Mean annual temperature and precipitation are 5°C and 1300 mm, respectively (Environment Canada, n.d.). This mild climate supports a number of riparian plant species such as basswood, white ash, and green ash (Kidd et al., 2011). The bedrock is mostly sedimentary, with pockets of metamorphic and volcanic rock (Kidd et al., 2011). The dominant soil types are humo-ferric podzols and gray luvisol (USask, 2010). Organic soils such as gleysols, fibrisols, and mesisols are found in the wetlands throughout the watershed (Kidd et al., 2011).

The Miramichi River Basin Watershed comprises an area of approximately 12069 km^2 (Fig. 2-1b). The main stem is the Miramichi River, which drains into Miramichi Bay in the Gulf of St. Lawrence. The length of Miramichi River measures approximately 250 km and comprises two main branches, the Southwest (SW) Miramichi River and Northwest (NW) Miramichi River, each having their respective tributaries (Wikipedia, n.d.). The NW Miramichi River is the smaller of the two systems, draining 3,900 km^2, whereas the SW Miramichi River drains 7,700 km^2 (Swansburg et al., 2011). The Miramichi River and its tributaries support one of the largest populations of Atlantic salmon (*Salmo salar*) in North America, as well as runs of other anadromous fish such as American Shad (*genus species*), smelt (*genus species*), herring (*genus species*), and sea-run brook trout (*genus species*). About one-half of the current sport catch of Atlantic salmon in North America is landed on the Miramichi River and its tributaries (MyNB, 2015). Descriptive statistics of the 1-m LiDAR DEM data (Fig. 2-2b), revealed that the elevation of the watershed ranges from -4m at the eastern portion to 762 m AMSL within the Miramichi Highlands. The average summer temperature is 16.5°C and average winter temperature is -7.1 °C, and average annual precipitation is 1100 mm (Environment Canada, n.d.). The major bedrock is sandstone, while Silurian and Ordovician rocks can be found in the Miramichi Highlands (MyNB, 2015). Soils are typically acidic with shallow topsoil, leading to poor suitability for agriculture (Wikipedia, n.d.). Most of the watershed is uninhabited woodlands and much of it is harvested for wood products. In the northern portion, located on the smaller Tomogonops River, mineral resources such as zinc, copper, and lead were extracted until the facilities were decommissioned in 2000 (MREAC, n.d.).

a. Lower St. John River Watershed

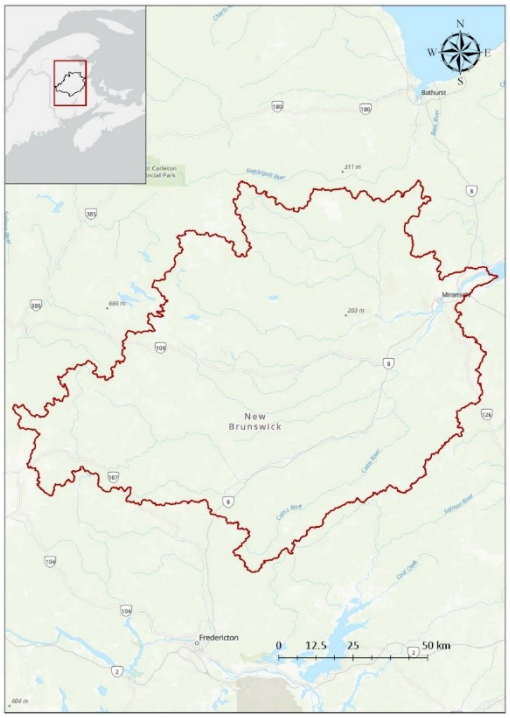

b. Miramichi River Basin Watershed

Figure 2-1 Study Areas

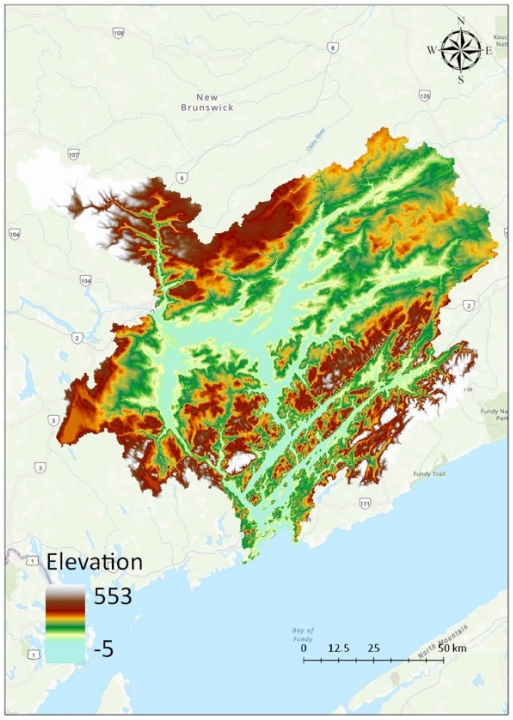

a. DEM of the Lower St. John River Watershed

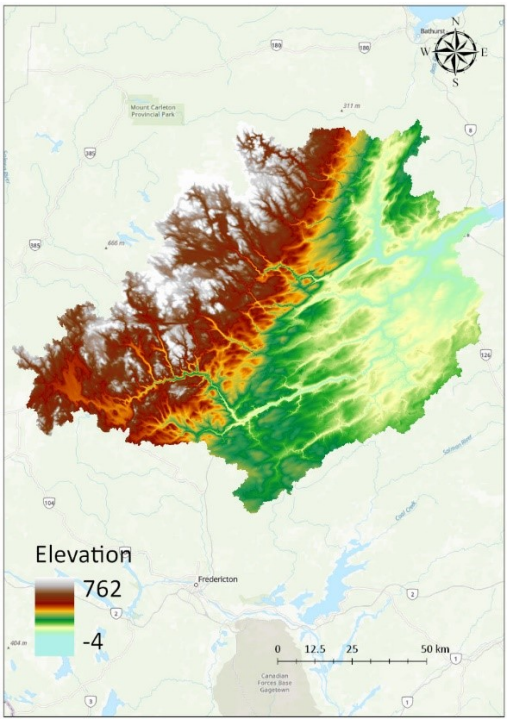

b. DEM of the Miramichi River Basin Watershed

Figure 2-2 Digital Elevation Model of Study Areas

2.2.3 Data Acquisition and Preparation

The input datasets for this study include 1-m LiDAR derived DEM data, 30-m SRTM DEM, 1:10,000 NBHN, provincial forest soils data, and existing satellite derived flood extent data (Table 2-1). The elevation datasets (i.e. LiDAR-DEM and SRTM-DEM) and NBHN are key input datasets for the ARA delineation, while the other datasets were used as ancillary data to set parameters and calibrate results.

Table 2-1 Brief descriptions of applied datasets

Dataset	Brief Description	Original Format	Responsible Agency	Source
LiDAR-derived DEM	LiDAR-derived DEMs in 1-m resolution in New Brunswick Stereographic Double Projection.	GeoTiff (.tif)	SNB	http://geonb.snb.ca/nbdem/ (Date: 2019-05-31)
SRTM-DEM	SRTM-DEM in 1 arc-second (~ 30-m) spatial resolution in WGS 84 Horizontal Datum	GeoTiff (.tif)	USGS	https://earthexplorer.usgs.gov/ (Date: 2000-02)
NBHN	Surface drainage features including rivers, streams, lakes, islands, and watershed boundaries including names for many rivers and streams.	Shapefile (.shp)	ERD	http://www.snb.ca/geonb1/e/DC/NBHN.asp (Date:2018-08-29)
Forest Soils	Polygons of Forest Soils Units, including information on drainage, slope, and aspect.	Shapefile (.shp)	ERD	http://www.snb.ca/geonb1/e/DC/forestsoils.asp (Date:2015-08-18)
Satellite-derived Flood Extent	Landsat imagery derived-flood extent in the year of 2011	Shapefile (.shp)	ELG	http://www.snb.ca/geonb1/e/DC/floodraahf.asp (Date:2011-09-01)

The provincial 1-m LiDAR-derived DEM data was generated from the LiDAR point cloud data collected by the Government of New Brunswick in 2016 and 2018. To convert LiDAR point cloud data into DEM data, calibrated point cloud strips were initially processed into 1-km tiles in the New Brunswick Double Stereographic projection with the aid of a series of off-the-shelf software and proprietary tools (e.g. CloudCompare and Fusion and etc.). A combined automatic-manual classification was then executed by separating points into ground (class 2), non-ground (class 1), low noise (class 7), and high noise (class 18). Once the classification of the LiDAR point cloud data was finalized, a Triangulated Irregular Network (TIN) of all existing ground points was populated and a 1-m 32-bit (i.e. floating point) continuous raster was created from the TIN using natural neighbors sampling techniques (Connors, personal communication, November 29, 2019). The global vertical accuracy reported for the LiDAR point cloud data used for the generation of the DEM of Lower St. John River Watershed and Miramichi River Basin Watershed is 0.105 m and 0.063 m RMSE, respectively. Interpolation error introduced during the DEM generation was not quantified by the data provider (GeoNB, 2016; GeoNB, 2018).

To produce multi-resolution LiDAR-derived DEM data for test purposes, the provincial 1-m LiDAR-derived DEM data for the study areas were resampled (i.e. upscaled) into five lower spatial resolution DEMs (i.e. 3-m, 5-m, 10-m, 15-m, 30-m) by using Bilinear interpolation techniques which determines the new value of a cell based on a weighted distance average of the four nearest input cell centers (ESRI, 2016). In addition to the bilinear interpolation, there are two other commonly used resampling techniques in GIS-based studies, which are Nearest-Neighbor interpolation and Cubic-

Convolution (Wu et al., 2008). Nearest-neighbor interpolation does not change the original elevation but tends to leave unwanted artifacts, which directly affect flood inundation modeling and are usually recommended for categorical data (ESRI, 2016). The Cubic-Convolution method is similar to Bilinear interpolation but takes more time to process the computation and is usually used when there is too much noise in data (Fereshtehpour and Karamouz, 2018). As this study focuses on DEM resolution effect on ARA delineation, no further comparisons are made on resampling techniques. Bilinear interpolation was chosen for use in this study as a compromise between pixel value preservation and topographical smoothing.

The NBHN is a digital hydrological network representing the location, characteristics and connectivity of water and water-related features within the province (GNB, 2013), which contains watercourse network, waterbody, water spot depth, hydrographic obstacle data, and other features (DataQC, 2009). The watercourse network is the foundation of the NBHN. It includes all non-isolated observed, inferred (spines) and constructed watercourse and junction entities, which provide a connected line network throughout the watercourses, wetlands and waterbodies that comprise each watershed (DataQC, 2009). The NBHN was originally delineated from the DNR orthophotos and modified to be geometrically seamless and continuous within a watershed and digitized in the downstream direction (DataQC, 2009). The general horizontal accuracy of ± 2.5 m was reported for the NBHN (DataQC, 2009). In order to determine the location of open freshwater and wetland within the two study areas for ARA delineation, only watercourse network, waterbody, junction entities and wetland data in NBHN were applied in this study.

2.2.4 Stream Classification and Watersheds Stratification

In ARA delineation, the extents of floodplains and terraces are determined by measuring the relative costs of water traveling upslope from the stream (Smith et al., 2008). This cost is a computation of the elevation and distance from the channel, with higher costs for greater elevations and distances (Barnett, 2011). The cost surface is continuous and therefore a cost threshold is required to cut-off the area which is no longer likely to be dynamically linked to the river or stream (Strager et al., 2000). Larger rivers have more water volume than smaller rivers, so their floods cover higher costs. Additionally, in sub-watersheds (i.e. CHU-8 level watersheds) with flat topography, cost increases slowly as water move away from the river in comparison to sub-watersheds with relief topography, so cost thresholds need to be lower in flat sub-watersheds to accommodate a flood of the same river size (Barnett, 2011; Nussey and Noseworthy, 2020). Given these factors, cost thresholds must be determined for rivers in different size classes and sub-watersheds separately, and thus the initial stage of the ARA delineation is to separate rivers into different classes given their size differences and assign a slope class to each CHU-8 level watershed within the two study watersheds. Assigning cost thresholds for rivers in different size classes separately will also allow the flood from a larger size river to correctly overwrite the flood of a smaller size river at their junctions.

The stream classification system applied in this study is the Strahler stream order system. It is a method for assessing river size and complexity based on the number and hierarchical relationship of tributaries (Strahler, 1957). The differences in terms of river sizes are represented by the Strahler order number (Fig. 2-3). For example, the headwater is the smallest stream in a watershed, with no tributaries, so it is considered a 1st-order

stream (i.e. the Strahler stream order number is "1"). When two 1st-order streams (i.e. headwaters) join each other, a 2nd-order stream is formed. When two 2nd-order streams join, a 3rd-order stream is formed, and so on. The ordering continues downstream within a drainage network. Smaller or lower order streams entering the network will not change the Strahler order of larger or higher order streams. For example, a 3rd-order stream entering a 4th-order stream will not change the Strahler order of the 4th-order stream.

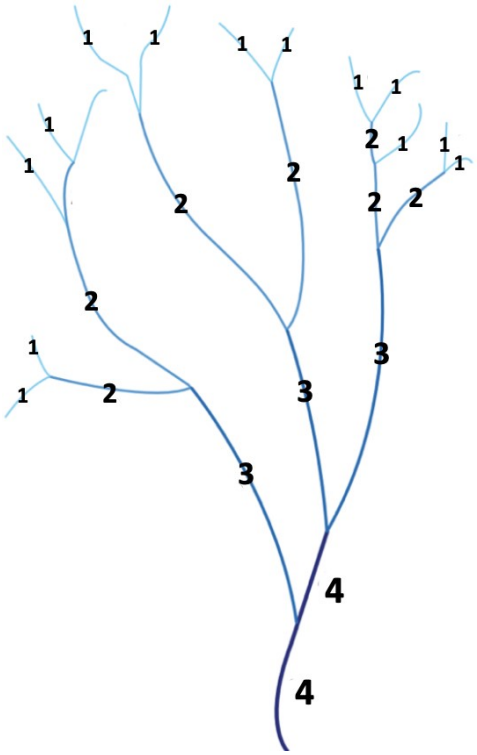

Figure 2-3 Stream ordering using the Strahler stream order system (Graphic: Adapted from Pierson et al. NHDPlus, 2008).

Strahler stream order values have already been assigned to each watercourse segment of the NBHN by DataQC (DataQC, 2009), which range from "1" to "8" (Table 2-2). To determine how to reorganize watercourse segments with different Strahler order numbers into different river size classes, several known examples in the study watersheds were applied to conduct a benchmark analysis to align the stream classification results as closely as possible with that in the NCC-ARA project (i.e. NCC stream classification

system V2.0) (Nussey and Noseworthy, 2020) for the final comparison purposes. The NBHN watercourse network was separated into five different size classes based on their Strahler stream order number (Table 2-2); waterbodies were separated into different river size classes based on the Strahler order of the largest river passing through the waterbody. The Strahler stream classification results were then directly compared to the NCC stream classification V2.0; the discrepancies in the river classification results were found to be negligible. The classified watercourse network and waterbody shapefiles were then converted into a raster format and merged together with the waterbody grids overwrite watercourse grids at their junctions.

Table 2-2 The relationship between river size classes and Strahler stream order numbers

Size classes	Strahler stream order numbers
Great Rivers	8
Medium Rivers	6,7
Small Rivers	4,5
Creeks	2,3
Headwaters	1

To determine cost thresholds for the rivers in the sub-watersheds exhibiting different topography separately, two CHU-6 level watersheds were divided into two slope classes based on sampling the percentage of each CHU-8 level watershed that fell into a zero-slope class within the integer slope grid. The following thresholds (Table 2-3), applied by both NCC and TNC, were used to define the slope classes for each CHU-8 level watershed.

Table 2-3 Watersheds Stratification by Slope Classes

Slope Class	Descriptions
Slope Class 1	< 10% of CHU-8 level watersheds in slope of zero
Slope Class 2	10-25% of CHU-8 level watersheds in slope of zero

2.2.5 Riparian Basezone Delineation

The ARA riparian basezone includes floodplains and terraces (Barnett, 2011). This step creates a cost distance surface and determines the cost distance thresholds for each river size class, and ultimately delineates the extent of the riparian basezone in each study watershed. Cost distance surface was created by running the cost distance command in ArcGIS Pro™ (ESRI, 2018), that requires two input raster layers, one for the friction surface and the other for the source cells. For the purpose of delineating the extent of the active river area, watercourse and waterbody grids were treated as source cells from which the least accumulated cost distance for every output cell location was calculated (Fig. 2-4a). The friction surface is the slope grid (in degrees) generated from the DEM data (Fig. 2-4a). With source cells and friction surfaces determined, the cost distance algorithm was then performed on each cell of the slope grids, moving outward from the input watercourse and waterbody grids. Following the method used by NCC and TNC to reduce the processing time by not analyzing areas beyond a likely ARA extent, the maximum cost distance was set to "5000", so that the algorithm stops after a cost distance of "5000". These operational procedures were applied separately for each river size class based on multi-resolution LiDAR-DEMs (i.e. 3-, 5-, 10-, 15-, 30-m), 30-m SRTM DEM, and NBHN grids. The results of the cost distance function are given as a surface of values indicating the relative costs (iii) of moving from the watercourse cells up into the stream valley, accounting for distance (i) and elevation change (ii) (Fig. 2-4b).

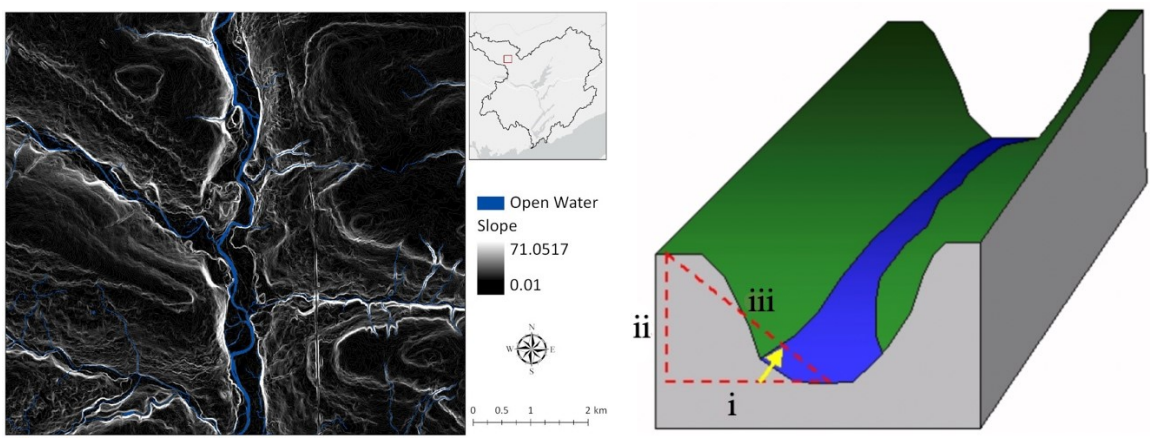

a. *b.*

Figure 2-4 Cost distance modelling: (a) inputs to cost distance function in a GIS, including slope grids and watercourse grids (blue); (b) schematic stream valley cross-section shows the inputs to cost distance function, including cost slope (yellow arrow) and source (stream) (Graphic: Adapted from Stager et al., 2000).

After producing cost distance surface for each river size class, cost distance thresholds were determined for each river size class within slope class stratified sub-watersheds to delineate the extent of the riparian basezone. To precisely determine the cost thresholds, the existing satellite-derived flood extent (ELG, 2011) was applied to calibrate the cost thresholds (Fig. 2-5). However, satellite-derived flood extent is not available for all streams and rivers in the two study areas. Methods for determining cost thresholds for areas with and without satellite-derived flood extent are detailed in the following two subsections.

Determining Cost Threshold for Areas with Satellite-Derived Flood Extent

For areas with satellite-derived flood extent coverage, cost thresholds were determined through iterative trial and error alignment with the existing flood extent. Statistical overlap analysis was performed to find a cost distance threshold that maximized the amount of the existing flooding captured by the ARA-derived riparian basezone (i.e. the percentage of ARA basezone fill inside the satellite-derived flood

extent), while minimizing the amount of non-flooding map area captured (i.e. ARA basezone spill outside the satellite-derived flood extent). More precisely, for each river size class: (i) multiple riparian basezone extents were created using multiple cost distance thresholds; (ii) the differences of percentages between their "fill" and "spill" (i.e. percent of overlap – percent of non-overlap) with regard to the satellite-derived flood extent were then calculated; and (iii) the cost threshold that maximized fill and minimized spill (i.e. the result that achieve greatest difference between percent overlap and percent non-overlap) was determined. The determined cost threshold was then applied to limit the cost distance surface to delineate the ARA riparian basezone.

Determining Cost Thresholds for Areas without Satellite-Derived Flood Extent

For creek and headwater areas where the satellite-derived flood extent was not consistently mapped, cost distance thresholds tested by NCC were applied. To make sure that the NCC thresholds were suitable for the two watersheds in this study, the following testing procedure was carried out. Since the extent of riparian basezone is essentially the extent of valley bottom, the extent of valley bottom can be used to inform the extent of riparian basezone. To determine the extent of valley bottom, "Hillshade" grids were generated from the LiDAR-derived DEM data, intended to augment the representation of the morphology of the river valley in a 3D grayscale version. After creating "Hillshade" grids, NCC cost-threshold-derived creeks and headwaters riparian basezones were visually inspected on the top of "Hillshade" grids to see whether they were associated with the extent of valley bottom.

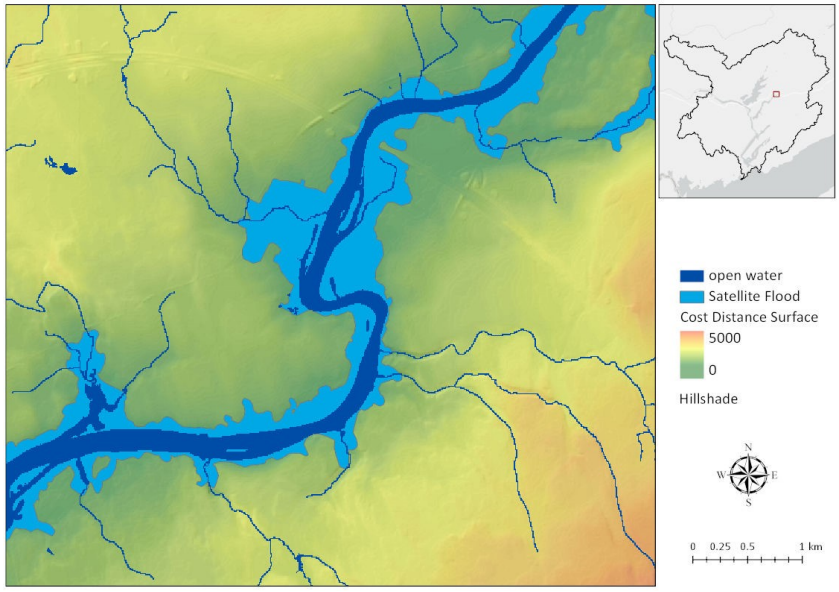

Figure 2-5 Example of cost distance threshold calibration in a GIS. The input datasets include existing satellite derived flood extent (light blue), cost distance surface and openwater grids (blue).

Finally, the calibrated riparian basezone for each river size class was clipped at some Euclidean distance from the river (i.e., distance dependent on river class) to avoid problems with the cost-threshold-derived riparian basezone extending an unrealistic distance from the river in flat areas, as well as skipping across bays and estuaries along the coastal areas, since the cost was increased slightly in flat areas and open ocean water. Based on the guidelines shared by TNC (Barnett, 2011) and NCC (Nussey and Noseworthy, 2020), the following Euclidean distances were adopted for this study:

- Large/Great Rivers (Strahler number: 8): 2 miles, 3219 m;
- Medium Rivers (Strahler number: 6, 7): 1.5 miles, 2414m;
- Small Rivers (Strahler number: 4, 5): 1 mile, 1609m;
- Headwaters/ Creeks /Isolated Lakes (Strahler number: 1, 2, 3): 1mile, 1609m.

2.2.6 Floodplain and Terrace Separation

The aim of this step is to develop an ARA-based framework to differentiate terraces from floodplain based on their height differences and geomorphic features with

the aid of high-spatial resolution LiDAR DEMs. Since the limitation of 10-m DEM data in differentiating terraces from the modern floodplain has been well established in previous studies (Marangelo and Farrell, 2010; Smith et al., 2008), efforts were only made to examine how 3-m and 5-m LiDAR DEM data perform in differentiating terraces from the floodplain, based on the developed separation framework.

As introduced in the former section, the standard ARA framework delineated the extent of riparian basezone by creating the cost distance surface based on path distance allocation (Smith et al., 2008). To ensure the developed separation framework is consistent with the standard ARA framework, the proposed floodplain and terrace separation framework is trying to detect the cost distance value underneath the transition lines between floodplain and terrace in slope and planform to differentiate the terrace from floodplain for each river size class. To extract the cost distance value underneath the floodplain-terrace transition lines, the subtle transitions between floodplain and terraces need to be identified and located within the river valley based on valley morphology information provided by high-spatial resolution LiDAR DEM data. The 'Interpolate Shape' command is an ideal tool to model the cross-valley morphology by interpolating height values for each valley cross-sectional line from a DEM surface. The interpolated valley profile allows the user to visualize elevational and horizontal-distance changes over a continuous distance.

To model the river valley morphology in this study, cross-sectional lines were manually generated orthogonal to the longitudinal direction of the river valley for different river size classes in portion (Fig. 2-6). River valley morphology profiles were then interpolated with the aid of the 'Interpolate Shape' command based on the location

of the cross-sectional line for each river size class. The output profile graph is the cross-section through the river valley at any given point along the cross-sectional line. It includes the top of one side of the valley, across the valley floor, which contains the river bankfull, up to the top of the other side of the valley (Fig. 2-6).

Based on the valley morphology profiles of different river size classes, river valleys were classified into three categories: V-shape (Fig. 2-6a), U-shape (Fig. 2-6b) and UT-shape (U-shape with terraces) (Fig. 2-6c). A V-shape valley is relatively narrow compared to the other two valley types, suggesting active incision; floodplains are relatively narrow or absent in this type of valley. A U-shape valley is a flat-bottomed valley, indicating that the valley wall is widening and/or the valley bottom is undergoing aggradation, which means that terraces have not been formed and all flat areas may be floodplain rather than terraces. A UT-shape valley is a flat-bottomed valley with terraces, indicating that there have been former high river levels whose geomorphic signatures are preserved (Yan et al., 2017). The geomorphic features of these three types of river valley indicate that the fluvial terraces only exist within UT-shaped river valleys, and thus transitions between floodplain and terraces were only identified on the profile map of the UT-shaped river valleys. Once the location of the first level terrace was identified on the profile map (Fig. 2-6c), the distance between the start point of the cross-sectional line and the start point of the terrace was measured. This distance measure represents the location of the floodplain-terraces transition line within the riparian basezone. The underlying cost distance value of the transition line was then extracted. To get a representative cost distance threshold for terraces and floodplain separation, several cross-sectional lines were created for different rivers in the same size class across both study areas; the

average of the extracted cost distance values of each river size class was then calculated and used as the separation threshold for that river size class. Once the separation cost thresholds for different river size classes were identified, the extent of floodplain and terraces of different river size classes were delineated with the aid of the “Reclassify” command.

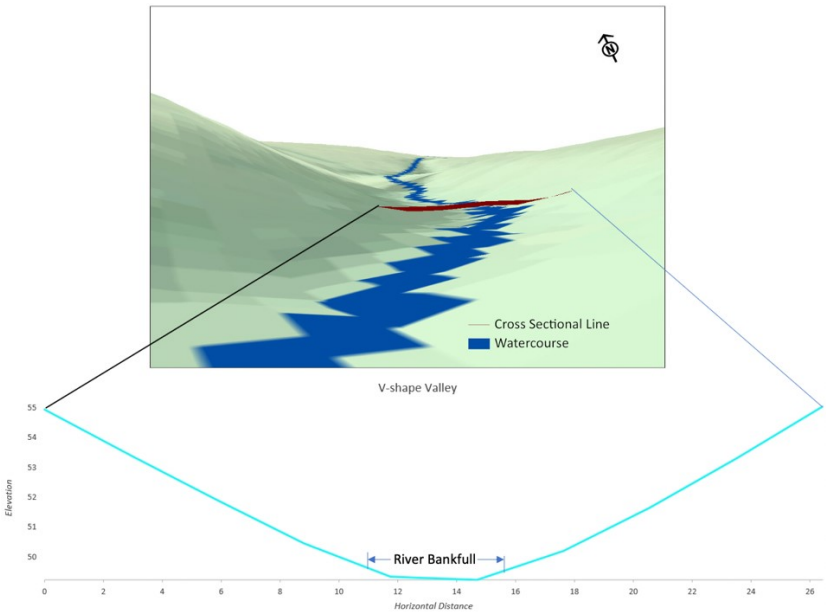

a. V-shape Valley

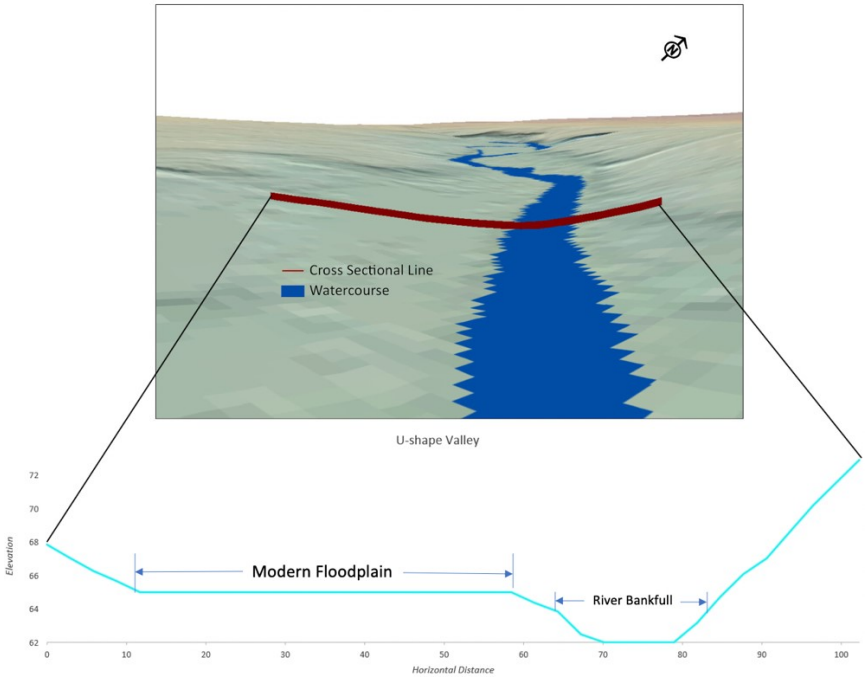

b. U-shape Valley

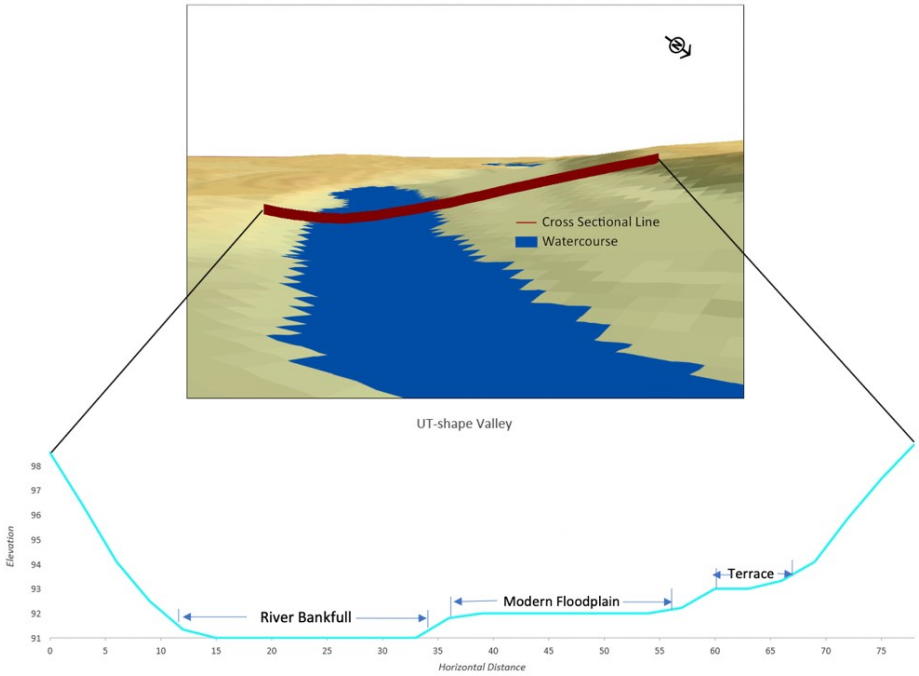

c. UT-shape Valley

Figure 2-6 Illustration of three different river valley shapes. (a) V-shape valley: the floodplain is relatively narrow or absent; (b)U-shape valley: the floodplain has clear flat zones, but there is no terrace exist; (c) UT-shape Valley (U shape with terraces):it has both floodplain and terraces and hence there is more than one flat level in the river valley.

2.2.7 Riparian Wetland Delineation

Riparian wetlands are low-gradient areas with inundated or hydric soils as a result of high surface water and/or groundwater levels. In order to detect certain low gradient areas with high water accumulation levels, topography and flow accumulation patterns were modelled separately across the study watersheds.

Topography patterns for each study watershed were modeled by analyzing slope change with the aid of DEM data. Slope change patterns were analyzed by creating slope grids (in degree) with the aid of the "Slope" command. Flow accumulation patterns were modelled by creating flow accumulation grids across the study areas. To generate flow accumulation grids, hydrologically correct flow direction was first determined, providing the basis for calculating the accumulated flow to each cell (ESRI, 2018). Although high-spatial resolution LiDAR DEM data is strong at capturing the stream network in fine detail and creating hydrologically correct flow direction grids, human infrastructural features that have elevations similar to the watercourse may bias the model. The 'DEM AGREE' method (Hellweger, 1997) was therefore applied to mitigate the influence of human infrastructure and depressions or pits on the flow direction modelling by modifying the elevation of stream cells within a DEM and entrenching the correct hydrological patterns into a DEM (Callow et al., 2007). The result was then applied to model the direction of flow from every cell in the raster by determining the direction of steepest descent or maximum drop from each cell based on the 'D-8 flow model' algorithm (Jenson and Domingue, 1988).

To integrate the topographic pattern with the flow accumulation pattern to determine the potential wetland area, a 'Topography Moisture Index' (TMI) (Barnett, 2011) (Fig. 2-7) was developed and calculated based on the following formula:

$$\text{TMI} = \text{int}\,(\text{focal mean}\left(\text{int}\left(\frac{\text{Ln}(\text{Flow Accumulation} + 1)}{(\text{slope} + 1)} * 1000\right)\right) + 0.5)$$

Equation 2-1

A high TMI value indicates a high flow accumulation value and a low slope value, and therefore land areas with high TMI values may be considered potential wetland areas. To calibrate the wet-dry threshold for detecting potential wetland area over the TMI grid surface, provincial wetland data and hydric soil data were applied. Additionally, following the method used by NCC and TNC, the extent of "wetflat grab zone" (i.e. 2x the cost threshold of the riparian basezone) was applied to limit the extent of potential wetland area to make sure the "wet" is a result of the physical prosses of riparian areas (Barnett, 2011; Nussey and Noseworthy, 2020). Once the potential wetland areas were detected, the potential wetland cells were region-grouped to reflect the nature of connectivity within riparian wetlands with the aid of "Region Group" tool. Since this ARA component is called the riparian wetland, only those region-grouped wetland cells that directly link to the riparian basezone of different river size classes were retained and determined as the riparian wetlands of each river size class. The same wetland delineation procedure was applied to multi-resolution LiDAR DEMs and SRTM DEM separately for comparison purposes.

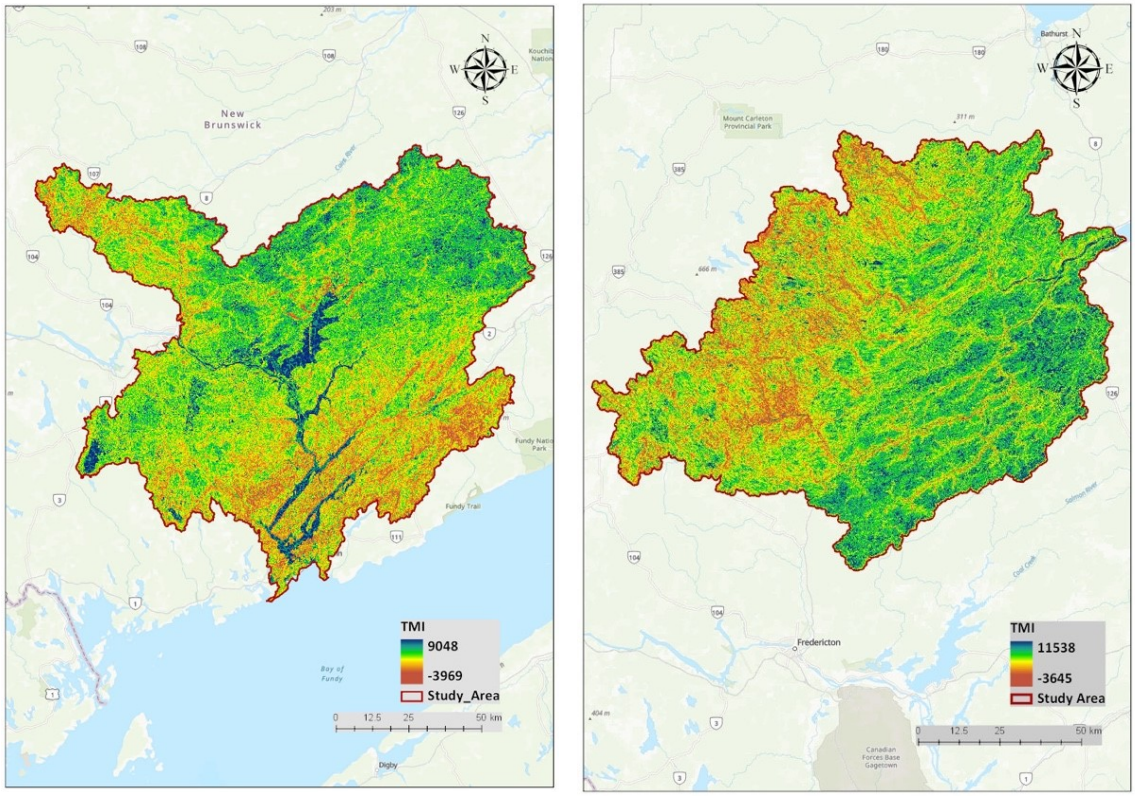

a. TMI of Lower St. John River Watershed

b. TMI of Miramichi River Basin Watershed

Figure 2-7 Topographic Moisture Index of (a) Lower St. John River Watershed and (b) Miramichi River Basin Watershed in 5-m resolution. The figures indicate the distribution of the land areas with high TMI value (blue) and low TMI value (orange) across the study areas.

2.2.8 Material Contribution Zones (MCZs) Delineation

This step is designed to capture the additional areas adjacent to the rivers, which are not riparian basezone but still actively contributing to rivers through erosion and input of large woody debris, etc. (Smith et al., 2008). Following the methods developed by NCC (Nussey and Noseworthy, 2020), 60-m planar buffers were created on both sides of rivers across the two study areas to delineate areas where organic materials and energy transportation are likely to occur. A 60-m safety buffer was selected based on a review of buffer sizes for riparian conservation regulation by the Environmental Law Institute (2003), in which a riparian buffer of 50 m or more was recommended for temperature and riparian microclimate regulation, detrital input, and bank stabilization. However, a 60-m

buffer was found to be inadequate for delineating MCZs for rivers located in confined valleys with steep slopes that extend beyond 60 m (Fig. 2-8). As introduced by the scientists from NCC (Nussey and Noseworthy, 2020), if slopes adjacent to streams have a 15% or greater rise, sediments and nutrients will enter streams from areas beyond 60 m, to the top of the slope. To address the limitation of a 60-m buffer for delineating steeply sloped MCZs, a component named 'ARA steep slope areas' was developed to supplement the 60-m-buffer MCZ (Nussey and Noseworthy, 2020).

To detect land areas with slopes of 15% or greater, slope grids (in percent rise) were created from the different spatial resolutions and sources of DEM data and then converted into polygons. A 60-m buffer was then created around the steep slope polygon to minimize mismatch errors between the hydrography layer and the DEM data (Nussey and Noseworthy, 2020). The buffered steep slope polygons were then used to clip the original watercourse layer. The remaining watercourses, named as 'steep slope flowlines', represent only those rivers that occur within the 60-m steep slope buffer area. The start and end points of the remaining watercourses were then generated and used to split the original NBHN watercourse layer to highlight the location of steep slope flowlines in the NBHN river network. Catchments were then delineated for each segment of split NBHN flowlines with the aid of ArcHydro Toolbox in ArcGIS Pro™, and the center points of the steep slope flowlines were created and used to select those catchments which contain steep slope flowlines. After picking up catchments that contain steep slope flowlines, the steep slope polygons were clipped to the steep slope catchments, and the steep slope polygons beyond the extent of 60-m MCZs were deleted. The same operation was completed for lakes using the 'lake polygon boundary' instead

of the watercourse layer. The lake steep slope areas and watercourse steep slope areas were combined with the 60-m buffer MCZs to represent the full extent of MCZs.

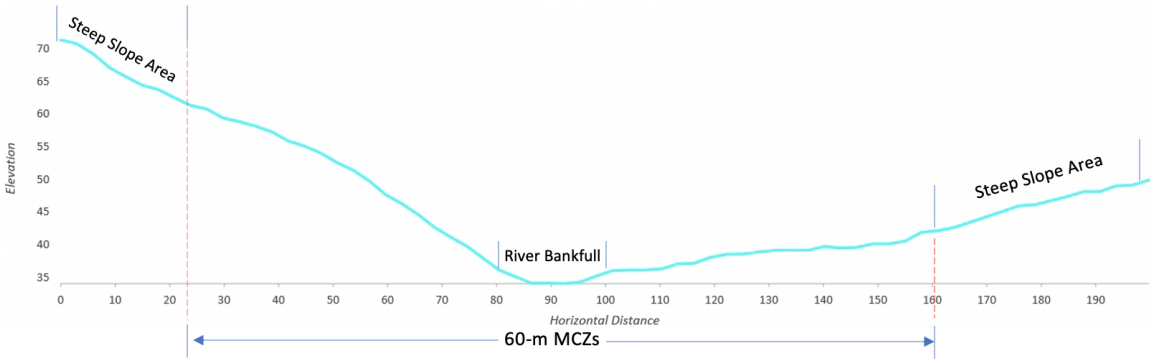

Figure 2-8 Profile map of a river situated in confined valley, which illustrates that 60-m buffer is too narrow to incorporate all the steep slope areas into the final MCZs extent.

2.2.9 ARA Components Combination

Finally, the ARA components were combined to delineate the final ARA extents based on their "flooding likelihood" (Barnett et al., 2011; Nussey and Noseworthy, 2020). Higher order streams have more water volume and power to flood than lower order streams, so the floodplain of larger rivers overwrite the floodplain of smaller rivers at overlapping areas when merging the floodplain of rivers in different size classes. These areas of overlap are mostly at river junctions, such as where a medium river merges into a great river. Since terraces are former floodplains that are not well integrated into the existing hydrological regimes of the river (Yan et al., 2017) and tend to be flooded only during extreme flood events (i.e. 20-100 years flood) (Smith et al., 2008), the 'floodplain combination' should overwrite the 'terraces combination' at their junction areas. To assure floodplain dominated where there was an overlap between floodplain and terrace, fluvial terraces of rivers in different size classes were merged together and then added underneath the floodplain combination. As recommended by NCC (Nussey and Noseworthy, 2020), ARA components of different river size classes should be condensed

into a single ARA component layer in the final ARA output to resonate more with stakeholders and conservation planners. To achieve the condensation, floodplains combination and terraces combination were simplified by merging different size-class floodplains and terraces into two categories, namely 'ARA floodplain' and 'ARA terraces'. Next, the riparian wetlands of rivers in different size classes were added and condensed together in a similar way (i.e. larger-river wetlands overwrite smaller-river wetlands) and then the wetland combination was added beneath the ARA floodplain and ARA terrace combination. The overlapping areas of the ARA basezone (i.e. ARA floodplain and ARA terraces) and riparian wetlands were selected and named as 'ARA floodplain (wet)' and 'ARA terraces (wet)', while the basezone areas where no wetlands exist were named as 'ARA floodplain (non-wet)' and 'ARA terraces (non-wet)'. Additionally, the wetland areas that exceed the extent of ARA basezone but are still within the extent of "wetflat grab zone" (i.e. 2x basezone) were named as 'ARA riparian wetland'. The headwaters systems were then added beneath and merged into the above combination. First their riparian basezones were added and then their wetlands. This size class was deemed to have the least power to flood and thus the larger river basezones and wetlands dominated where there was an overlap. Finally, the MCZs (i.e. 60-m buffer and steep slope area) of watercourses and waterbodies were added underneath the ARA combinations, which allowed the MCZs to be added to areas where no other ARA components exist. The hierarchy for combining raster layers is as follows in descending order, where (i) is considered as having the greatest likelihood of flooding:

(i) ARA Floodplain combination (wet); ARA Floodplain combination (non-wet)

(ii) ARA Terraces combination (wet); ARA Terraces combination (non-wet)

(iii) ARA riparian wetland

(iv) Headwater system (headwater basezone and headwater wetland)

(v) Steep slope area

(vi) 60-m riparian buffer

2.3 Results

ARA extents derived from different spatial resolution LiDAR DEMs and 1:10,000 NBHN will be provided and compared with each other and to those derived from 30-m SRTM DEM and 1:10,000 NBHN. ARA derived by NCC based on 30-m SRTM DEM and 1:50:000 NHN will also be included in the comparison. Differences in the areas of different datasets-derived ARA will be illustrated, informing whether high-spatial resolution LiDAR DEM data can achieve floodplain and terrace separation within riparian basezones and whether high-spatial resolution LiDAR DEM data can achieve higher accuracy ARA results as compared to low-spatial resolution LiDAR DEM and the low-spatial resolution SRTM DEM.

2.3.1 Cost Threshold Values

Cost threshold values derived for use in riparian basezone delineation and floodplain and terrace separation across parallel analyses at the various DEM spatial resolutions and sources are presented in Appendix A. The results show cost threshold values are more largely influenced by river size classes than by the topographic settings of different sub-watersheds. For the rivers in the same size class, cost threshold values determined by lower spatial resolution LiDAR DEMs are generally greater than that determined by higher spatial resolution LiDAR DEMs.

2.3.2 Area of Openwater

The area of openwater (i.e. watercourses and waterbodies) calculated from lower spatial resolution LiDAR DEMs is greater than that calculated from the higher spatial resolution LiDAR DEMs in both study areas (Table 2-4). For example, openwater areas range from 744.16 km^2 (at 3-m resolution) to 1281.73 km^2 (at 30-m resolution) in the Lower St. John River Watershed. Additionally, the openwater area calculated from the 30-m SRTM DEM and 1:10,000 NBHN is greater than that calculated from the 30-m SRTM DEM and 1:50,000 NHN, at 1281.73 km^2 and 910.47 km^2 respectively in the Lower St. John River Watershed (Table 2-4a).

2.3.3 Riparian Basezone

Riparian basezone is the dominant component of the active river area in all spatial resolutions and sources of DEM-derived ARA results (Table 2-4). The proportion of riparian basezone located on the "wet" area is greater than that on the "non-wet" area. The same pattern is seen across the parallel analyses with all the spatial resolutions and sources of DEM data in both study watersheds (Table 2-4). However, the riparian basezones derived from the different spatial resolutions of LiDAR-DEMs vary in area and shape (Table 2-4), especially in creeks and headwater areas (Fig. 2-14 and Fig. 2-15). A negative relationship between the LiDAR-DEM spatial resolution and the total area of the riparian basezone can be detected in both study areas. For instance, the basezone areas in the Miramichi River Basin Watershed range from 1711.66 km^2 (in 30-m resolution) to 2138.5 km^2 (in 10-m resolution) and 3238.17 km^2 (in 3-m resolution) (Table 2-4b).

By visually comparing the shape and extent of the riparian basezones derived from different spatial resolutions of LiDAR DEMs, some patterns were observed. For example, while similar boundary extents were detected for riparian basezones of rivers (i.e. great, medium and small rivers) (Fig. 2-9), more small blank areas (i.e. no riparian basezone delineated) were found within the extents of riparian basezones derived from high-spatial resolution LiDAR DEMs as compared to those derived from lower spatial resolution LiDAR DEMs (Fig. 2-14). Additionally, great differences in extent were detected in the basezones of small streams (i.e. creeks and headwaters), especially between high-spatial resolution LiDAR DEMs (i.e. in 3-m and 5-m resolution) and low-spatial resolution LiDAR DEMs (i.e. in 10-m, 15-m and 30-m) derived small stream basezones (Fig. 2-14 and Fig. 2-15). Thus, the differences in total area of riparian basezones derived from the LiDAR DEMs in different spatial resolutions are largely due to discrepancies in basezone extent in creeks and headwater areas.

For DEM data in the same spatial resolution (30-m) but from different sources (i.e. SRTM and LiDAR), the LiDAR-DEM produced a larger basezone area compared to SRTM-DEM in both study watersheds (Table 2-4). For instance, in the Miramichi River Basin Watershed the total area of riparian basezone derived from 30-m SRTM DEM data and 30-m LiDAR DEM data are 1387.86 km^2 and 1711.66 km^2, respectively, a difference of 323.8 km^2 (~19%). For the analyses based on the same DEM data (i.e. 30-m SRTM DEM) but different hydrological network, the areas of riparian basezone derived from the 1:10,000 NBHN are greater than that derived from the 1:50,000 NHN. For example, in the Lower St. John River Watershed, the total areas of riparian basezone derived from NBHN and NHN are 1928.03 km^2 and 1465.91 km^2, respectively, a difference of 462.12

km^2 (~24%). While the total openwater area calculated from the 30-m NBHN and NHN grids for the Lower St. John River Watershed are 1281.73 km^2 and 910.47 km^2 (a difference of 28%), respectively, reflecting a similar percent difference with the area of riparian basezone.

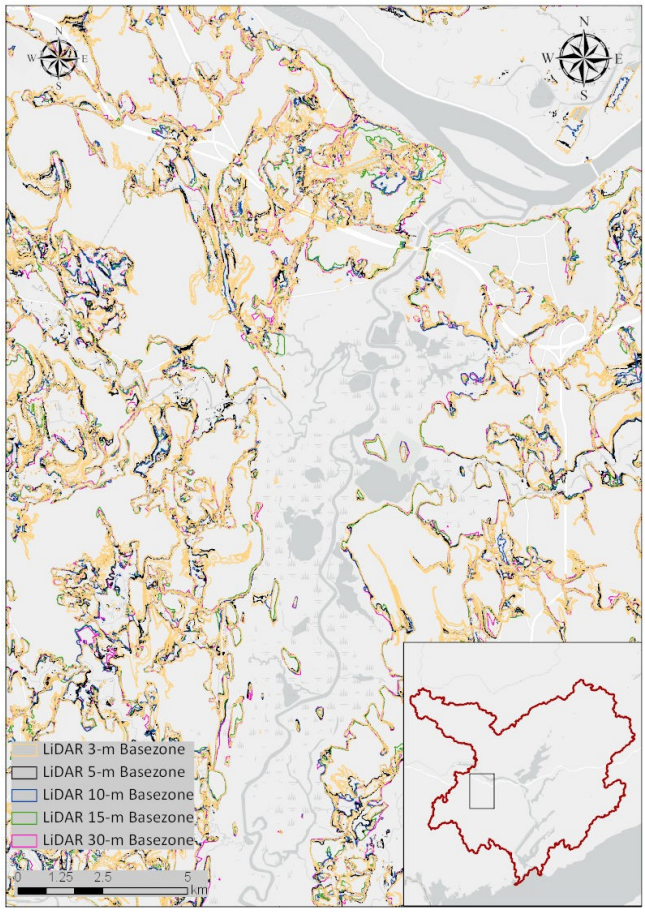

Figure 2-9 Example area of riparian basezone extent in the Lower St, John River Watershed. Different colours represent they were derived from different resolution LiDAR DEMs, which illustrates that different resolution LiDAR DEMs have the similar ability in detecting riparian basezone extent for rivers.

2.3.4 Floodplain and Terrace Separation

The results of floodplain and terraces separation show that high-spatial resolution LiDAR DEM data (i.e. 3-m and 5-m) can provide enough detail about the elevational and horizontal distance changes in the river valley to allow the user to analyze the valley morphology of rivers (i.e. great, medium and small rivers) and visually differentiate the

terraces from the modern floodplains for those rivers (Fig. 2-6). However, high spatial resolution LiDAR-DEMs (i.e. 3-m and 5-m) failed at extracting valley morphology information for small streams (i.e. creeks and headwaters) due to the appearance of excessive surface roughness at local scales (Fig. 2-10) (will be discussed in more detail in Chapter 4), causing a bias in identifying floodplain-terrace transitions. Given this specific bias, separation of the terraces from floodplain for creeks and headwaters was not achieved in this study. The results of floodplain and terraces separation for great, medium and small rivers show that the area of the terrace is smaller than that of the floodplain in all parallel analyses (Table 2-4), meaning the floodplain is the dominant component within the riparian basezone for these rivers (Fig. 2-11). Similar to the floodplain distribution, larger proportions of terraces are located on the "wet" areas in both study areas compared to those on "non-wet" areas (Table 2-4). Additionally, it was found that the extent of terraces was more influenced by DEM spatial resolution in the watershed with less topographical relief, given that the area difference between the 3-m and 5-m DEM derived terraces is greater in the Lower St. John River Watershed as compared to that in the Miramichi River Basin Watershed (Table 2-4).

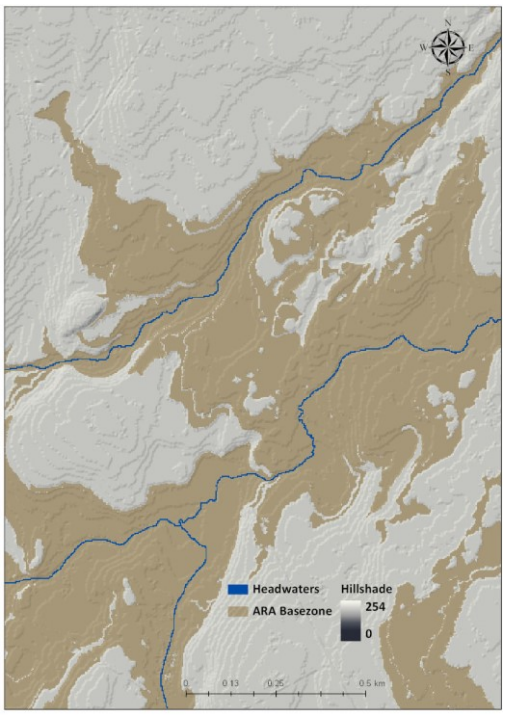

Figure 2-10 Surface roughness at headwater areas in the Miramichi River Basin Watershed (in 3-m resolution). The roughness appearance of high-resolution DEM-derived Hillshade illustrates that there are lots of undesirable "steps" across the high-resolution DEM surface, which causes bias on terraces identification and results in unreasonable wide headwaters basezone (brown area).

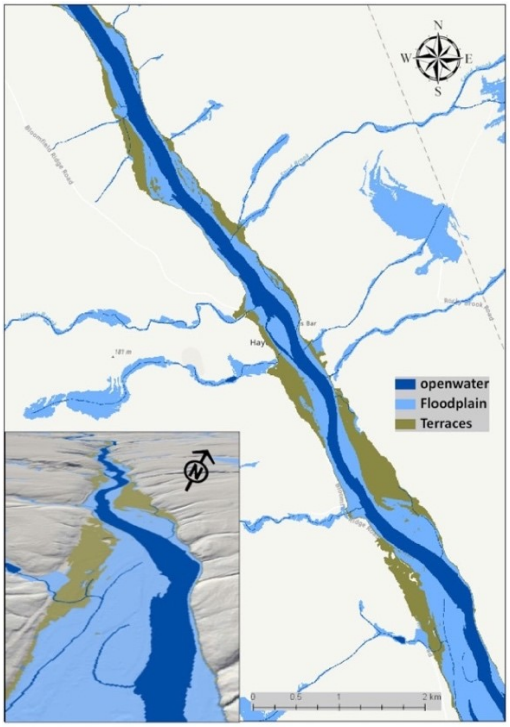

Figure 2-11 Example area of terraces and floodplain separation. The area of floodplain (light blue) is greater than that of the terraces (brown)in riparian basezones.

2.3.5 Riparian Wetlands

The areas of riparian wetlands are largely affected by the spatial resolution and source of DEM data. High spatial resolution LiDAR-DEMs (i.e. 3-m and 5-m DEM) tend to create greater wetland extent compared to low-spatial resolution LiDAR-DEMs (Table 2-4) (Fig. 2-12). The same pattern can be seen in both study watersheds. By visually comparing the riparian wetland extents derived from different spatial resolutions of LiDAR-DEMs, it was found that the extents of high-spatial resolution riparian wetland match better with the provincial wetland inventory compared to the low-spatial resolution LiDAR DEM derived-riparian wetlands (Fig. 2-12). Furthermore, the relationship between the area of riparian wetland and low spatial resolution LiDAR DEMs (i.e. 30-m, 15-m and 10-m) is different in the two study areas. The area of riparian wetland derived from low-spatial resolution LiDAR-DEMs are similar to each other in the Miramichi River Basin Watershed, with the area of 950.78 km^2 (23.52%), 1004.64 km^2 (23.54%), 1041.6 km^2 (23.33%) respectively (Table 2-4b). However, in the Lower St. John River Watershed, the riparian wetlands derived from low-resolution LiDAR DEMs vary in their areas, range from 660.67 km^2 (12.22%) (30-m DEM) to 905.7 km^2 (15.28%) (10-m DEM) (Table 2-4a). For the analyses based on different sources of DEMs (i.e. 30-m LiDAR DEM and 30-m SRTM DEM) and 1:10,000 NBHN, the area of riparian wetland derived from LiDAR-DEM is greater than that derived from SRTM-DEM (Table 2-4). Same pattern is found in both study watersheds.

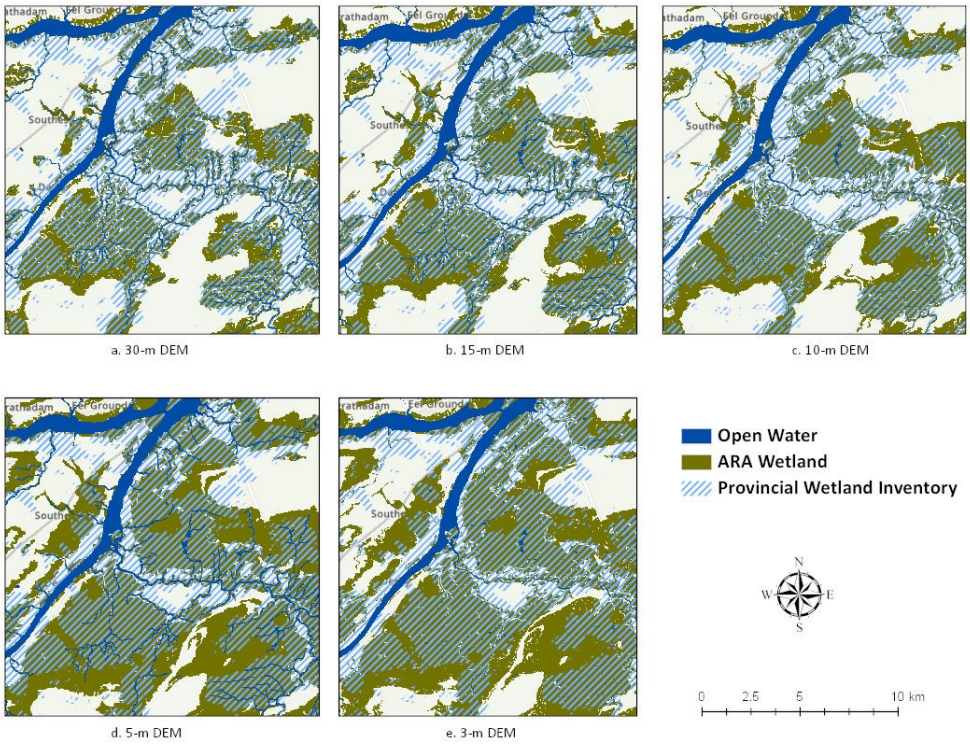

Figure 2-12 Portion of the result of riparian wetlands derived from different resolution LiDAR derived DEMs. The extent of higher-resolution DEM derived riparian wetland (Olive) (d, e) is more consistence with the existing provincial wetland extent (Hatched fill) as compared to the lower resolution LiDAR DEM derived riparian wetland (a, b, c).

2.3.6 Material Contribution Zones (MCZs) Delineation

The results of the steep slope delineation reveal that the steep slope areas are concentrated in relatively small portions of both study watersheds (Fig. 2-13). The steep slope areas derived from different spatial resolution and source DEMs are similar in their general locations but vary in their specific areas and extents (Table 2-4). The area of steep slope MCZs increases as the spatial resolution of LiDAR DEM becomes finer, with the same trend in both study areas (Table 2-4). For example, the area of steep slope MCZs derived from 30-m LiDAR DEM data is 671.7 km^2 and increases to 1003.65 km^2 in 3-m LIDAR DEM analyses in the Lower St. John River Watershed. Additionally, the area of steep slope derived from 1:50,000 NHN is smaller than that derived from 1:10,000 NBHN (based on 30-m SRTM DEM) in both study watersheds (Table 2-4). For

example, in the Lower St. John River Watershed, the areas of steep slope derived from 1:50,000 NHN and 1:10,000 NBHN are 378.64 km^2 and 616.77 km^2, respectively, a difference of 238.13 km^2 (~38%). Meanwhile, the total length of watercourse calculated from the NBHN and NHN for the Lower St. John River Watershed are approximately 18634 km and 12224 km (a difference of 34%), respectively, reflecting a similar percent difference with the area of steep slope.

There is no clear relationship between the DEM sources and resolutions, and the area of 60-m buffer MCZs. This area is designed to pick up the additional narrow areas that are not captured by the other ARA components, so the differences between the 60-m MCZs derived through the different resolutions and sources of DEMs may also be explained by the differences in other ARA components introduced above.

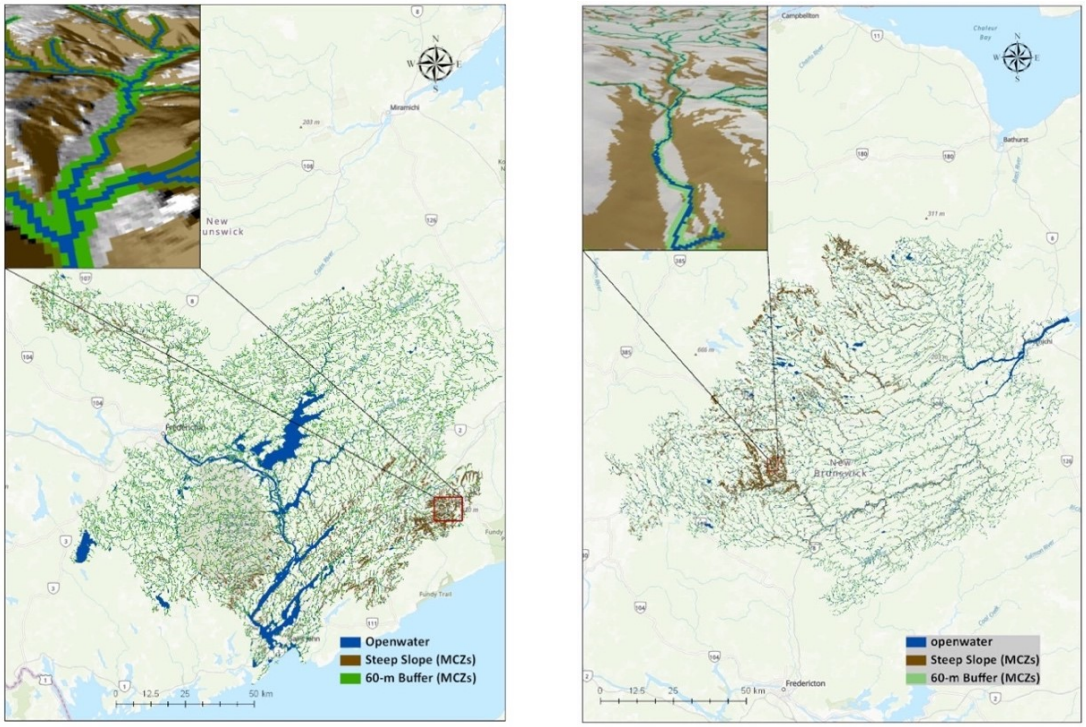

a. Lower St. John River Watershed *b.Miramichi River Basin Watershed*

Figure 2-13 Steep Slope Area derived from 30-m LIDAR DEM data in (a) Lower St. John River Watershed and (b) Miramichi River Basin Watershed. Inset maps are the 3D version of steep slope area in the river valley

Table 2-4 Total Area (sq km) (percentage) for each ARA components by DEM resolution

a. Lower St. John River Watershed

DEM source and resolution	HN scale and source	Openwater	Basezone (Floodplain) (Wet | Non-Wet)		Terraces (Wet | Non-Wet)		Wetland	MCZs (steep slope area)	MCZs (60-m)
SRTM 30-m	1:50,000 NHN	910.47	1465.91				482.99	378.64	384.24
SRTM 30-m	1:10,000 NBHN	1281.73	1240.59	687.44			597.36	616.77	394.62
LiDAR 30-m	1:10,000 NBHN	1281.73	1452.14	881.18			660.67	671.7	459.09
LiDAR 15-m	1:10,000 NBHN	978.3	1993.14	959.43			821.89	802.43	395.94
LiDAR 10-m	1:10,000 NBHN	878.88	2033.78	737.94			905.70	902.72	467.23
LiDAR 5-m	1:10,000 NBHN	782.06	2625.84	504.32	244.47	157.91	1181.33	906.85	418.82
LiDAR 3-m	1:10,000 NBHN	744.16	3246.26	544.78	447.93	206.88	1370.5	1003.65	407.39

b. Miramichi River Basin Watershed

DEM source and resolution	HN scale and source	Openwater	Basezone (Floodplain) (Wet | Non-Wet)		Terraces (Wet | Non-Wet)		Wetland	MCZs (steep slope area)	MCZs (60-m)
SRTM 30-m	1:50,000 NHN	520.38	1030.75				361.00	374.82	357.30
SRTM 30-m	1:10,000 NBHN	573.26	1228.72	159.14			653.51	542.74	196.13
LiDAR 30-m	1:10,000 NBHN	573.26	1474.43	237.23			950.78	622.03	184.49
LiDAR 15-m	1:10,000 NBHN	362.34	1816.63	187.20			1004.64	726.53	170.23
LiDAR 10-m	1:10,000 NBHN	294.5	1994.09	144.41			1041.6	792.17	196.50
LiDAR 5-m	1:10,000 NBHN	228.9	2452.88	94.84	220.31	52.36	1200.37	778.82	178.12
LiDAR 3-m	1:10,000 NBHN	203.2	3075.09	163.08	258.08	57.07	1337.34	883.67	196.03

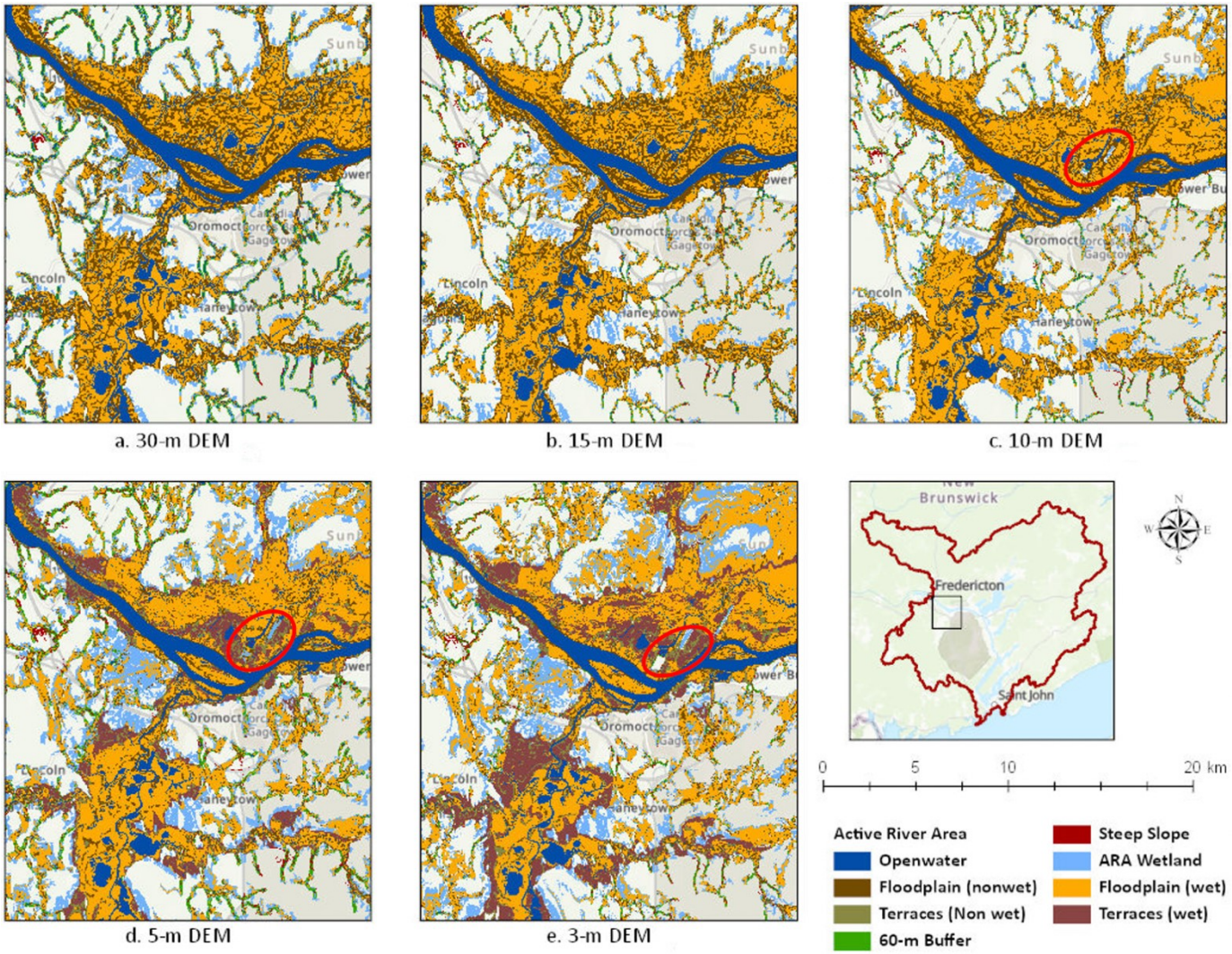

Figure 2-14 Portion of active river area of the Lower St. John River Watershed derived from different resolution LiDAR DEMs. The red circle in the maps (c, d, e) show the example of 'blank areas' in riparian basezones. High resolution DEMs derived ARA results (d, e) have unreasonable wide creeks and headwaters basezone, which covers a large portion of active river areas

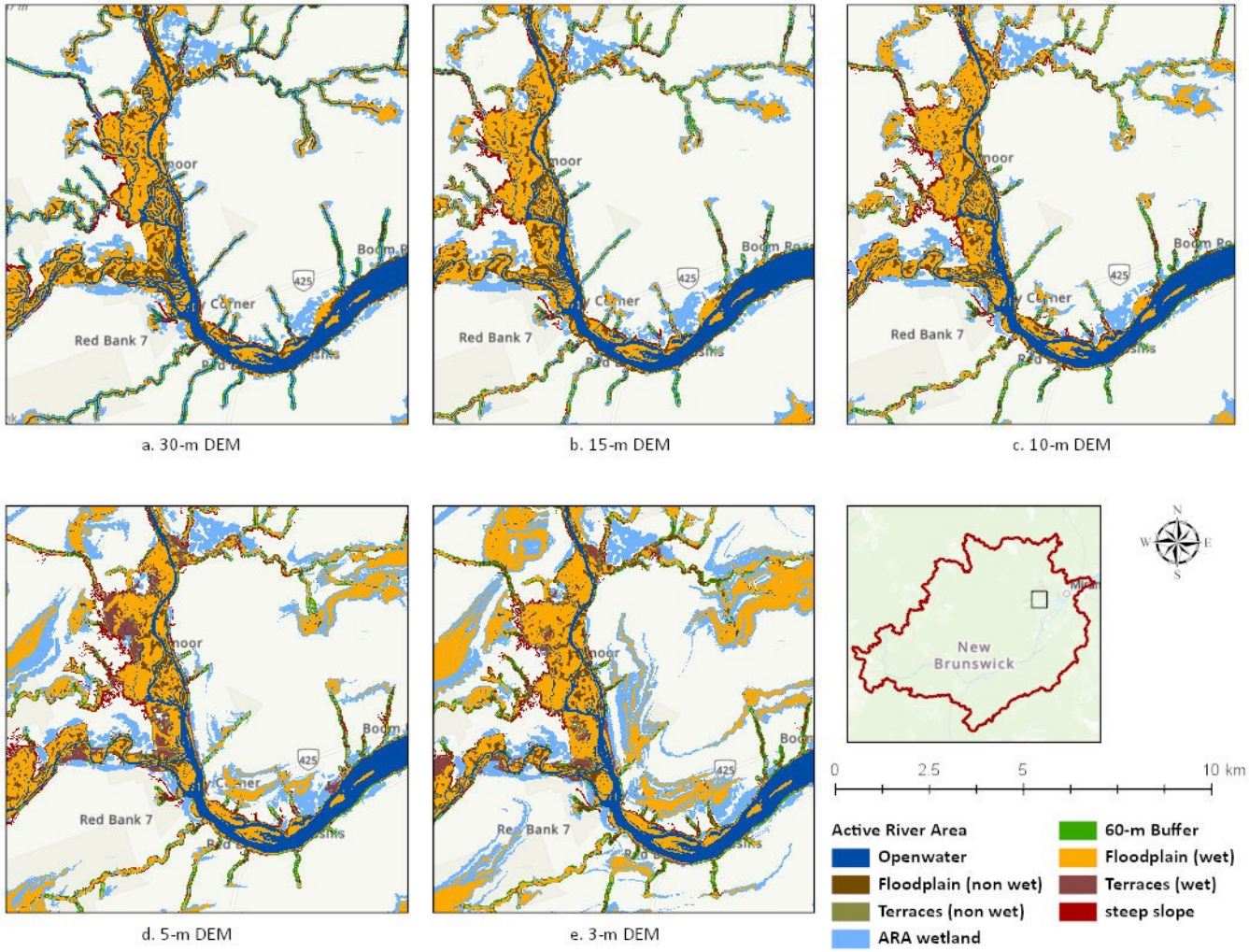

Figure 2-15 Portion of active river area of the Miramichi River Basin Watershed derived from different resolution LiDAR DEMs. High resolution DEMs derived ARA results (d, e) have unreasonable wide creeks and headwaters basezone which covers a large portion of active river areas

2.4 Discussion

The analysis in this study have produced important results. The ARA components derived from the parallel analyses vary in both study watersheds in response to differences in spatial resolution and source of DEM data and scale and source of hydrological network. This result is not surprising, as the influence of these factors has been well documented in the literature (Poppenga et al., 2009; Barber & Shortridge, 2005; Johansen et al., 2011). Nonetheless, understanding the nuances and causes of these differences is important to choosing the most appropriate scales and resolutions of data for future ARA delineation across broader (eco-) regions.

The area of openwater is a directly observable feature and thus should be readily detectable, yet the total areas of openwater differ distinctly across the parallel analyses because of differences in spatial resolution of the input LiDAR-DEM. In raster-based studies (i.e. ARA delineation), all input data, such as the hydrological network, need to be converted into raster format at the same resolution with the input elevation data. Fine-scaled features, such as creeks and headwaters with average bankfull widths of 8-m and 4-m, respectively (Conservation Gateway, n.d.), are overpredicted by the watercourse grids lower than 3-m and/or 5-m spatial resolutions, since the minimum bankfull width that low-spatial resolution watercourse grids can represent is their own resolution (e.g., 10-m and 30-m). Thus, high-spatial resolution data will provide a more accurate representation of openwater area, as the first step in the ARA delineation process. Additionally, differences in terms of openwater area were also detected between the analyses based on the same SRTM DEM data but different hydrological networks (i.e. 1:50,000 NHN and 1:10,000 NBHN). These differences are due to the fact that the

provincial hydrological network (i.e. 1:10,000 NBHN) have the ability to represent the location of creeks and headwaters and can allow users to more precisely calculate the area of openwater, while the low-resolution national hydrological network (i.e. 1:50,000 NHN) eliminates many small-scale creeks and headwaters, thereby excluding these small streams from the ARA delineation. Such limitation of the low-spatial resolution hydrological network also partially explains why the area of 1:50,000 NHN derived ARA results (Nussey and Noseworthy, 2020) are generally smaller than those of 1:10,000 NBHN-derived ARA results.

The majority of basezone areas are located on the "wet" area in all parallel studies. This is to be expected, since the riparian basezones are generally low-gradient areas with hydric soils, which have the same features as riparian wetlands, and thus there is a lot of overlap between riparian basezones and riparian wetlands. Such overlapping areas are considered important in conservation planning because highly productive and diverse riparian plant communities tend to establish themselves in areas with rich alluvial soils (Smith et al., 2008). Low spatial resolution LiDAR DEMs and SRTM DEM derived riparian wetland, however, may underpredict the extent of riparian wetland and the overlap areas between riparian basezone areas and riparian wetlands, since the area and extent of wetlands derived from low spatial resolution LiDAR and SRTM DEMs are smaller than that derived from higher spatial resolution LiDAR DEMs in both study watersheds (Table 2-4).

Different spatial resolution LiDAR DEMs turn out to have the similar ability in terms of modelling the extent of riparian basezone for great, medium and small rivers at the macro spatial scale (Fig. 2-9). High spatial resolution LiDAR DEM data, however,

can generate more detailed basezone boundaries that better match the natural shape of the valley wall given its small cell size. Accordingly, it is reasonable to conclude that high spatial resolution LiDAR DEM data can more precisely but not more accurately model the extent of riparian basezone. Additionally, more blank areas (i.e. no riparian basezone delineated) were found within the extent of riparian basezone derived from high-spatial resolution LiDAR DEM data (Fig. 2-14). By visually inspecting the aerial photo of those blank areas, it was evident that most of the blank areas are human infrastructural features with a sharp boundary. Because high-spatial resolution LiDAR DEM data can generate more detailed slope grid and have the ability to model subtle topographic transitions, human infrastructure with a sharp boundary can be represented and will receive high cost distance value at the cost surface modelling stage, which will ultimately exclude them from the extent of riparian basezone. Accordingly, it is reasonable to suspect that low spatial resolution LiDAR DEMs will overpredict the riparian basezone extent at certain areas (e.g. human encroachment areas).

Although, high-spatial resolution LiDAR-DEM can more precisely model the extent of riparian basezone and delineate the flood-free areas, raw high-spatial resolution LiDAR DEMs are inappropriate for local-scale (i.e. creeks and headwaters) riparian basezone delineation, resulting in undesirable surface roughness (Fig. 2-10), which causes unreasonably wide creeks and headwaters basezone, as was the case in the high-spatial resolution LiDAR DEMs result (Fig 2-14 and Fig 2-15). Through the visual inspection, the widths of creeks and headwaters modelled by high-spatial resolution LiDAR DEMs (i.e. in 3-m and 5-m resolution) are much greater than the general widths of creek and headwater floodplains, reported as ranging from 5m to 50m (Benda et al.,

2007). Furthermore, many creek and headwater basezones are connected to each other and cover a large portion of the watersheds, thereby magnifying the problem of overprediction. Together, these explain why the area of riparian basezone derived from high-spatial resolution LiDAR DEMs is greater than that from low-spatial resolution LiDAR and SRTM DEMs.

Steep slope MCZs are designed to pick up riverine land areas with slopes greater than 15% percent rise. The accuracy of the DEM-derived slope grid is important to the steep slope area delineation. As mentioned previously, high-spatial resolution LiDAR DEM data can generate more detailed slope grid and pick up the subtle topographic change on the bare earth, while low spatial resolution LiDAR DEMs and SRTM DEM will eliminate subtle topographic transitions when converting into slope grids. Given this limitation, only extremely steep slope areas will be identified from the low-resolution slope grids, while less steep sloped area will remain undetected and thus excluded from the steep slope MCZs delineation, which is the reason why the area of steep slope MCZs is greater in the high-spatial resolution than in the lower spatial resolution steep slope MCZs.

In order to address the two gaps in ARA studies, this study tests (i) the performance of high-spatial resolution LiDAR DEMs in terms of separating terraces from floodplains based on the ARA framework, and (ii) whether high-spatial resolution LiDAR DEM data can achieve higher accuracy than low-spatial resolution LiDAR- DEM and commonly used SRTM-DEM in ARA results. The differences in the results of the seven parallel analyses in terms of the spatial extent of the ARA components inform whether high-spatial resolution LiDAR DEM data and high-spatial resolution

hydrological network (1:10,000 NBHN) can achieve high accuracy results as compared to low-spatial resolution LiDAR DEM, low-spatial resolution SRTM DEM, and the coarse national hydrological network (i.e. 1:50,000 NHN).

2.5. Conclusion

This chapter introduced the methods developed and applied for delineating the ARA and its components in two study watersheds in NB. Key components included: development of a new method for terrace and floodplain separation; delineation of the extent of riparian basezone, riparian wetland and MCZs based on the original ARA framework; separation of terraces from modern floodplain based on the refined ARA framework, integrating the new methodology; and comparison of the area and extent of ARA components derived from different spatial resolutions and sources of DEMs and scales of hydrological network.

The results reveal that the area and extent of different ARA components are largely affected by the source and spatial resolution of DEM data as well as the spatial resolution of input hydrological network. It was found that the high-resolution LiDAR DEM data can benefit the active river area delineation, but it is not without its limitations. High-spatial resolution LiDAR DEM data can accurately summarize the area of openwater across the study areas. Additionally, the extent of riparian wetland derived from high-resolution LiDAR DEMs match better with the extent of provincial wetland and hydric soil inventory, allowing for accurate identification of these areas, which are areas of conservation priority.

High-spatial resolution LiDAR DEM data can more precisely but not more accurately delineate the riparian basezone for great, medium and small rivers compared to low-spatial resolution LiDAR and SRTM DEMs, and it can also create more detailed and accurate slope grid and spatial-explicit delineation of flood-free areas and incorporate more steep-slope MCZs into the final ARA output. Raw high-spatial resolution LiDAR DEM, however, is inappropriate for the creeks and headwaters basezone delineation due to the excessive surface roughness which causes unreasonably wide creek and headwater basezones, resulting in a large riparian basezone area across both study watersheds. Furthermore, the surface roughness caused by high-spatial resolution DEM data at local scales makes the valley morphology of creeks and headwaters difficult to analyze, and thus the developed ARA-based floodplain and terraces separation framework failed to differentiate the terraces from modern floodplains for creeks and headwaters. Appropriate DEM smoothing algorithms should be found and applied to reduce the surface roughness of high-spatial resolution LiDAR DEM-derived products before delineating the active river area (will be discussed in Chapter 4).

Chapter 3. Meander Belt Delineation: Developing an ARA-Based Framework for Channel Migration Extent

3.1 Introduction

Rivers are dynamic features within active river areas (Smith et al., 2008). Their configuration and position on riparian basezones change continuously in time as part of river meander evolution, development, and migration processes (Parish Geomorphic, 2014). Continuous channel migration is expected as the associated flow and sediment transportation maintain the linkages among different ARA components and contribute to diverse riparian functions (Smith et al., 2008). However, when rivers change their shape and shift in their positions within meander belts, the associated erosion and sediment deposition can cause loss or damage to human properties and/or structures adjacent to rivers (Rapp and Abbe, 2003). To maintain meander migration and fluvial erosional processes while at the same time endeavoring to reduce risks to human communities, the extent of meander belts should be quantified and delineated to guide development along and adjacent active river areas. Limiting development within the meander belt extent can reduce costs of repairing and replacing public infrastructure and/or privately-owned property that might otherwise be threatened or damaged by meander migration (Rapp and Abbe, 2003). Quantifying the extent of meander migration can also provide guidance in reducing degradation and loss of important riparian functions, helping assure that physical and ecological processes (e.g. sediment movement and organic materials transportation) within active river areas are accommodated (Rapp and Abbe, 2003; Smith et al., 2008).

Despite its importance, a review of the literature suggests a lack of consensus on methods for meander belt delineation (Howett, 2017; Parish Geomorphic, 2014). At the time of writing, no ARA related studies have successfully identified the extents of meander belts in active river areas, making the ARA framework weak at informing fluvial erosion hazard management practices (Smith et al., 2008; Marangelo and Farrell, 2010; Nussey and Noseworthy, 2020). The extent of the meander belt under the ARA framework refers to the cross-channel distance that spans the outer edges of existing or potential meanders (Smith et al., 2008), and is controlled by interactions of spatial variables such as flow regime and riverbank materials (i.e. soil lithology) (Kline and Dolan, 2008). Due to the inherent variability of these factors, the meander extent will vary between adjacent watercourses and along the drainage network of specific watercourses. Furthermore, temporal variability in these spatial processes can occur through time, a consequence of natural changes or human activities (e.g. urbanization and storm water management) (Mcgrane, 2016). Whenever one or more spatial or temporal variables that influence meander pattern are altered, adjustments to the meander belt are expected to occur. These unpredictable spatial and temporal variables present challenges to estimating the extent of meander migration (Parish Geomorphic, 2004).

Currently, the most commonly used meander belt delineation method is to analyze the historical dynamics of a watercourse to predict future channel migration behaviour and areas at risk of channel movement (Lagasse et al., 2004; Piegay et al., 2005). Such analyses rely on the evaluation of channel processes that occur within multi-temporal contexts (Rapp and Abbe, 2003). Historical data, including topographic maps and aerial imageries, have been successfully applied to identify the rate of channel mobility and

channel migration extent in many meander assessment studies. For example, Rapp and Abbe (2003) identified rates of erosion and directional movement of meanders, as well as physical characteristics surrounding the watercourse in Washington State by overlaying historical aerial photographs and comparing previous configurations of the watercourse. A study by Biron et al. (2014) modelled the horizonal rates of fluvial erosion for a wide array of rivers in Quebec by generating quantitative representations of channel migration from transects across multiple years of channel configurations. Historical analyses, however, must be conducted in a data rich environment, with most studies suggesting that at least 50 years of remote sensing data are necessary to reveal meaningful trends in channel migration (Gurnell, 1997; Ham and Church, 2000). If historical data is insufficient or unavailable, intensive field work must be carried out to reconstruct past channel movement and rates of channel erosion (Rapp and Abbe, 2003). Moreover, historical analyses only document geographic changes that are subject to temporal variables, from which on-the-ground channel processes are inferred. Historical analyses do not explicitly account for the effects of spatial variables (e.g. valley setting and riverbank lithology etc.) on channel migration behavior along the watercourse (Rapp and Abbe, 2003).

To properly determine the extent of the meander belt within active river areas, spatial variables need to be integrated into delineation procedures (Howett, 2017), since the natural meandering pattern that occurs on each individual river reach is heavily dependent on the physical characteristics of the valley section in which the river reach is situated (Kline and Dolan, 2008). River reaches refer to the lengths of channel that display similarity with respect to hydrological conditions, riparian basezone materials and

valley settings (Donovan, 2015). Given that all controlling and modifying influences of the watercourse are similar at the reach scale, it is expected that all menders within the reach could respond in a similar way (i.e. similar meander pattern) and occupy a similar position in the riparian basezone (Parish Geomorphic, 2004). River meander pattern and migration extent are cumulative functions of local settings of different river reaches along a watercourse. For example, if riparian basezone materials (i.e. riverbank lithology) and valley setting are relatively homogeneous among different river reaches, then a regular meander pattern occurs along the watercourse; a regular meander pattern implies that all meanders in a sequence of meanders are similar in radius, shape and frequency. When any of the physical controlling variables differ across reaches, the meander pattern tends to be irregular (Parish Geomorphic, 2004). As the physical characteristics of reaches are always different in the real world (Hickin and Nanson, 1975), meander patterns along the watercourse are, most often, characterized by asymmetry and irregularity (Hooke, 1984). For instance, reaches within wider valleys with erodible basezone materials have more space and ability to meander than those situated within confined valleys comprised of more solid materials. High gradient reaches associated with resistant bedrock are usually highly confined with low sinuosity, whereas low gradient reaches which have greater opportunity for lateral migration (Sheldon et al., 2015). Given variations in physical characteristics and meander processes along a watercourse and similarities in meander patterns and migration extents at the reach scale, the extent of the meander belt should be separately defined for each river reach rather than for an entire river.

The objective of this chapter is to introduce a framework developed and utilized for meander belt delineation in order to address a weakness in current ARA studies. The

framework takes into consideration the differences in physical characteristics between reaches along the watercourse. Its applicability was tested in the two study watersheds in New Brunswick (i.e. Lower St. John River Watershed, and Miramichi River Basin Watershed). Firstly, the method for meander-reach-separation parameter (i.e. river sinuosity, riverbank lithology, valley confinement, stream gradient) measurement and meander belt delineation will be described, followed by the example result of meander belt delineation. The advantage and limitations of the developed meander belt delineation approach will then be discussed. Since creeks and headwaters often have steep gradients and small water discharge volumes (USEPA n.d.), they are less likely to form great extents of meander belts. Thus, for test purposes, the meander belt delineation framework was applied only to great, medium and small rivers, and not to the creeks and headwaters, in the study watersheds.

3.2 Materials and Method

Information about the dataset and methodology for delineating meander belt extent is introduced in this section. Spatial parameters and procedures for reach separation are first described, followed by the method for delineating the meander migration extent for each reach.

3.2.1 Data Acquisition and Preparation

The input datasets for meander belt delineation include 1-m LiDAR-derived DEM data, New Brunswick Hydrographic Network (NBHN), provincial forest soil data, NCC upstream drainage area, and 10-m LiDAR-DEM derived riparian basezone extent (Table 3-1). The riparian basezone extent and NCC upstream drainage area were applied to

measure the valley confinement ratio. As previously discussed in chapter 2, the riparian basezone extents of great, medium and small rivers derived from different spatial resolutions of DEM data are similar to each other, and thus the 10-m DEM derived basezone extent was applied to meander belt delineation as a comprise between precision and data processing effort. Given that several upstream flowlines in NB cross into Maine and Quebec, high-resolution cross-border hydrological network data is challenging to acquire and fit to the NBHN. As a consequence, this study did not calculate the upstream drainage area based on NBHN, and instead used the drainage area derived by NCC from the national hydrological network (i.e. 1:50,000 NHN) (Millar et al., 2009). The NCC-derived drainage area was applied to calculate the river bankfull width (see section 3.2.4).

Table 3-1 Brief descriptions of applied datasets

Dataset	Brief Description	Original Format	Responsible Agency	Source
LiDAR-derived DEM	LiDAR-derived DEMs in 1-m resolution in New Brunswick Stereographic Double Projection.	GeoTiff (.tif)	GNB	http://geonb.snb.ca/nbdem/ (Date: 2019-05-31)
NBHN	Surface drainage features including rivers, streams, lakes, islands, and watershed boundaries including names for many rivers and streams.	Shapefile (.shp)	ERD	http://www.snb.ca/geonb1/e/DC/NBHN.asp (Date:2018-08-29)
Forest Soils	Polygons of Forest Soils Units, including information on drainage, slope, and aspect.	Shapefile (.shp)	ERD	http://www.snb.ca/geonb1/e/DC/forestsoils.asp (Date:2015-08-18)
NCC-upstream drainage area	A layer of the hydrology with the drainage area information.	Shapefile (.shp)	NCC	(Assessed Date:2019-10-25)

NBHN provides a connected line network through the watercourses that comprise each watershed (DataQC, 2009). Junction features (i.e. vector points) can be found associated with the NBHN flowline where two or more watercourse segments intersect (DataQC, 2009), or where a watercourse segment enters into a lake, pond, or reservoir. In this chapter, each of these individual watercourse segments is referred to as a 'NBHN hydrologically meaningful reach' so as to distinguish it from a 'river meander reach'. The NBHN hydrologically meaningful reach is the basic unit for the measurement of the following meander-reach-separation-parameters (i.e. river sinuosity and stream gradient).

The provincial forest soil composition was measured by New Brunswick Department of Natural Recourses and Energy by integrating interpretations of previously published soil survey and surficial geology maps (Colpitts et al., 1995). The basic unit of this dataset is the forest soil unit, which is defined as a "naturally occurring segment of the regolith with distinct lithology characterized by the overlaying parent material and solum" (Colpitts et al., 1995, p15). The primary lithology information of each soil unit can be found in the attribute table of the dataset.

3.2.2 River Sinuosity

The sinuosity of a river is a measure of the degree of complexity or curvilinearity displayed within a meandering channel (Andrle, 1996). It is a comprehensive result of riverbank lithology configuration, valley confinement setting and hydrological conditions (Zhang et al., 2008). For instance, in a low-gradient channel, the overall stream power is usually low, and if the stream has resistant bank materials, there will be little erosion on both sides of the channel and the channel remains relatively static with low sinuosity value (e.g. the sinuosity of a straight river is 1). However, when the stream power is great

enough and the underlying bank materials are erodible, bank erosion will increase, initiating the formation of meander belts with high sinuosity values (Saadi and Zekkos, 2013). Thus, river sinuosity can be used as an indicator at the reach scale of the ability of a river to meander in response to local physical characteristics (Zhang et al., 2008). River sinuosity is recognized as the most straightforward parameter for separating rivers into different reaches (Parish Geomorphic, 2004), and is used accordingly in this study.

River sinuosity is commonly measured as a ratio between the length along a channel and the length of the valley (i.e. straight-line distance between the start point and the end point) within a given reach (Fig. 3-1) (Ferguson, 1975). The length of the valley was measured by calculating the Euclidean distance between the start and end point of a NBHN hydrologically meaningful reach, while the length of each hydrologically meaningful reach can be found in the attribute table of the NBHN dataset. Once the sinuosity was measured for each hydrologically meaningful reach across the two study watersheds, the sinuosity ratio thresholds (Table 3-2) were determined by reviewing a commonly used sinuosity index (Charlton, 2008) and conducting benchmark analyses to make sure the applied thresholds can successfully separate the flowlines into three different stream types (i.e. low-, moderate-, and high-sinuosity) based on their sinuosity value. However, sinuosity alone cannot necessarily separate a river into different meander reaches as there are numerous channel configurations which are possible for a given sinuosity value (Hooke and Yorke, 2010) (Fig. 3-2). To address this limitation, three physical parameters were measured separately: riverbank lithology, valley confinement ratio, and stream gradient. Each is described as follows.

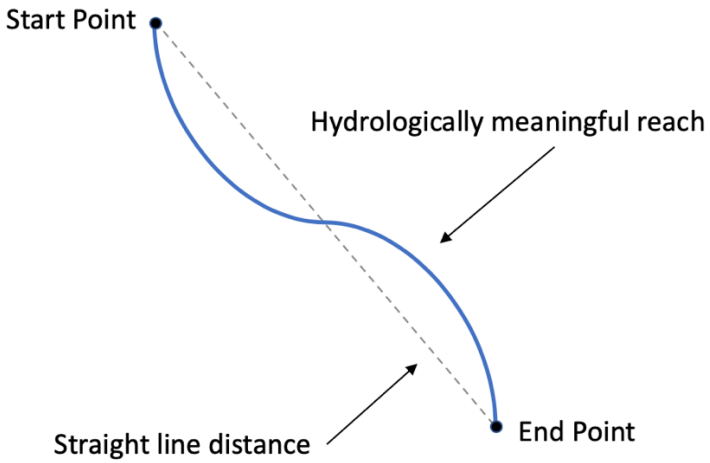

$$\text{River Sinuosity} = \frac{\text{Length of hydrologically meaningful reach}}{\text{Length of straight line distance}}$$

Figure 3-1 River sinuosity is measured as a ratio between the length along a hydrologically meaningful reach (blue line) to the straight line distance (dash line) between the start point and the end point of that reach.

Table 3-2 River sinuosity ratio thresholds. Source: Charlton, 2008

Description	Sinuosity Ratio Value
Low Sinuosity	≤ 1.01
Moderate Sinuosity	> 1.01 and ≤ 1.2
High Sinuosity	> 1.2

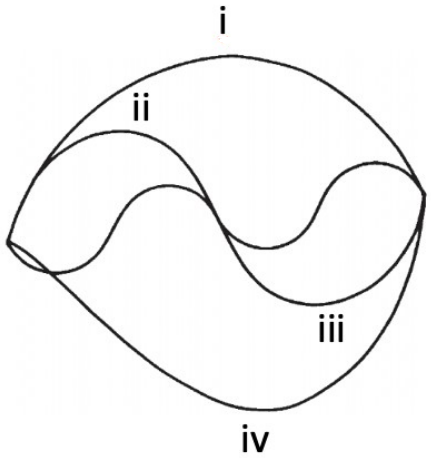

Figure 3-2 An example shows different channel configurations (i.e. i,ii,iii,iv) for sinuosity index of 1.5 (Image adapted from Hey. 1976).

3.2.3 Riverbank Lithology

Meander is the result of the dynamic equilibrium between riverbank erosion and downstream sediment deposition which is subject to the ever-changing flow discharge rate (Neuendorf et al., 2005). Meander pattern and meander migration extent are influenced by riverbank erosion and sediment deposition rates which are deeply controlled by riverbank material composition (Petrovszki et al., 2012; Zaimes et al., 2004). For instance, in a rigid channel with resistant riverbank material, the variation in flow discharge has to be accommodated within the physical dimensions of the fixed channel geometry, resulting in limited meander migration extent with low sinuosity value. Alluvial channels situated in the riparian basezone with erodible bank materials, however, can accommodate changes in the imposed flow discharge by eroding their banks and forming greater meander extents with high river sinuosity values (Cameron and Bauer, 2014).

The riverbank lithology configurations were derived from the provincial forest soil dataset. The soil units have already been grouped in the dataset according to their primary lithology or the mineralogical composition of their parent material (i.e. the rocks in the soil) by the data provider (Colpitts et al., 1995) (Appendix B). Different riverbank soil units in the study watersheds were reorganized into different lithology categories and represented by their primary lithology types in ArcGIS Pro™ (ESRI, 2008) (Fig. 3-3) for the future use in separating the river meander reaches.

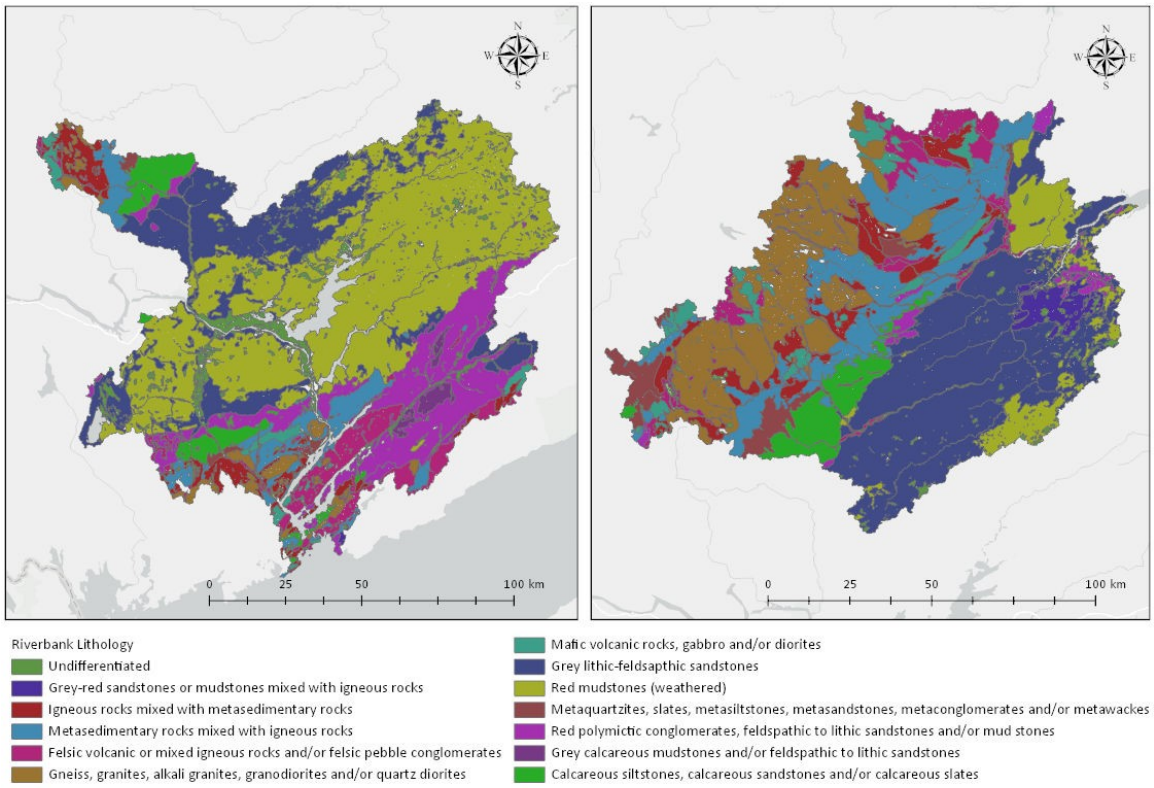

Figure 3-3 Riverbank lithology configurations of the Lower St. John River Watershed (left), and the Miramichi River Basin Watershed (right).

3.2.4 Valley Confinement Ratio

Valley confinement ratio describes the degree to which bounding topographic features, such as hillslopes, limit the lateral extent of the riparian basezone and channel migration along a river (Nagel et al., 2014). River valleys can be broadly classified as confined and unconfined with corresponding differences in their appearance, topographic gradient and stream characteristics (Fig. 3-4). Confined valleys in mountain basins are typically narrow, with little alluvial fill. These valleys have relatively steep gradients and contain coarse-grained sediments. Rivers situated in confined valleys have little to no opportunity to develop great extents of meander belt (Fig. 3-4 a and b). In contrast, unconfined valleys are usually composed of fine alluvium and susceptible to bank erosion, with broad riparian basezones that allow active channel migration and the

development of channel sinuosity or braiding (Nagel et al., 2014; Sheldon et al., 2015) (Fig. 3-4 c and d).

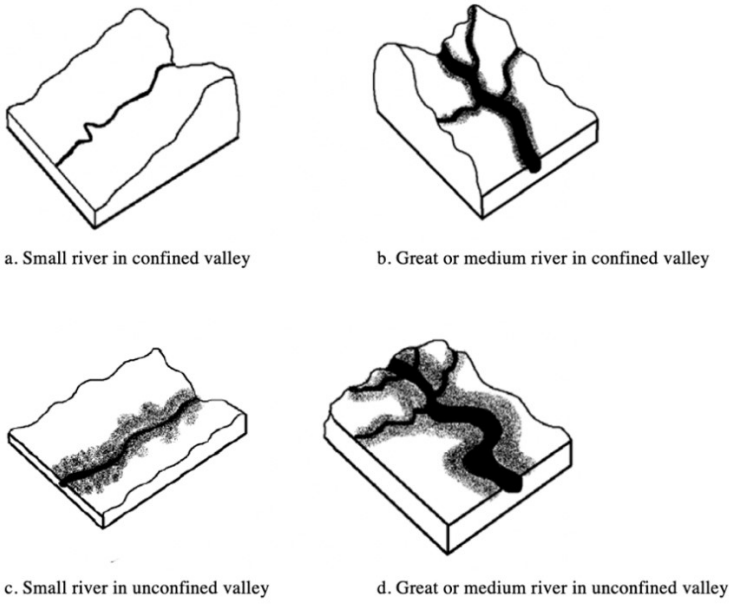

Figure 3-4 Schematic maps of four different river valley confinement types, including small river in confined valley (a), great or medium river in confined valley (b), small river in unconfined valley (c), and great or medium river in unconfined valley (d) (Image adapted from K. Weaver, TNC).

Valley confinement ratios were quantified by comparing the widths of the riparian basezones to those of the open water channels for the rivers in the study watersheds, following the guideline of a previous TNC stream classification study (Sheldon et al., 2015). A higher confinement ratio indicates a wider riparian basezone available for channel meandering and migration and thus less confinement. The width of riparian basezone was continuously measured using the maximum of four axes in a series of flow accumulation (i.e. N-S, E-W, NE-SW, NW-SE) (Sheldon et al., 2015). Firstly, eight raster grid layers were created based on the extent of 10-m DEM-derived ARA riparian basezone; each of them was assigned as a single D-8 flow direction value (i.e. 1(E), 2(NE), 4(S) ,8(SW), 16(W), 32(NE), 64(N), 128(NE)) to indicate their fake directions. The “flow accumulation” geoprocessing tool was then separately applied to each of the

eight grid layers to calculate the width (in number of cells) of ARA riparian basezone in the direction indicated by the fake direction value. If all the ARA riparian basezone grids in one of the eight layers are represented by only one direction value (e.g. 4), the "flow accumulation" command will only sum the number of accumulated cells in that direction (i.e. South). After this, eight flow accumulation grid layers were added perpendicularly and diagonally to get the total width of riparian basezone by taking the maximum value of the sum grids in the four major directions (i.e. E-W, NW-SE, NE-SW, N-S) with the aid of "cell statistics" tool.

The bankfull widths of open water channels were estimated based on their drainage areas and the location of ecoregion or more specifically, physical characteristics of the ecoregion. The relationship between river bankfull width and their upstream drainage area can be expressed as the formula (Faustini et al., 2009),

$$w = \alpha A^{\beta}$$

Equation 3-1

Where w is the river bankfull width in meter, A is the drainage area in km^2, α and β are empirical parameters controlled by physical characteristics of the ecoregion. The coefficient α is primarily related to precipitation (i.e. the greater the precipitation—or more specifically, runoff—the higher the value of α), while coefficient β is largely the function of regional geology, as well as topography and climate (Faustini et al., 2009). This formulation assumes that, within a limited geographic area having relatively uniform geology and climate, drainage area is the dominant control on discharge (Faustini et al., 2009). The empirical coefficient values applied in this study for α and β were 2.55 and 0.39 respectively, which were tested by Faustini et al. (2009) for the US portion of the Northern Appalachian / Acadian Ecoregion through extensive field surveys. Since the

study watersheds for this project are situated within the Canadian portion of the same ecoregion (separated only by the Canada-USA boundary), it is expected that they have a similar physical geography setting and the empirical coefficients tested for the USA portion are suitable for application in the Canadian portion.

With the river bankfull width continuously measured along the entire drainage network with the aid of NCC upstream drainage area information and river bankfull width formula, NHN flowline grids in 10-m resolution were then generated with the value of each cell in the calculated width of that NHN flowline segment. It is expected that the issue of dissimilarity in hydrological network resolution is negligible, since the major discrepancies between low (i.e. 1:50,000 NHN) and fine resolution hydrological network (i.e. 1:10,000 NBHN) are in creeks and headwater areas which are not included in the meander delineation step. The valley confinement ratio was then calculated by comparing the maximum width of riparian basezone grids from the four major directions to the width of the NHN river flowline. After this, each 10-m flowline pixel was assigned a confinement ratio and then classified into one of the confinement categories based on the valley confinement thresholds (Table 3-3). The thresholds were determined by reviewing the thresholds applied in the TNC stream classification study (Sheldon et al., 2015) and comparing them to known examples in the study watersheds in order to make sure the applied thresholds can successfully separate the river valley into two different confinement types (i.e. confined and unconfined) based on their valley confinement ratio.

Table 3-3 Description of confinement classes

Description	**Valley confinement thresholds (Ratio ARA width to river bankfull width)**
Confined	0-3
Unconfined	> 3

3.2.5 Stream Gradient

Stream gradient influences river sinuosity and meander migration extent at the reach scale due to its influence on stream bed morphology, flow velocity, sediment transport, substrate and grain size (Montgomery and Buffington, 1993). For instance, high gradient streams have substrates of cobble, boulders and/or bedrock, while low gradient streams typically have substrates of fine sediment such as sand, gravel, or cobble with a tendency to be carried by water flow. As a result, high gradient streams are always dominated by cascade to plane-bed channel morphology with low sinuosity and limited meander extent as opposed to low gradient channel systems which are dominated by riffle-pool channel morphology with moderate to high sinuosity and greater meander migration extent (Rosgen, 1996).

The variable "percent slope" (Fig. 3-5) is a unitless ratio calculated as the change in elevation divided by distance (Sheldon et al., 2015; Millar et al., 2019). It was applied as a measure of stream gradient to each hydrological meaningful NBHN flowline. DEM elevation values were extracted for the start and end points of each flowline, the change in elevation was calculated, and the difference was then divided by the length of the flowline to get the stream gradient. It was found that approximately 0.5% of flowlines have a negative slope value, which was due to errors in NBHN and resampled 10-m LiDAR DEM data caused by instream infrastructure (e.g. bridges, culverts). To rectify the negative slope value, the percent slope was re-calculated for the error flowlines using maximum and minimum elevation along each respective flowlines' length instead of start and end points, following a method developed by NCC (Millar et al., 2019).

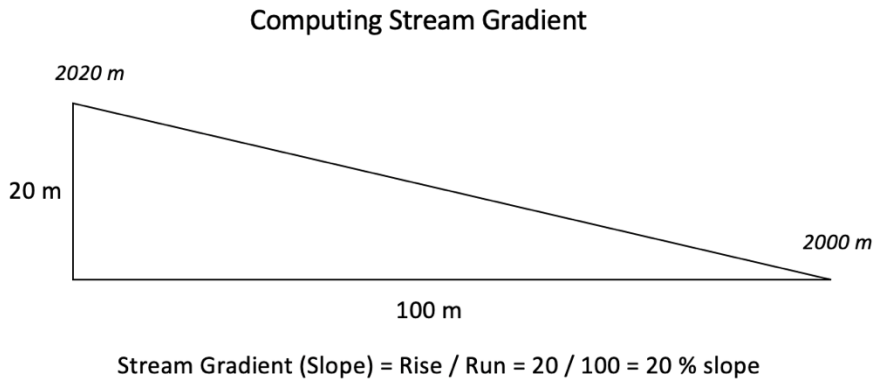

Figure 3-5 An example illustrating the calculation of stream gradient.

The stream gradient thresholds (Table 3-4) were adopted from a stream classification study conducted by NCC in the same ecoregion (Millar et al., 2019). Millar et al. (2019) chose the thresholds by comparing the classes with stream gradients at known locations and with Rosgen's (1996) slope classes, and by examining the distribution of freshwater species across different watercourse gradients.

Table 3-4 Stream gradient classes

Description	Stream gradient (%)
Low Gradient	≤ 0.1
Moderate Gradient	> 0.1 and ≤ 2
High Gradient	> 2

3.2.6 Meander Reach Separation and Manual Meander Belt Delineation

To identify watercourse sections with similar meander pattern and local physical settings for meander belt delineation, each river was separated into different meander reaches based on the four parameters (i.e. river sinuosity, riverbank lithology, valley confinement and stream gradient) as measured in the preceding steps. If dissimilarity was detected in any parameter between two watercourse sections, these two watercourse sections were identified as different meander reaches. As introduced in the previous sections, the valley confinement setting, and stream gradient heavily control the lateral

migration ability of watercourses; high-gradient rivers situated in confined valleys are less likely to form great extent of meander belts since the valley wall is considered to be a constraint to meander migration (Parish Geomorphic, 2004). Thus, it is expected that the meander migration extent of the rivers with certain features are highly consistent with the range of river valley in which they are situated (i.e. riparian basezone) (Parish Geomorphic, 2004; Kline and Dolan, 2008). In contrast, meander migration extent of low to moderate gradient rivers situated in the unconfined valley is less consistent. Given the meander migration features of rivers situated in confined and unconfined valleys, a manual meander delineation procedure was only conducted on low to moderate gradient rivers situated in unconfined valleys in the study watersheds.

In order to model complex meander migration patterns on a GIS platform, meander morphology was simplified by the Meander Centerline (MCL), which is a line used to represent the general down-valley orientation of the meander pattern (Parish Geomorphic, 2014; Kline and Dolan, 2008). The river meander belt is essentially centered around the MCL (Parish Geomorphic, 2004), and thus its location is important to the identification of the meander belt in active river areas. Following the Vermont River Corridor Protection Guideline (Kline and Dolan, 2008), the MCL is created on reaches where the river has an opportunity to meander (i.e. low to moderate gradient reaches situated in unconfined valleys) by identifying and connecting the meander crossover points on the river channel (i.e. NBHN flowline). The meander crossover point is a point of inflection or the point where river channel curve changes from concave to convex (Fig. 3-6). In this study, meander crossover points were added on the NBHN

flowlines where the deepest thread of water "crosses over" from the outside bank of one meander to the opposite bank on the next meander downstream.

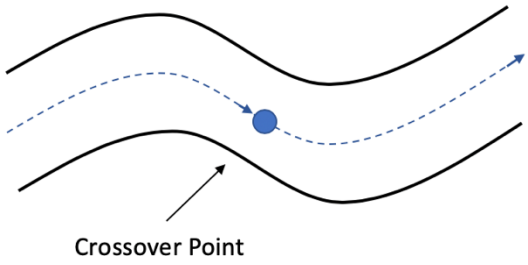

Figure3-6 Schematic map shows the location of meander crossover point on the river channel. The blue dash line indicates the deepest thread of water as it crosses over from the outside bank of one meander to the opposite bank on the next meander downstream; arrows indicate the direction of river flow.

While the locations of crossover points can be readily identified on the NBHN flowlines with regular meander patterns, they are more complex to find when the meander pattern is irregular or compound. For instance, where there are no discernible equilibrium-scaled meanders, and the channel was historically straightened back and forth across the valley, placing crossover points only at morphology inflections would result in a laterally over-extended meander extent (Fig. 3-7a). Carson and Lapointe (1983) suggested that MCL should retain the large river bend and follow the primary meander pattern when simplifying the river channel as the meander belts are expected to shift in position mainly along the primary meander pattern. Accordingly, crossover points should be added to large river bends to allow the MCL to represent the primary meander curve (Fig. 3-7b). In contrast, where a channel is just starting to form youthful meanders and none of the river bends have developed to equilibrium length and radius, the MCL should not be built with cross-over points at every micro inflection (Fig. 3-7c). In these cases, some crossover points should be eliminated to help achieve a simplified river morphology (Fig. 3-7d) (Kline and Dolan, 2008).

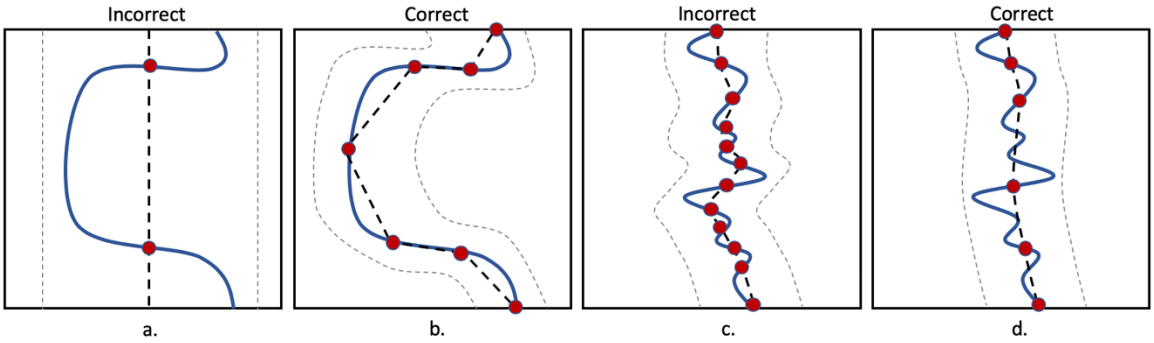

Figure 3-7 Schematic maps illustrate how to identify the location of crossover points(red dots) and MCLs (black dash lines) for different types of river channel (blue line), including an incorrect example of adding crossover points only at morphology inflections for a large river bend (a), a correct example of crossover points and MCL that follow the primary meander pattern (b), an incorrect example of adding crossover points at every micro-inflection (c), and a correct example of crossover points and MCL that properly simplify the river channel (d).

These procedures were applied to identify meander cross-over points and MCLs of river reaches in the study watersheds. Once the MCL was identified for each reach, the lateral meander migration extent was quantified. Based on the definition of meander belt under the ARA framework (i.e. cross-channel distance that spans the outside-most edges of existing or potential meanders [Smith et al., 2008]), the limits of the meander belt were defined by parallel lines drawn tangential to the outer most river bend for each river mender reach. To identify the location of the parallel lines on both sides of the river channel, the horizontal distance between the MCL and the outer most point of each reach was measured, and the meander buffer was then created on both sides of the MCL based on the measured distance. Given that the outer most river bend represents the greatest lateral meander migration extent under the control of local physical characteristics at the reach scale, it is expected that the remaining river bends in the same reach with the same controlling variables are less likely to meander beyond this lateral extent.

Finally, since the initiative for active river area meander belt delineation is to identify land areas that are prone to fluvial erosion and may influence runoff patterns and sediment discharges, it would make little sense to conserve an area on the valley side-

slope, and thus the extent of meander belt should not extend laterally beyond the toe of valley walls (Kline and Dolan, 2008). To ensure the final meander migration extent lies within the extent of the river valley bottom, the extent of the riparian basezone was used to delimit the final extent of the river meander belt.

3.3 Results

The results of meander-reach-separation-parameter measurements (i.e. river sinuosity, valley confinement, and stream gradient), meander reach separation, and meander belt delineation are presented. Since the meander delineation framework is based on the reach scale, the reach separation and meander belt delineation results are difficult to present for the entire study watershed. For these, an example river serves to demonstrate the results.

3.3.1 Meander-Reach-Separation-Parameter Measurements

River Sinuosity

The vast majority (94.8% and 96.4%) of rivers in the two study areas have moderate to high sinuosity values (Table 3-5). The portion of rivers with low sinuosity (i.e. sinuosity ≤ 1.01) is relatively low (3.6% and 5.2%), and since straight rivers are rare in nature, many of them are a result of human structural controls (Wang and Ni, 2002).

Portions of the results of river sinuosity measurements for the Lower St. John River Watershed and the Miramichi River Basin Watershed are shown in Figure 3-8. Red lines represent river channels with high sinuosity, while blue lines represent those with moderate sinuosity. Through visual inspection, it is evident that most of the red lines are found in small river areas, which means sinuosity values of tributaries (i.e. rivers with the

stream order of 4 and 5) are generally higher than those of main stems (i.e. rivers with the stream order of 6, 7, and 8). High sinuosity values indicate that small rivers are generally formed by multiple small river bends with small radius curvature, and thus the meander migration extents of small rivers are smaller than those of great and medium rivers at the reach scale. Additionally, due to spatial variability in the modifying and controlling influences of meander patterns, two watercourse sections situated immediately up / downstream of each other could show differences in sinuosity (Fig. 3-8, Inset maps).

Table 3-5 The percentages of different river sinuosity types in the two study areas

River sinuosity type	Total stream length (percentage)	
	Lower St. River Watershed	Miramichi River Basin Watershed
Low sinuosity	5.2%	3.6%
Moderate sinuosity	50.9%	62.6%
High sinuosity	43.9%	33.8%

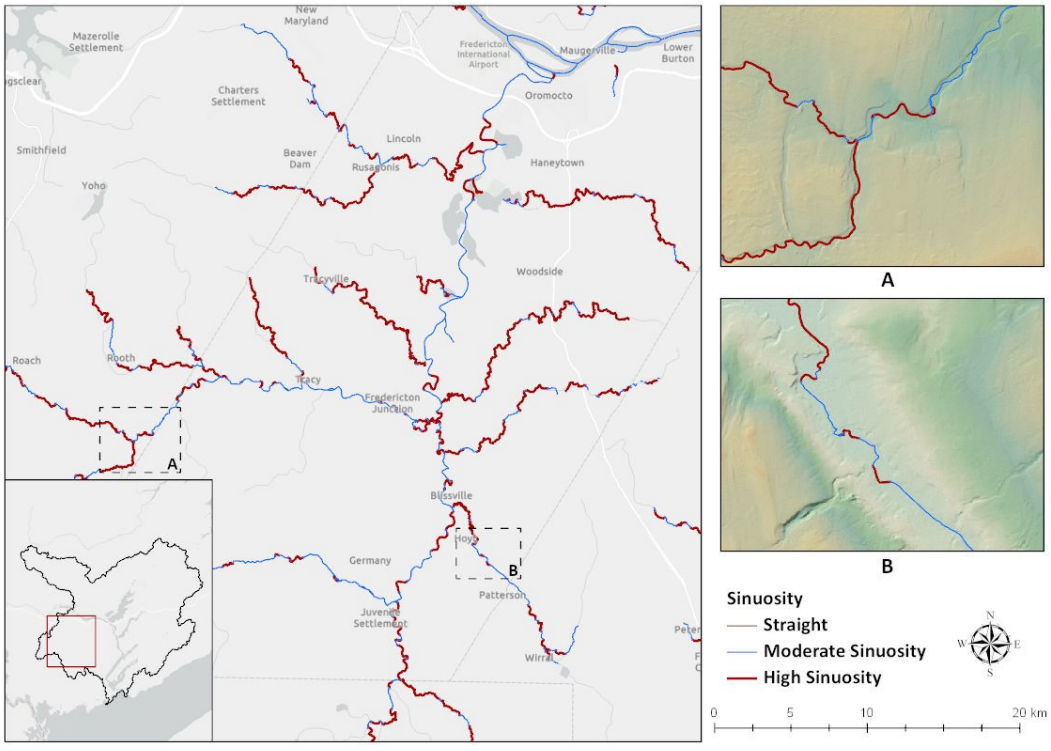

a. Example area of river sinuosity measurement in the Lower St. John River Watershed

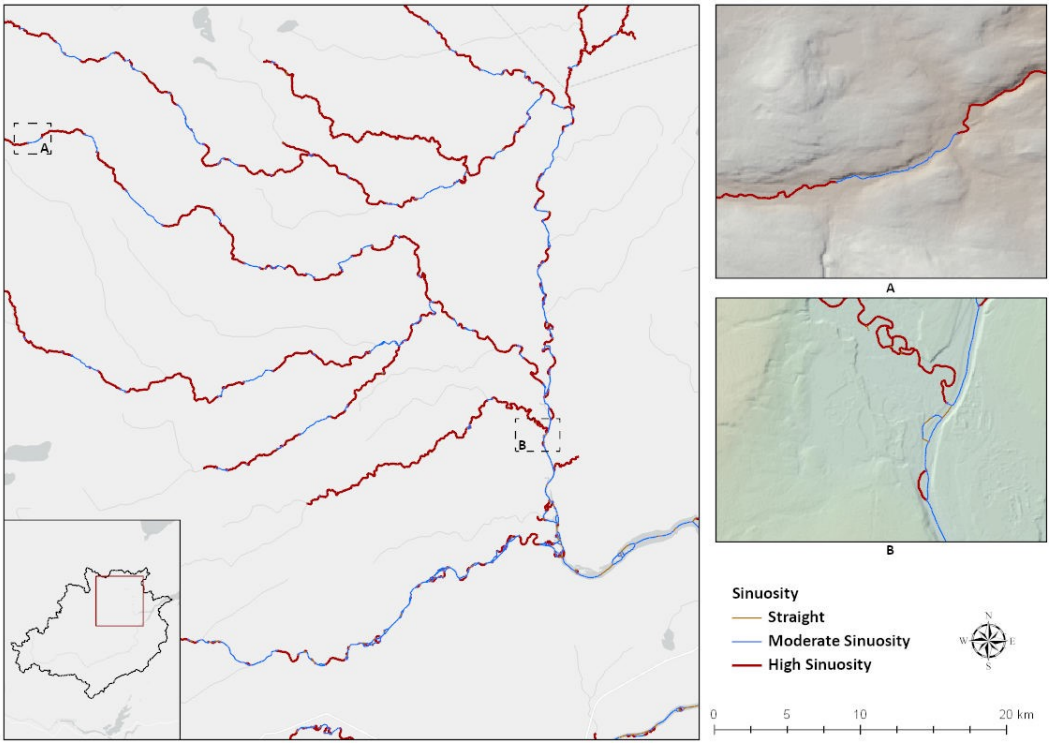

b. Example area of river sinuosity measurement in the Miramichi River Basin Watershed

Figure 3-8 Portion of results of river sinuosity measurement for (a) Lower St. John River Watershed and (b) Miramichi River Basin Watershed. Two watercourse sections situated immediately up/downstream of each other could show differences in sinuosity due to the spatial variability in the modifying and controlling influences of meander pattern (Inset maps A, B).

Valley Confinement

Given greater topographic relief in the Miramichi River Basin Watershed, the proportion of rivers situated in its confined valleys is greater than in the Lower St. John River Watershed, at 50.7% and 33.9% respectively (Table 3-6). In the Lower St. John River Watershed, the portion of rivers situated in unconfined valleys is greater than that situated in confined valleys, at 66.1% and 33.9% respectively (Table 3-6), reflecting the wide valley bottoms of its two main rivers (i.e. Lower St. John River and Oromocto River).

Figure 3-9 presents the results of valley confinement measurements for Lower St. John River Watershed and Miramichi River Basin Watershed. As shown in the inset map,

rivers situated in confined valleys have narrow riparian basezones and limited space to form river meander extents. Their potential meander extent is therefore highly consistent with the extent of the riparian basezone. In contrast, broader riparian basezone areas with extensive alluvial fill can be found in unconfined valleys, which allow active channel migration and the development of channel sinuosity. Valley confinement type is highly subject to variations in local topographic setting; two watercourse sections situated immediately up / downstream of each other could show differences in confinement type due to the variation in their local valley bottom width (Fig. 3-9b, Inset maps).

Table 3-6 The percentage of different valley confinement types in the two study watersheds

Valley confinement type	Total stream length (percentage)	
	Lower St. John River Watershed	Miramichi River Basin Watershed
Confined	33.9%	50.7%
Unconfined	66.1%	49.3%

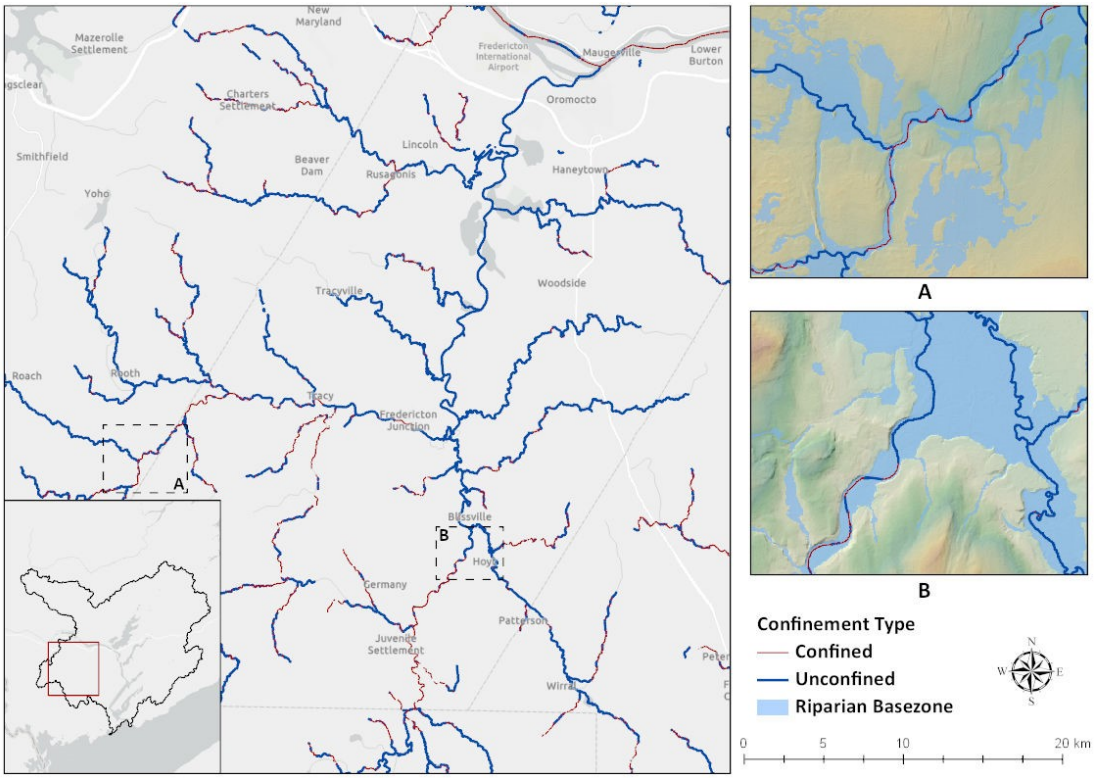

a. Example area of valley confinement measurement in the Lower St. John River Watershed

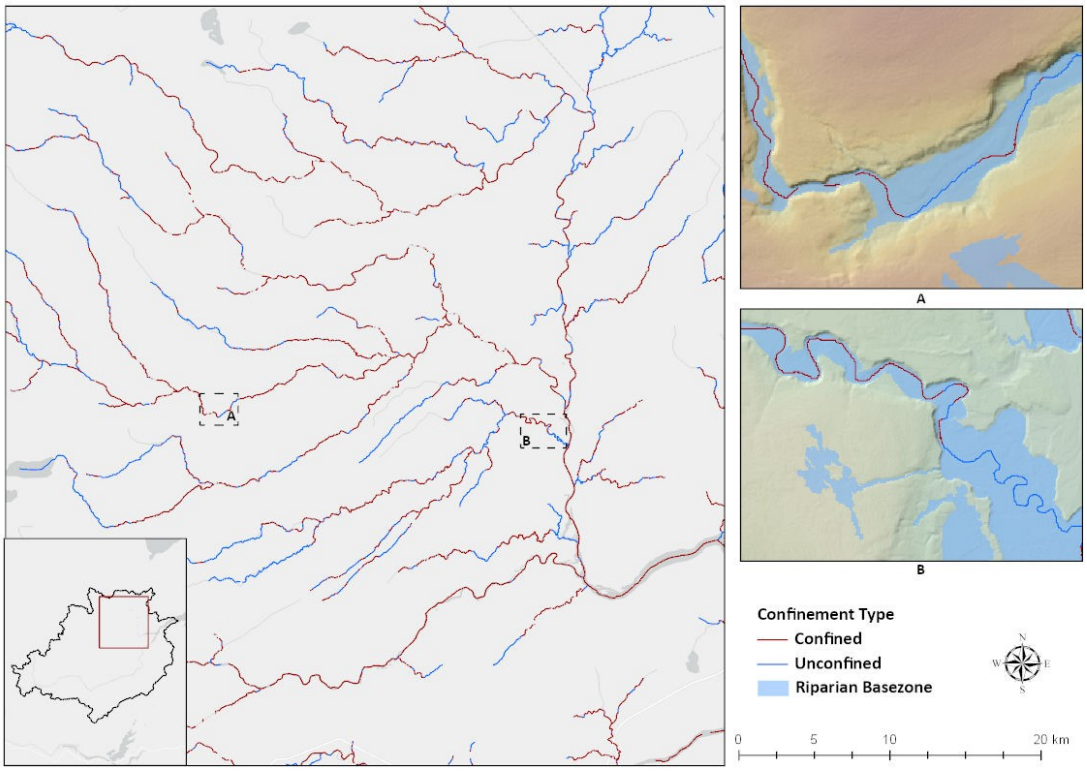

b. Example area of valley confinement measurement in the Miramichi River Basin Watershed

Figure 3-9 Portion of the result of valley confinement measurement for (a) Lower St. John River Watershed and (b) Miramichi River Basin Watershed. The red lines represent rivers situated in confined valleys, while blue lines represent rivers situated in unconfined valleys. Two watercourse sections situated immediately up/downstream of each other could show differences in confinement type due to the variation in their local valley bottom width (Inset Maps A, B).

Stream Gradient

Most examined rivers have moderate to low gradient values (Table 3-7); the portions of high gradient rivers are relatively low in both study watersheds as they are always found in creeks and headwater areas in the upper watersheds (Open Oregon, n.d.). Although rivers may occasionally have stretches with high-gradients (at 1.8% and 9.77%, respectively), such as waterfalls, at the scale of the stream gradient measurement, high-gradient rivers would likely have been errors originating from the DEM (Millar et al., 2019). Due to the higher topographic relief in the Miramichi River Basin Watershed, the percentages of moderate- and low-gradient stream lengths differ, at 63.4% and 26.83%

respectively. In contrast, the percentages of moderate- and low-gradient stream lengths are more similar in the Lower St. John River Watershed.

The distribution of stream gradients in the watersheds is presented in Figure 3-10. Visual inspection confirms that moderate and high gradient rivers tend to have steep, narrow valleys with limited space for river channel meandering (Fig. 3-10, Inset maps). The meander pattern of high and moderate gradient rivers is highly constrained by the shape of the river valley. In contrast, low gradient streams have wider river valley bottoms (i.e. riparian basezone), with a tendency for the streams to meander (Fig. 3-10a, Inset Maps A, B). Additionally, the majority of moderate and high gradient rivers can be found in small river areas, while most low gradient rivers of medium or great size are situated in unconfined valleys in the lower watershed (Fig. 3-10a).

Table 3-7 The percentage of different stream gradient type in the two study areas

Stream gradient type	Total stream length (percentage)	
	Lower St. John River Watershed	Miramichi River Basin Watershed
Low gradient	44.6%	26.83%
Moderate gradient	53.6%	63.4%
High gradient	1.8%	9.77%

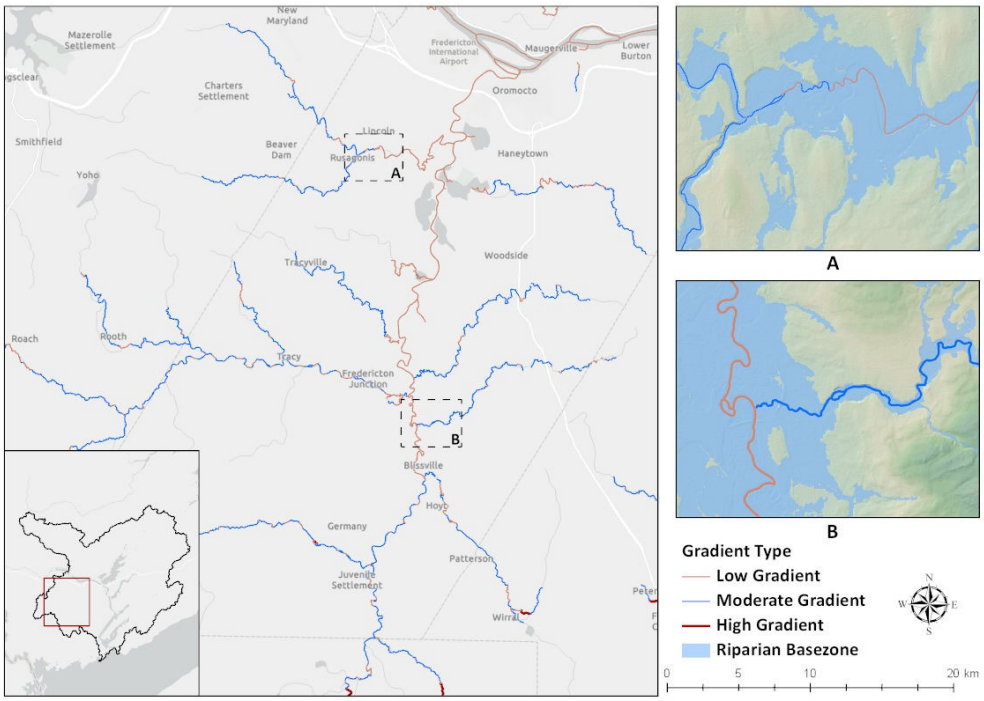

a. Example area of stream gradient measurement in the Lower St. John River Watershed

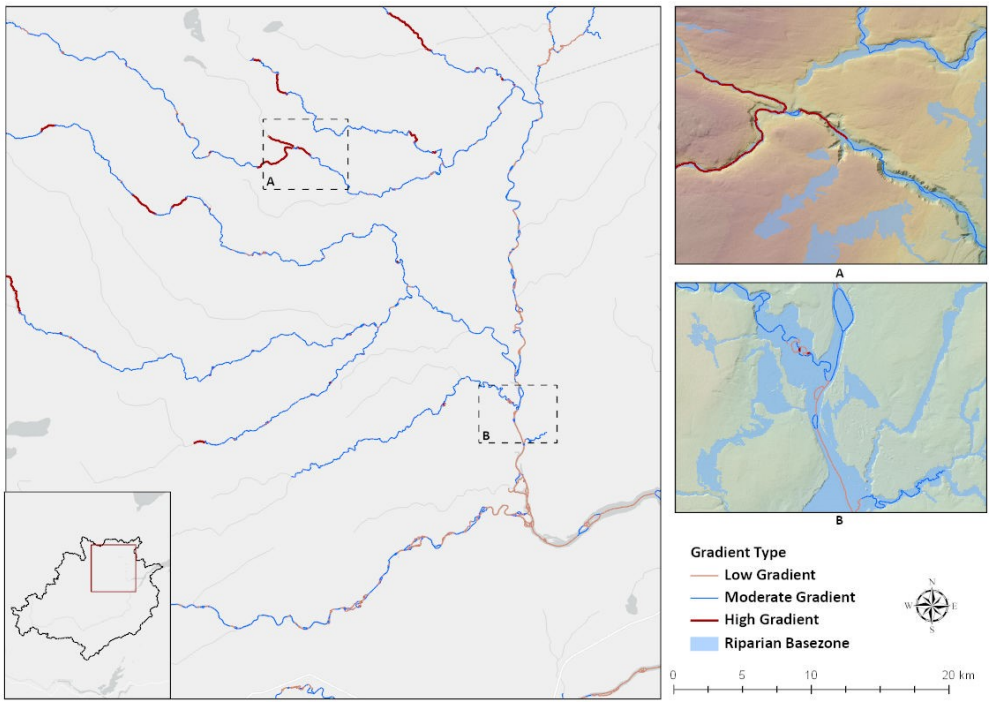

b. Example area of stream gradient measurement in the Miramichi River Basin Watershed

Figure 3-10 Portion of the distribution of the result of stream gradient measurement for (a) Lower St. John River Watershed and (b) Miramichi River Basin Watershed. Orange lines represent rivers with low gradients, while blue lines and red lines represent moderate and high gradient rivers, respectively. Due to the elevation change ratio vary along the river network, two adjacent watercourses could vary in their stream gradient setting (Inset Map). Streams with low gradient are always located in wide riparian basezones (blue area) (a. Inset Maps), while streams with moderate to high gradient are always located in narrow riparian basezones (blue area) (b. Inset Maps).

3.3.2 Meander Reach Separation

Meander reach separation results, including the local physical setting and sinuosity type of each meander reach for all rivers in the study watersheds, are presented in Appendix C. In this section, meander reach separation results are demonstrated through the example of the North Branch of the Oromocto River in the Lower St. John River Watershed (Fig. 3-11). As shown in this example, reach breaks were identified through variations in river sinuosity, soil lithology, valley confinement and stream gradient setting (Table 3-8). The soil lithology types for reaches 1 and 2 are Grey Lithic-feldsapthic Sandstones and Red Mudstones, respectively, while reach 3 is alluvial deposition with undifferentiated lithology type, among which the alluvial deposition is the most erodible riverbank material (Geotech, n.d.) (see Appendix B for the full list of lithology types and descriptions). Accordingly, it is reasonable to expect that the widest meander belt will be found in reach 3 if other parameters remain consistent along the watercourse. Additionally, among the three different meander reaches, reaches 1 and 3 are located in unconfined valleys with moderate and low gradients (Table 3-8), and thus the manual meander belt delineation procedure was conducted only on these reaches.

Table 3-8 North Branch Oromocto River reach physical setting

Reach	Soil Lithology	Stream Gradient	Valley Confinement	River Sinuosity
Reach 1	8	Moderate gradient	Unconfine	High Sinuosity
Reach 2	9	Moderate gradient	Confine	Moderate Sinuosity
Reach 3	1	Low gradient	unconfine	Moderate Sinuosity

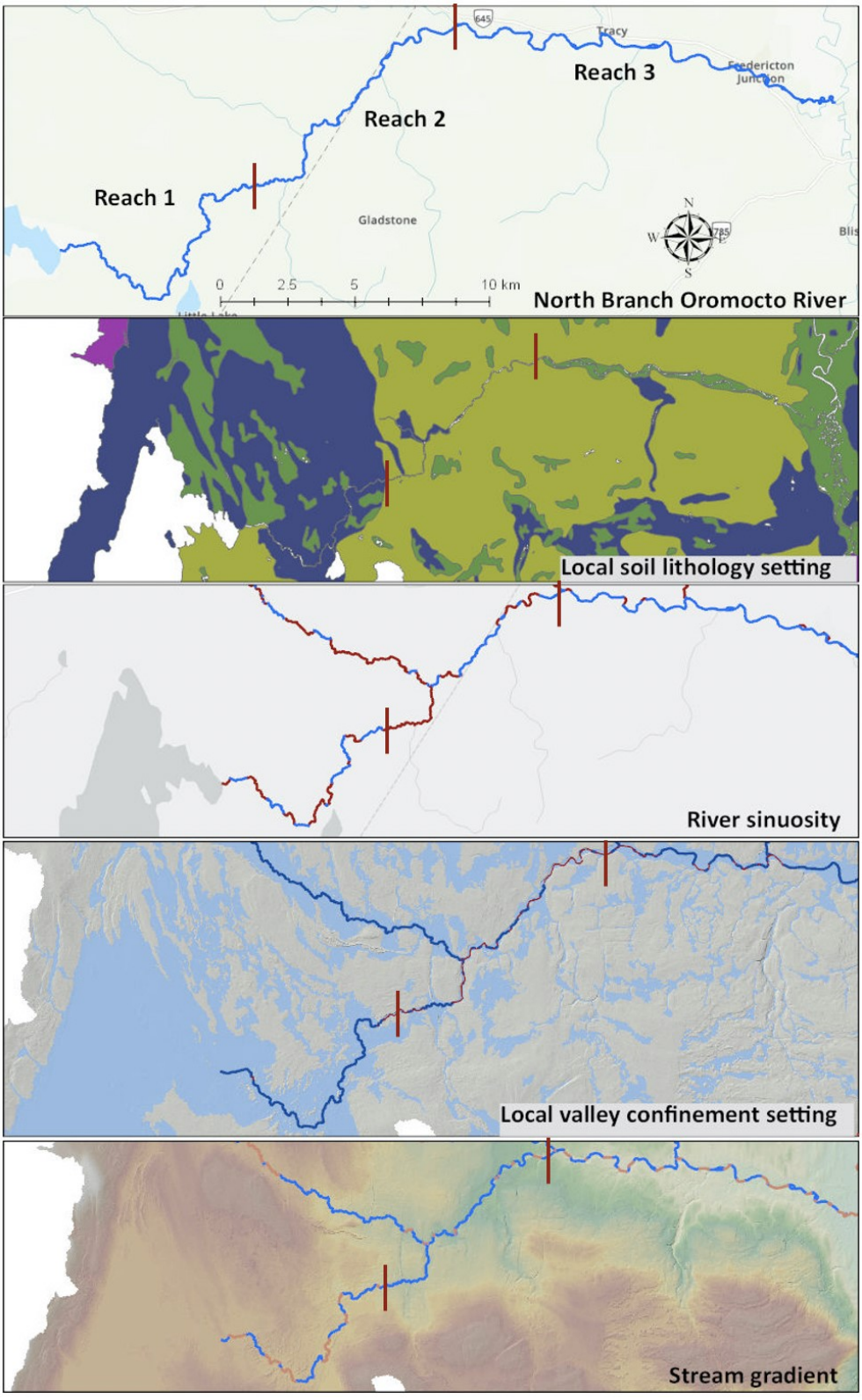

Figure 3-11 Meander reach separation of the example river. Reach breaks (red lines) were placed due to the variation in local soil lithology setting, river sinuosity, valley confinement setting and stream gradient setting.

3.3.3 Manually Meander Belt Delineation

The location of MCLs were determined for reaches 1 and 3 of North Branch Oromocto River by connecting the crossover points on the NBHN flowlines (Fig. 3-12). Through visual inspection, it is apparent that the two reaches have different meander patterns. Reach 3 has a regular meander pattern and the MCL follows the general down-valley trend of the river channel; reach 1 has an irregular meander pattern and the MCL follows the primary pattern, which gradually shifts downstream and eliminates micro-inflections (Fig. 3-12).

Meander belt delineations on reaches 1 and 3 are drawn as parallel lines that encompass the meander tendencies of the reach, centred around the MCL (Fig. 3-12). The meander belt width measured for reaches 1 and 3 are 330m and 520m, respectively, which reflects the differences in terms of riverbank material erodibility between the two reaches, with the latter being more erodible. The approximate river-bankfull width of reaches 1 and 3 measured from satellite imagery are 50m and 60m, respectively. The relationship between the meander belt width and river bankfull width is similar to the finding of a previous study (Williams, 1986), in which the relationship is expressed by an empirical formula (i.e. $B = 3.7W^{1.12}$), where B is the belt width and W is the river bankfull width. When the areas within the preliminary meander migration extent but outside the basezone extent were eliminated (as described in section 3.2.6), the final meander migration extents are limited to the extents of river valley bottom (i.e. riparian basezone) (Fig. 3-12).

The total areas of meander migration extent measured for the Lower St. John River Watershed and Miramichi River Basin Watershed are 491.45 km^2 and 170.32 km^2,

respectively. Great differences in terms of meander migration and potential fluvial erosion extent were detected between the two study areas, as the relief topography in the Miramich River Basin Watershed constrains the meander migration extent and potential fluvial erosion area. In contrast, the flat topographic setting and ample discharge volume of great and medium rivers (e.g. Lower St. John River, Oromocto River) in the Lower St. John River Watershed result in greater areas of meander migration extent and potential erosion hazard.

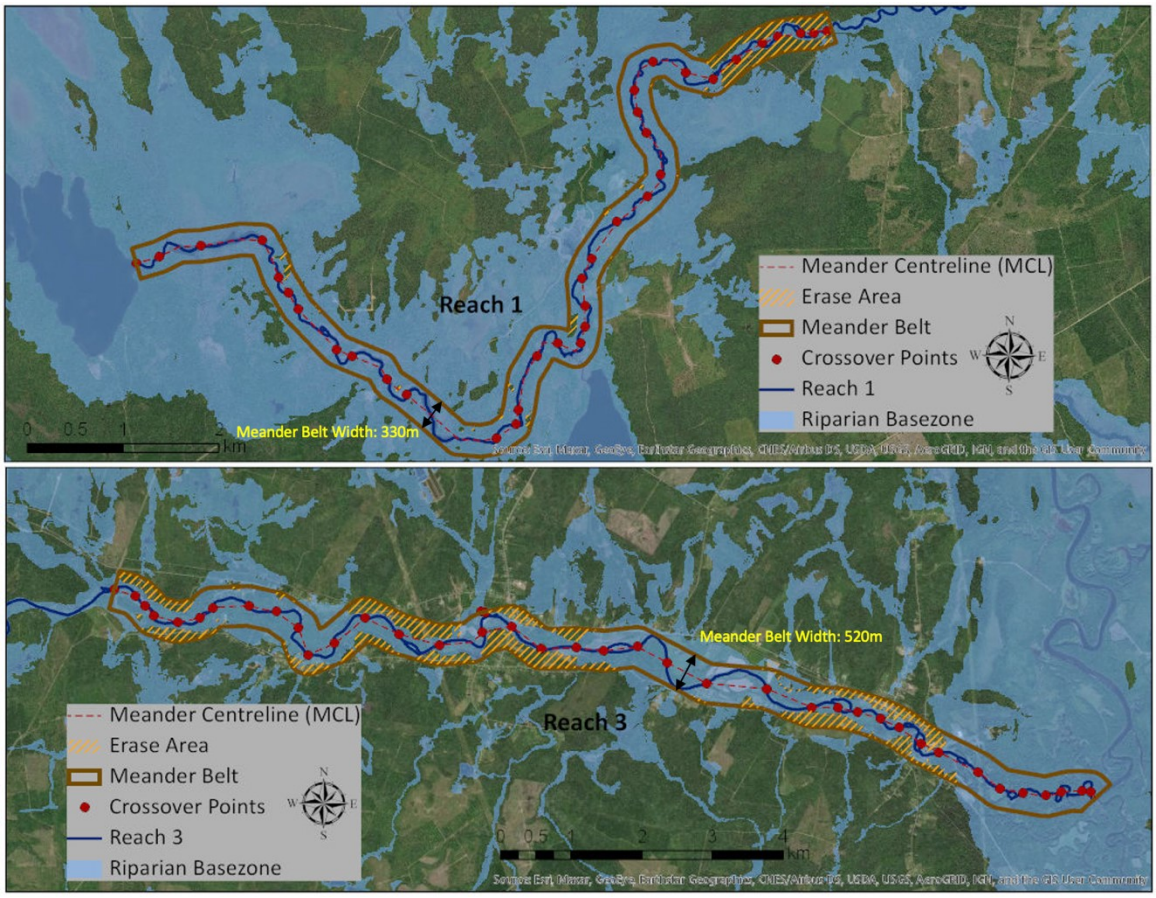

Figure 3-12 Meander belt delineation of the North Branch Oromocto River (reach 1 and reach 3). The MCL (red dash line) identified for reach 1 (with irregular meander pattern) follows the primary meander pattern which gradually shifts downstream. Areas within preliminary meander extent but outside riparian basezone extent (orange slash line) are eliminated from the final meander extent.

3.4 Discussion

The active river meander belt delineation method developed in this study was informed by approaches applied in Vermont, US (Kline and Dolan, 2008) and Southern Ontario, CA (Parish Geomorphic, 2004). The introduced reach separation concept (Parish Geomorphic, 2004) is critical to accurate meander belt delineation, allowing practitioners to better understand the variation in meander pattern and width along the watercourse. For instance, it is always expected that the meander belt of a watercourse increases in width in the downstream direction since it is essentially a function of flow discharge (Parish Geomorphic, 2004). Given this reasonable assumption, the meander belt width of reach 2 of the North Branch Oromocto River should be greater than that of reach 1. However, because reach 2 is located in a confined valley, its meander migration extent is deeply constrained by the steep valley wall adjacent to the watercourse. Such a confined setting makes the meander migration extent highly consistent with the extent of the valley bottom, and in this case, smaller than that of the reach 1. Other local modifying influences such as riverbank material erodibility and stream gradient can also explain why the meander belt varies in width among different reaches in the downstream direction. It should be noted that meander reach configuration is also subject to temporal variation in physical parameters, such as changes in water flow and human infrastructural development. When these reach separation parameters remain relatively unaltered through time, the current meander reach configuration is expected to remain constant through time (Parish Geomorphic, 2004). However, if any of the physical parameters are expected to change naturally and/or by human alteration in the future, then it can

reasonably be expected that the reach extent will be altered, thereby affecting the future meander reach configuration.

Although the developed meander belt delineation framework takes the spatial variables along the watercourse into consideration by separating rivers into different distinct meander reaches geographically, there remain various assumptions and limitations. First, the method is based on the assumption that the existing meander configuration represents a dynamic equilibrium condition between meander pattern and the driving forces of meander form, and that it will remain constant into the future, such that the future meander pattern can be estimated from the current meander pattern (Kline and Dolan, 2008). This hypothesis is unlikely to hold true under changing climate and land-use scenarios which may impact erosion rates and/or flood frequency and ultimately the future meander pattern and meander migration extent (Parish Geomorphic, 2004). To enable a precise future prediction of meander migration extent for a given watercourse, thereby minimizing future erosion risk to private property and structures, more detailed investigations into the historical change in controlling and modifying variables of meander pattern (e.g. hydrological regime and stream gradient setting and etc.) need to be completed. With such information, more accurate predictive models of future controlling variables and meander pattern may be developed. This type of work, however, is beyond the scope of this study and should be undertaken by qualified geomorphologists with relevant technical support that can be provided by an interdisciplinary team.

Secondly, although a general conceptual framework was introduced to identify the location of crossover points and MCLs (see section 3.2.6), there are limited practical sources to inform the optimal choice of scale at which to add crossover points and

simplify the channel with irregular or compound meander pattern, which makes MCL identification a subjective task. The identification of crossover points will vary among different practitioners and depend on the care taken to complete the work. In the future, a machine learning-based algorithm should be developed to automatically or semi-automatically identify the river inflection points.

Finally, it should be noted that this study did not make any effort to delineate the meander migration extent for high gradient river reaches situated in confined valleys. This does not mean that the location of river reaches with certain features will remain static over time. As rivers have limited ability to meander beyond the toe of valley wall (Kline and Dolan, 2008), it is reasonable to expect that the meander migration extent of river reaches situated in confined valleys are highly consistent with the extent of riparian basezone in which they are situated, and thus the local riparian basezone extent is essentially their meander migration extent. Based on the same theory (i.e. rivers have limited ability to meander beyond the toe of valley wall), the final meander migration extent of reaches situated in partially confined valleys were also delimited by the extent of riparian basezone. However, since some of the valley walls are formed by highly erodible materials and may be prone to fluvial erosion, they may allow the development of channel sinuosity and meander migration (Parish Geomorphic, 2004). Additionally, given most valley walls are sloped and not nearly vertical, they may be important to slope adjustment, runoff pattern change and sediment discharges for rivers (Kline and Dolan, 2008). Thus, completely constraining the meander belt to the valley bottom may underestimate the actual meander migration extent, which is an undesirable scenario for both riparian conservation planning and fluvial erosion hazard management, with

detrimental implications (Parish Geomorphic, 2004). Given these factors, it may be important to adjust meander boundaries along valley walls for river reaches situated in confined or partially confined valleys in accordance with geotechnical slope stability considerations (Parish Geomorphic, 2004).

3.5 Conclusion

In this chapter, a novel approach based on fluvial geomorphology concepts was developed to define the meander belt extent within active river areas. The developed methodology analyzed the relationship between meander formation controlling variables (i.e. riverbank materials, valley confinement and stream gradient) and meander pattern and migration extent; measured spatial controlling variables along the drainage network in a GIS; and spatially separated rivers into different meander reaches based on the measured spatial variables. It also introduced a way to quantify the meander migration extent at the reach scale based on the definition of meander belt under the ARA framework. The applicability of the developed meander belt delineation method was tested and evaluated on different size rivers (i.e. great, medium and small rivers) across the two watersheds with different topographic relief settings. The application provides valuable insights on how to implement the method, demonstrates that it can be effectively applied in a variety of geomorphological contexts, and thereby enhances the likelihood that it will be of utility in other settings and contexts.

The meander delineation result of the example river reveals that the relationship between river bankfull width and meander belt width is consistent with the finding in a previous study in the field (Williams, 1986). Additionally, it demonstrates that the

meander belt width along the watercourse is not completely a function of flow discharge rate but also subject to the local physical setting, which emphasizes the importance of reach separation in the meander belt delineation framework.

This method, however, is not without its own limitations. Estimation of meander positions in active river areas, or indeed an estimation of channel dimensions at some point in the future, is restricted by limited knowledge regarding future climate changes which could conceivably cause changes to flow discharge significant enough to cause a morphological channel response. Other future changes in the controlling and modifying influences of meander pattern such as flow regime change cannot be foreseen and therefore may only be estimated at best (Parish Geomorphic, 2004). Additionally, the subjective decisions made on crossover point locations and MCLs identification may influence the overall accuracy of meander belt delineation. Automatic or semi-automatic methods for river inflection point identification should be developed and applied in future studies with the aid of machine learning techniques to make the meander delineation results more scientifically reliable. Finally, completely constraining the river meander belt to the extent of the riparian basezone may underpredict the actual meander migration extent, which is an undesirable scenario for conservation planning and risk-hazard prevention purposes (Parish Geomorphic, 2004). Future methodological refinements in terms of meander boundary adjustments for river reaches situated in confined or partially confined river valley is recommended.

Chapter 4. Accuracy and Efficiency Assessment of Different DEM Data on ARA Delineation

4.1 Introduction

Two main characteristics of a DEM, namely, vertical accuracy and spatial resolution, are directly related to its ability in terms of topographic representation and flow simulation, which are two key components in flood modelling and active river area delineation (Smith et al., 2008; Fereshtehpour and Karamouz, 2018). Several researchers have investigated the effects of DEM spatial resolution and vertical errors on topographic characteristics representation (Zhang and Montgomery, 1994; Holmes et al., 2000; Vaze et al., 2010). Thomas et al. (2007) found that the aggregation (i.e. upscale) of DEM resolutions will seriously deteriorate accuracy of terrain parameters. Lower DEM spatial resolutions tend to produce narrower slope distributions and lower mean slope value, attributed to the smoothing of topography and loss of topographic details (Thompson et al., 2001). Additionally, the reliability of DEM-derived flood extent is significantly affected by DEM errors and uncertainties (Fereshtehpour and Karamouz, 2018), given the impacts of DEM vertical errors on the accuracy of topographic indices (e.g. slope, aspect, etc.). A suite of studies have examined DEM errors using statistical approaches that frequently employ root-mean-square-error (RMSE) to quantify the global vertical error of a DEM and found a negative relationship between the RMSE and the accuracy of topographic indices and flood inundation modelling (Wechsler, 2007; Carlisle, 2005; Saksena and Merwade, 2015). For instance, Saksena and Merwade (2015) resampled

high-spatial resolution LiDAR DEMs to lower spatial resolution and found a relationship between errors arising from DEM properties to fluvial flood inundation maps.

Since topography defines the pathways of surface water movement across a watershed (Wu et al., 2008; Thomas et al., 2017), the spatial resolution of elevation data can also be crucial to the accuracy of flow simulation modelling (Thomas et al., 2017). A major disadvantage of low-resolution DEM data is the loss of important local-scale features (e.g. roads, bridges and culverts, etc.), potentially creating inevitable errors in flow direction modelling (Haile and Rientjes, 2005; Nussey and Noseworthy, 2020). Fortunately, high-spatial resolution LiDAR DEM has been widely reported to successfully address flow simulation issues. For instance, Poppenga et al. (2009) compared LiDAR derived surface flow features in Minnehaha County, U.S., with 30-m and 10-m National Elevation Datasets (NED) that were previously applied in similar studies; the authors found that surface flow features generated from 1-m LiDAR-derived DEMs are consistently integrated with elevation and are important in understanding surface water movement, specifically in that these higher spatial resolution elevation models can better detect surface-water runoff, flood inundation, and erosion in comparison to the original 30-m and 10-m NED DEM.

Raw (i.e. unsmoothed) high-resolution LiDAR DEMs, however, may also be inappropriate for topographic representation and hydrological process modelling (Kuo et al., 1999). Topographic surfaces are highly complex at local spatial scales (< 10 m), owing to the prevalence of un-autocorrelated topographic variation (Lindsay et al., 2019), contributing to the rough appearance of many high-resolution DEMs (MacMillan et al., 2003) and ultimately confounding the measurement of topographic indices (e.g. slope,

aspect, etc.) and the modelling of near-surface flow processes (Habtezion et al., 2016; Lindsay et al., 2019). As introduced previously (see Chapter 2), the excessive surface roughness of high-spatial resolution LiDAR DEMs results in the production of inaccurate slope grids and cost distance surface modelling, generating unreasonably wide creek and headwater basezones at local spatial scales and makes the final ARA extents unacceptably inaccurate. Furthermore, a very high-spatial resolution DEM could result in the representation of a terrain surface that is much more detailed than necessary for the process being modelled (Ziadat, 2007), imposing challenges with respect to increased data storage, and computational intensity required for processing and manipulation (Sangster, 2002).

The previous studies reveal that the characteristics of DEMs (i.e. horizontal resolution and vertical accuracy) play important roles in topographic and hydrological modelling, thus the accuracy of flood inundation mapping and active river area delineation relies heavily on the properties (quality) of the input DEM data (Smith et al., 2008; Saksena and Merwade, 2015). High-spatial resolution LiDAR DEM, however, has its own limitation (i.e. over-detailed topography representation) and is not necessarily better than low-spatial resolution DEM in terms of topographic representation and hydrological modelling (Wechsler, 2007). Studies on selecting optimal spatial resolutions of elevation data that can satisfy both data processing and storage capabilities and representation of spatial variability, for different models are therefore necessary (Thomas et al., 2017; Smith et al., 2008). To date, efforts have been made to identify optimal input DEMs for several flood inundation and riparian area delineation models (e.g. TOPMODEL, the SWAT model and Bathtub method, etc.) (Zhang and Montgomery,

1994; Lin et al., 2010; Fereshtehpour and Karamouz, 2018). Unfortunately, no ARA-related studies to date have carried out accuracy-efficiency analyses to identify the optimal DEM for ARA delineation, limiting the efficiency of the ARA framework and confidence in the modelled outputs for application in riparian conservation and management contexts (Smith et al., 2008; Nussey and Noseworthy, 2020). Moreover, in this study, the advantages of high-spatial resolution LiDAR DEMs in terms of ARA delineation have been hindered by excessive surface roughness. To allow the ARA framework to take advantage of high-resolution LiDAR DEMs, an appropriate DEM smoothing algorithm must be applied to subdue the surface roughness before commencing topographic and hydrological modelling. Thus, the main objectives of this chapter are to (i) identify an appropriate DEM smoothing algorithm to lessen the rough appearance of high-spatial resolution LiDAR DEMs; (ii) compare the differences between smoothed DEMs-derived ARA and unsmoothed DEMs-derived ARA (iii) conduct an error analysis for DEMs of varying resolutions and different sources with the aid of commonly used error statistics and analyze topographic and hydrological indices uncertainties introduced by DEM sources, resampling and smoothing; and, (iv) provide an accuracy-efficiency tradeoff analysis framework to help select the optimal DEM for future ARA studies.

4.2 Materials and Methods

A high-spatial resolution LiDAR DEM smoothing algorithm is introduced, followed by a methodology for analyzing the effect of DEM quality on topographic and

hydrological indices. A developed accuracy-efficiency tradeoff analysis framework for optimal DEM selection is then described.

4.2.1 Feature-Preserving DEM Smoothing Algorithm (FPDEMS)

Surface roughness is a natural component of the bare Earth's topography, and therefore its presence in high-spatial resolution LiDAR DEMs is expected (Lindsay et al., 2019). Local scale surface roughness, however, is often undesirable in computer-based modelling since it adds complexity (noise) to a DEM, which inevitably affects the characterization of macro-scale topography (Lindsay et al., 2019). DEM smoothing algorithms, commonly low-pass filters (i.e. mean, median and Gaussian filters), are frequently applied to LiDAR DEMs to lessen the surface roughness (Walker and Willgoose, 1999; Gallant, 2011). These techniques, however, have a tendency to blur edges of important topographic features and small drainage features (i.e. ditches, gullies, etc.) (Barash, 2002; Lindsay et al., 2019). Several flood modelling and riparian area delineation applications take advantage of high-resolution LiDAR DEMs to represent these local-scale drainage features, which provides the justification for the application of high-spatial resolution DEMs in projects (Petrasova et al., 2017). Thus, it is counter-productive to smooth high-spatial resolution elevation data if the outcome is the removal of important topographic information (Lindsay et al., 2019).

The smoothing algorithm applied to LiDAR-DEM in this study is the "Feature-Preserving DEM Smoothing" algorithm (FPDEMS) developed by Lindsay et al. (2019). This algorithm was specifically designed to smooth raster DEMs while preserving the important topographic features (Lindsay et al., 2019). The algorithm has three general steps: (i) calculate the normal vector field from the DEM surface, (ii) smooth the normal

vector field, and (iii) use the smoothed normal vector field to update the original vertex positions (Lindsay et al., 2019). These three steps can be automatically carried out by the "FeaturePreservingSmoothing" tool, which has already been implemented in an open-source geospatial analysis platform called WhiteboxTools (Lindsay, 2019). The user specifies three main tool parameters: the smoothing filter kernel size, the threshold normal difference angle (in degrees), and the number of elevation-update iterations.

To lessen the rough appearance of high-resolution LiDAR DEMs (i.e. 3-m and 5-m), the "FeaturePreservingSmoothing" tool was applied to high-resolution LiDAR DEMs of the Lower St. John River Watershed and Miramichi River Basin Watershed. The three parameters were determined as 11*11 kernel, 15° threshold, and three iterations for 5-m LiDAR DEM data and more aggressively for 3-m LiDAR DEM data (i.e. 17*17 kernel, 25° threshold, and five iterations). These parameters were determined by reviewing a previous study carried out by Lindsay et al. (2019) as a compromise between processing time and processing performance.

4.2.2 Effects of DEM Quality on Slope Grids and the TMI

The qualities of different DEMs were reported by calculating DEM error statistics. Three types of DEM errors are considered in this study including those arising from resampling (i.e. upscaling) of a LiDAR DEM from a higher to lower spatial resolution, data sources and LiDAR DEM smoothing. These errors can be estimated by computing RMSE and Mean Error (ME) for each of the elevation datasets with respect to the reference dataset in order to report global elevation error statistics for the entire DEM (Fereshtehpour and Karamouz, 2018; Fisher and Tate, 2006). The RMSE measures the global accuracies of the DEM surface, which indicates how concentrated the predicted

data is around the "line of best fit" (Equation 4-1) (Fisher and Tate, 2006). The ME is a measure of bias, which quantifies the systematic error indicating the degree to which the elevation dataset is, on average, underestimated or overestimated compared to the reference dataset (Equation 4-2) (Fereshtehpour and Karamouz, 2018).

$$\mathrm{RMSE} = \sqrt{\frac{\sum(\mathrm{Zp}-\mathrm{Zt})^2}{\mathrm{n}}}$$

Equation 4-1

$$\mathrm{ME} = \frac{\sum(\mathrm{Zp}-\mathrm{Zt})}{\mathrm{n}}$$

Equation 4-2

Where "Zt" refers to the elevation value for the "i^{th}" point obtained from the reference dataset, "Zp" is the elevation value for the "i^{th}" point obtained from the lower quality DEMs, and "n" is the total number of points for which elevation values are retrieved.

As 1-m LiDAR DEM data is available in the study watersheds, the reference dataset in this study was considered as the elevations obtained from the 1-m LiDAR DEM. To calculate the error statistics, a number of points (i.e. 1000) were randomly generated across each of the two study watersheds (Fig. 4-1) as the ground control points (GCPs). These GCPs are evenly distributed over the entire study watershed to cover all different types of landscape. After creating GCPs, the elevation values of the reference dataset and lower quality DEMs were extracted to GCPs to calculate the elevation errors (i.e. $\mathrm{Zp} - \mathrm{Zt}$). The two error statistics were then reported for different lower quality DEMs based on the formulas mentioned above.

Slope and TMI derived from different lower quality DEMs (see Chapter 2 for detail) were then selected and applied to analyze the effect of DEM qualities (i.e. RMSE)

on topographic and hydrological modelling and ARA delineation as they are two major indices for riparian basezone and riparian wetland delineation, respectively.

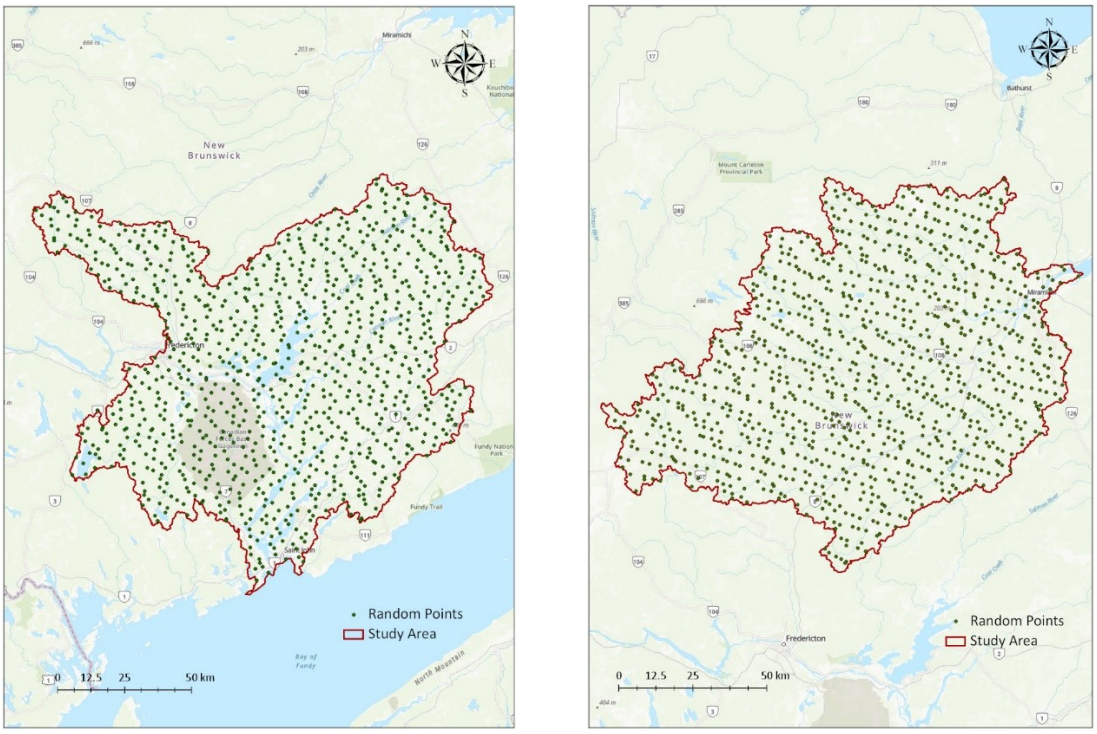

a. Lower St. John River Watershed *b. Miramichi River Basin Watershed*

Figure 4-1 The location of random points (green) in (a) Lower St. John River Watershed and (b) Miramichi River Basin Watershed

4.2.3 Computer-Based Accuracy-Efficiency Tradeoff Analysis

The most suitable DEM for ARA analysis is determined by analyzing the performance of different DEMs on ARA delineation in terms of final output accuracy and time and effort spent on data processing. The tradeoff analysis is conducted by separately measuring accuracy and efficiency components of different parallel analyses. The approach for ARA output accuracy measurement is inspired by remote sensing-based accuracy assessment techniques (Janssen and Vanderwel, 1994; Campbell, 1996), involving the derivation of accuracy metrics (i.e. user's accuracy, producer's accuracy, and Kappa Coefficients) based on the comparison of delineated ARA components and

reference ARA components for a set of specific locations (Foody, 2002). Briefly, the user's accuracy (errors of commission) represents the proportion of pixels that are incorrectly delineated as a known ARA component when they should have been classified as something different according to the reference ARA. In contrast, producer's accuracy (error of omission) is calculated as a proportion of pixels of a known ARA component that classified as something other than the known component (ESRI, 2018). The Kappa Coefficient then considers a measure of overall accuracy of ARA delineation and individual ARA component accuracy as a means of actual agreement between delineation and observation (i.e. reference ARA) (Ismail and Jusoff, 2008). The value of Kappa lies between "0" and "1", where "0" represents agreement due to chance only, while "1" represents complete agreement between two sets of ARA results. Overall, the goal of this approach is to quantitatively determine how effectively pixels were grouped into the correct ARA components in the study watersheds (Foody, 2002; Ismail and Jusoff, 2008).

Given the absence of field verification data and high-resolution aerial imagery for the study watersheds and the inaccuracy of 3-m DEM derived ARA extent caused by excessive surface roughness, the reference dataset was determined as the 3-m smoothed DEM-derived ARA. To get the reference DEM and other DEM-derived ARA components at specific locations for confusion matrix creation, the 1000 random points generated for the error statistics calculation in the previous section (Fig. 4-1) were applied to extract the underlying ARA components from the reference DEM and other DEM-derived ARAs, respectively. Confusion matrices were then generated for accuracy assessment with the aid of the "compute confusion matrix" command in ArcGIS Pro™

(ESRI, 2018). Classification accuracy (i.e. user's accuracy and producer's accuracy) and Kappa Coefficients were automatically calculated for the accuracy assessment of different DEM-derived ARA extents.

As for efficiency assessment, the important characteristic is the computational effort expressed as the time spent to run key geoprocessing tools. Runtimes of different geoprocessing tools applied for ARA delineation have been automatically stored in the GIS software environment, among which "cost distance" and "flow accumulation" command are the two most time-consuming tools. These tools are also key for riparian basezone delineation and riparian wetland delineation, respectively. Furthermore, the runtime of these two geoprocessing tools are considerably increased as data volumes become larger (i.e. DEM resolutions become higher). Thus, runtimes of these two tools were considered as efficiency components and applied to compare against the results of ARA accuracy assessment to find the optimal DEM for future ARA delineation.

4.3 Results

The results of high-spatial resolution DEM smoothing, and smoothed DEM derived ARA extent are presented, followed by the relationship between DEM quality and the value distribution of topographic and hydrological indices. Results of the ARA accuracy and data processing efficiency assessment are then provided.

4.3.1 High-Spatial Resolution LiDAR DEMs Smoothing

Visual inspection on the original high-spatial resolution LiDAR DEMs derived-Hillshade and smoothed LiDAR DEMs-derived Hillshade reveals that the edge-preserving nature of the FPDEMS method is able to effectively subdue topographic

complexity at local spatial scales in both 3-m and 5-m LiDAR DEMs, while not significantly impacting the complexity of macro-scale landforms (Fig. 4-2) based on the selected parameters (i.e. filter kernel size, threshold normal difference angle (in degrees) and the number of elevation-update iterations). As shown in Fig. 4-2 c and 4-2 d, the rough appearance of raw high-resolution LiDAR DEMs was successfully removed, while the boundaries of important topographic features (i.e. channel edges) were effectively preserved. Beyond preserving the important topographic features, the FPDEMS method is well suited to maintaining the geometry of small streams. Fig. 4-2 shows the effects of the FPDEMS method in an area containing incised creeks; the steepness of channel banks on both sides of the creek was preserved well by the FPDEMS method.

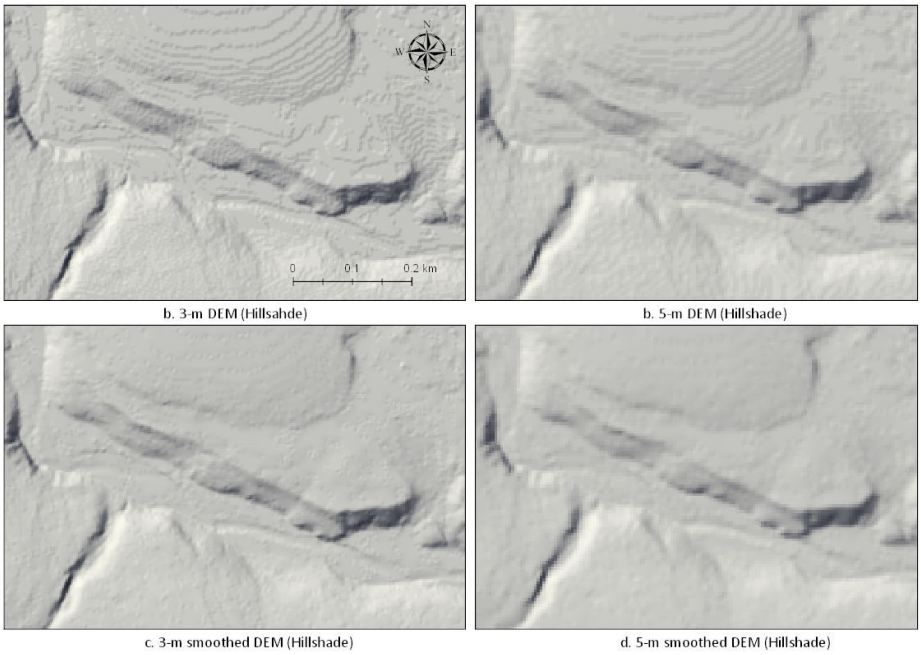

Figure 4-2 A comparison of original high-resolution (3- and 5-m) LiDAR DEMs derived shade relief images (a and b) and FPDEMS smoothed LiDAR DEMs derived shaded relief images (c and d). Images present portions of the Hillshade surface extracted from each DEM in the Miramichi River Basin Watershed.

4.3.2 Smoothed High-Spatial Resolution LiDAR DEMs-derived ARA Extent

Smoothed LiDAR DEMs can generate more reasonable creeks and headwaters basezone extents in comparison to the raw high-spatial resolution LiDAR DEMs (Fig. 4-

3). As shown in the shaded relief images (Fig. 4-2), raw high-spatial resolution LiDAR DEMs exhibit lots of cut-off planforms or so-called "*padi terraces"* at the local spatial scale where creeks and headwaters always exist. These areas are typical of closed contours where all the surrounding pixels exhibit the same elevation and/or slope value. Accordingly, all the pixels inside the closed contours were assigned the same cost distance value and thus the determined cost distance thresholds cannot necessarily cut-off the accurate basezone extent for creeks and headwaters, which results in extremely wide basezone areas. The FPDEMS method successfully removed these cut-off planforms from the DEM surface (Fig. 4-2); pixels can therefore receive accurate cost distance values given their location to source cells (i.e. creeks and headwaters grids). As a result of this, the determined cost distance thresholds can effectively cut off areas that are no longer likely to be dynamically linked to creeks and/or headwaters, and thus the creek and headwater basezones derived from smoothed LiDAR DEMs are more accurate (Fig. 4-3).

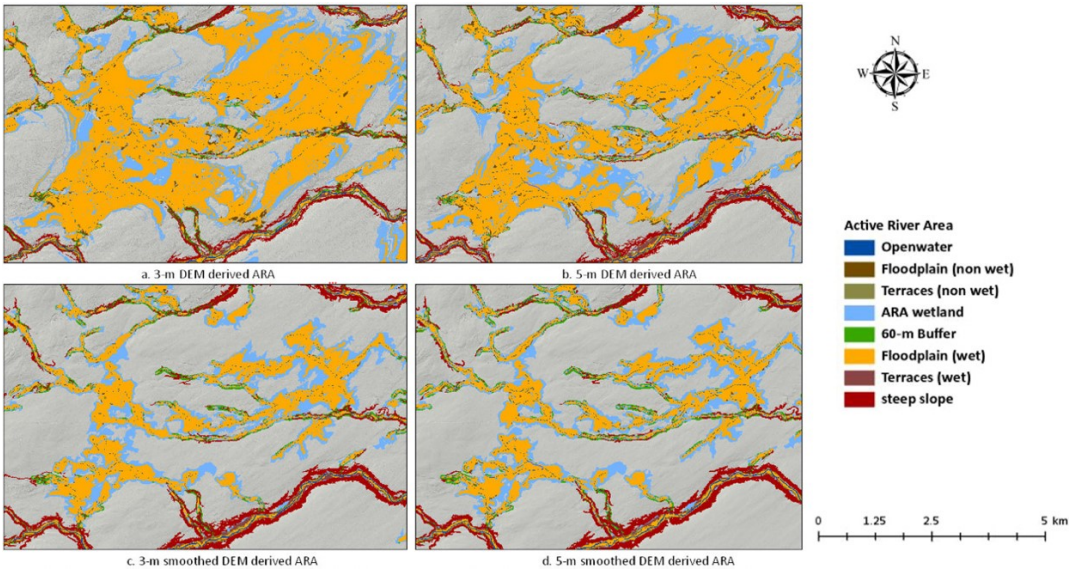

Figure 4-3 A comparison of raw high-resolution (3- and 5-m) DEMs-derived ARA (a and b) and FPDEMS smoothed DEMs-derived ARA (c and d). Image presents portion of creeks and headwater areas in the Miramichi River Basin Watershed.

The total area of floodplain derived from smoothed elevation data is considerably smaller than that derived from raw LiDAR DEMs as the over-prediction issue of creek and headwater basezones has been successfully addressed by FPDEMS treatment. For instance, in the Lower St. John River Watershed, the total floodplain areas (wet and non-wet) derived from 5-m LiDAR DEM and 5-m smoothed LiDAR DEM are approximately 3130.16 km^2 and 1552.98 km^2, respectively, a difference of 1577.18 km^2 (> 50%) (Table 4-1). The same trend can also be found in the Miramichi River Basin Watershed. For instance, the total area of floodplain derived from raw 3-m DEM is 3238.17 km^2, while the area of floodplain derived from 3-m smoothed DEM is 1340.6 km^2, decreased by almost 60% (Table 4-1). The area of riparian wetlands also show a decreasing trend in both study watersheds. For example, in the Miramichi River Basin Watershed, the area of riparian wetland decreases by 25% due to 5-m LiDAR DEM smoothing (from 1200.37 km^2 to 889.88 km^2) (Table 4-1). This result is not surprising, since the FPDEMS smoothing algorithm removed many cut-off planforms. These planforms are typically areas of low slope (almost 0 degrees) and are highly likely to be misidentified as riparian wetlands. Furthermore, the increasing trend in the area of steep slope can be found in both watersheds (Table 4-1), which can also be explained by removal of the cut-off planforms.

Table 4-1 A comparison of original DEM-derived ARA area (in sq km) and FPDEMS smoothed DEM derived ARA area (in sq km) for (a) the Lower St. John River Watershed and (b) the Miramichi River Basin Watershed

a. Lower St. John River Watershed

DEM resolution	Openwater	Floodplain		Terraces		Wetland	MCZs (steep slope area)	MCZs (60-m)
		(Wet)	(Non-Wet)	(Wet)	(Non-Wet)			
5-m	782.06	2625.84	504.32	244.47	157.91	1181.33	906.85	418.82
3-m	744.16	3246.26	544.78	447.93	206.88	1370.5	1003.65	407.39
smoothed 5-m	782.06	1314.33	238.65	227.21	170.74	826.17	992.02	529.36
smoothed 3-m	744.16	1415.77	281.91	215.94	132.01	1008.62	1034.96	531.4

b. Miramichi River Basin Watershed

DEM resolution	Openwater	Floodplain		Terraces		Wetland	MCZs (steep slope area)	MCZs (60-m)
		(Wet)	(Non-Wet)	(Wet)	(Non-Wet)			
5-m	228.9	2452.88	94.84	220.31	52.36	1200.37	778.82	178.12
3-m	203.2	3075.09	163.08	258.08	57.07	1337.34	883.67	196.03
smoothed 5-m	228.9	1235.28	39.37	166.84	46.3	889.88	851.3	218.86
smoothed 3-m	203.2	1289.5	51.1	205.73	46.58	967.37	886.08	214.18

4.3.3 Effect of DEM Errors on Slope and TMI Value Distribution

For all resampled and smoothed LiDAR DEMs in the two study watersheds, MEs were in the sub-centimeter level, indicating that biases introduced by DEM resampling and smoothing were negligible (Table 4-2). In contrast, MEs calculated for SRTM DEMs were considerably greater than those for resampled and smoothed LiDAR DEMs, with the number of 2.80 m and 2.08m for the Lower St. John River Watershed and the Miramichi River Basin Watershed, respectively, meaning SRTM DEMs, on average, overestimated the elevation values compared to the reference dataset (i.e. 1-m LiDAR DEM). This over-estimation refers to the fact that the elevation of SRTM DEM represents a Digital Surface Model (DSM), not a bare Earth model, as the top of dense canopy forests and built-up areas are included in the SRTM DEM (Nelson et al., 2009). The presence of such features can be quite problematic, especially in hydrological modelling (Nelson et al., 2009). Furthermore, the RMSEs for SRTM 30-m DEMs are significantly higher than resampled 30-m LiDAR DEMs by approximately 4 times in both study watersheds, indicating overall low accuracy of SRTM DEMs as compared to LiDAR DEMs of the same resolution. For the resampled LiDAR DEMs, the RMSE is increased by decreasing the resolution of DEMs; the same trend was found in both study watersheds. For instance, in the Lower St. John River Watershed, the RMSE ranges from 0.2588 m to 1.0281 m, increasing for all resampled LiDAR DEMs as the resolution decreased from 3-m to 30-m (Table 4-2). It is also interesting to note that RMSEs of smoothed high-resolution DEMs and raw high-resolution DEMs are different only marginally (Table 4-2). For instance, the RMSEs calculated for 3-m smoothed and 3-m raw LiDAR DEMs are 0.3067 and 0.2588, respectively, in the Lower St. John River

Watershed, indicating the ideal ability of the FPDEMS method in terms of preserving original elevation values.

Table 4-2 Global statistics summarizing vertical errors (m) for different quality DEM datasets

	Lower St. John River Watershed		Miramichi River Basin Watershed	
	ME	RMSE	ME	RMSE
SRTM-30m	2.80	4.1855	2.080	3.8066
30-m	0.055	1.0281	0.018	0.8854
15-m	0.024	0.6132	0.014	0.6148
10-m	0.026	0.4626	0.012	0.4539
5-m	0.004	0.3376	-0.01	0.3550
3-m	0.005	0.2588	0.015	0.2702
5-m smooth	0.002	0.4443	-0.006	0.4509
3-m smooth	0.011	0.3067	0.003	0.3018

As for the effect of DEM quality on topographic (i.e. slope) modelling, similar relationship between slope value distribution and DEM quality (RMSE) was detected in the two study watersheds. The maximum slope value increases dramatically as the resolution of the resampled LiDAR DEMs increases (or RMSE value decreases) in the two study watersheds (Table 4-3). For example, the maximum slope value increases from approximately 60 degree to 80 degree as the LiDAR DEM resolution increases from 30-m (RMSE = 1.0281) to 3-m (RMSE= 0.2588) in the Lower St. John River Watershed (Table 4-3). The maximum value of slope raster derived from 30-m SRTM DEM is less than that derived from 30-m LiDAR DEM in both study areas, reflecting the same relationship between these two DEMs in terms of RMSE (Table 4-2 and Table 4-3). In addition to the maximum slope value, the mean slope value increases as the RMSE value of resampled LiDAR DEMs decreases (Table 4-3). For instance, in the Miramichi River Basin Watershed, mean slope value increases from 2 degree to 8 degree (approximately) as the RMSE values of LiDAR DEMs drop from 0.8854 (30-m) to 0.2702 (3-m). Besides,

as the smoothed high-resolution LiDAR DEMs and raw high-resolution LiDAR DEMs have similar RMSE values, the value range of slopes derived from FPDEMS smoothed LiDAR DEMs is similar to that derived from the raw high-resolution LiDAR DEMs in the two study watersheds (Table 4-3), reflecting an ideal characteristic of the FPDEMS method in terms of important topographic feature preservation. The inner value distribution of slope grids, however, are different between the smoothed high-resolution LiDAR DEMs and raw high-spatial resolution LiDAR DEMs (Table 4-3). For instance, in both study watersheds the interquartile range (i.e. first quartile to third quartile) of the smoothed high-spatial resolution LiDAR DEM derived slopes is smaller than that of raw high-spatial resolution LiDAR DEM derived slopes, as the FPDEMS method removed several planforms (i.e. "*padi terraces"*) with low-slope values.

Table 4-3 Box plots show the value distribution of slope grids for different DEMs in (a) Lower St. John River Watershed and (b) Miramichi River Basin Watershed

a. Lower St. John River Watershed

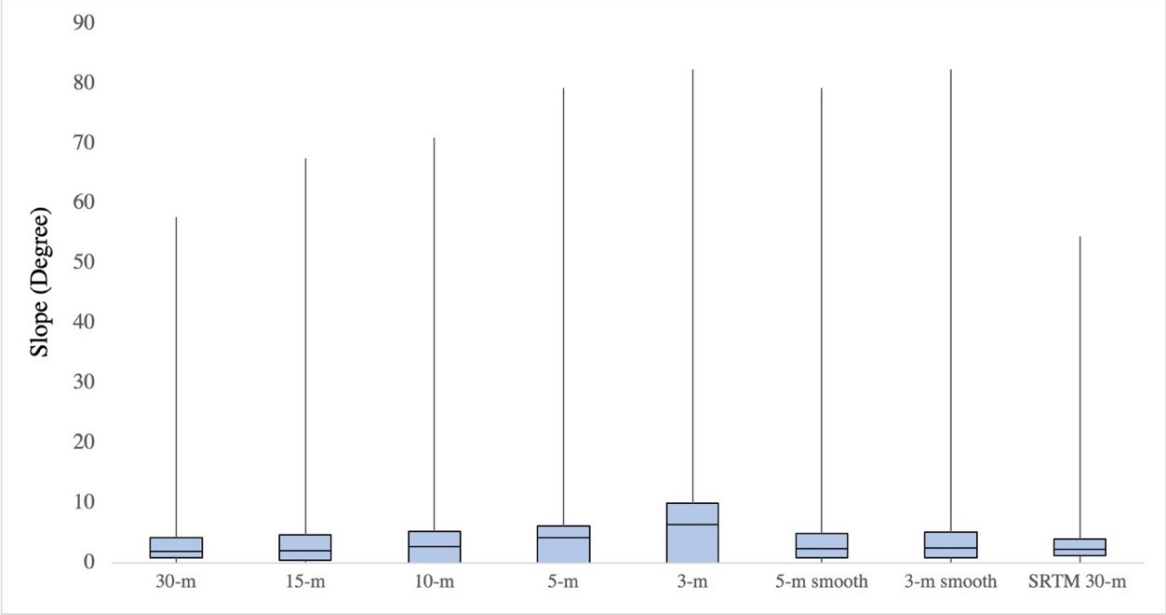

b. Miramichi River Basin Watershed

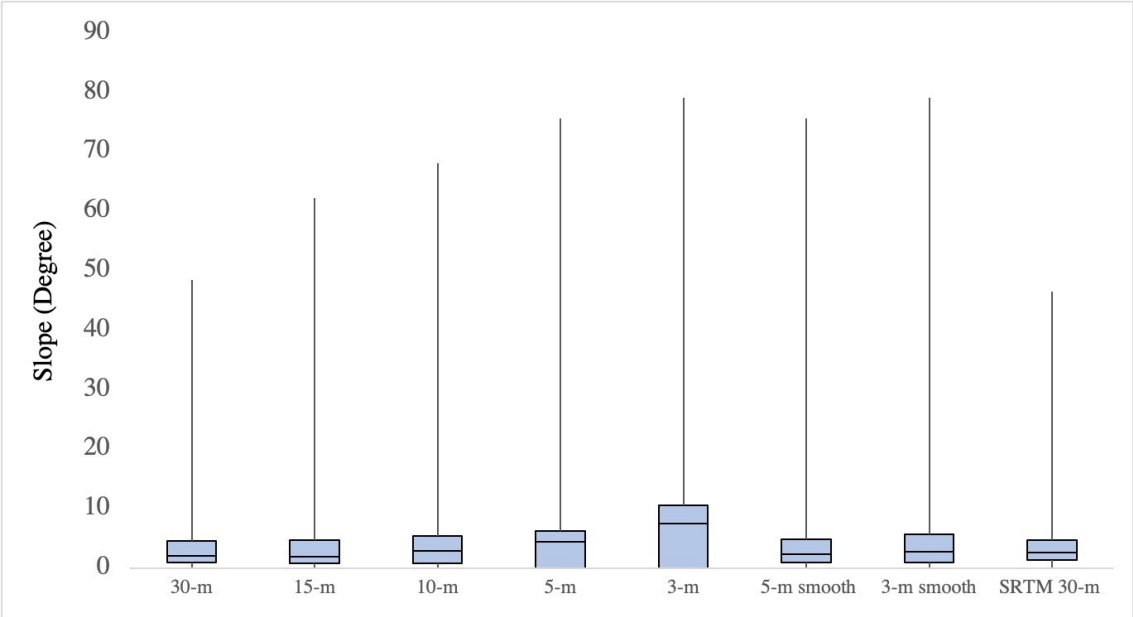

The comparison of different DEM-derived TMIs shows that the TMI value distributions vary among different parallel analyses (Table 4-4). Generally, the TMI values derived from DEMs with low RMSE values (i.e. high-resolution resampled and/or smoothed LiDAR DEMs) tend to follow a normal distribution; in contrast, the TMI values derived from DEMs with high RMSE values are positively skewed (i.e. most TMI values are clustered around the left tail of the distribution while the right tail of the distribution is longer). For instance, in the Miramichi River Basin Watershed, the differences between medium (744) and mean (747) values of 5-m LiDAR DEM (RMSE = 0.3550) derived TMI is 3, such differences increased to 160.32 and 217.89, respectively, for the TMIs derived from 30-m LiDAR DEM (RMSE = 0.8854) and 30-m SRTM DEM (RMSE = 3.8066) (Table 4-4). Besides, a declining tread can be seen in both mean and median values of TMI as the RMSE value of DEM increases; a similar trend can be found in both study watersheds (Table 4-4). This declining trend means more pixels were receiving lower TMI values in the low quality (i.e. high RMSE value)

DEM-based parallel analyses, possibly explaining in part the underprediction issue of riparian wetland area introduced in Chapter 2. Additionally, the DEM smoothing algorithm (i.e. FPDEMS method) lowered the mean and median values of TMI in both study watersheds, though it is difficult to comment on the accuracy of one distribution over another in the absence of reference data. For instance, in the Lower St. John River Watershed, the mean and medium values of raw 3-m DEM derived TMI are 1037.87 and 1006, respectively. FPDEMS treatment made these two values decline to 767.53 and 734, respectively (Table 4-4). Such effects of FPDEMS treatment partially explain the declining trend in the area of riparian wetland shown in the Table 4-1, as more pixels were receiving lower TMI values and were considered as dry areas.

Table 4-4 Distribution of TMI derived from different DEMs

	Lower St. John River Watershed			Miramichi River Basin Watershed		
	Mean	**Median**	**Std. Dev**	**Mean**	**Median**	**Std. Dev**
SRTM 30-m	109.87	-127	1132.13	87.89	-130	1066.91
30-m	396.9	140	1335.21	294.32	132	1120.74
15-m	491.51	309	1213.4	432.74	341	945.1
10-m	504.27	426	971.19	514.63	455	912.5
5-m	762.74	721	990.53	747	744	908.28
3-m	1037.87	1006	1001.8	991.37	1005	900.09
5-m smooth	585.06	567	867.53	413.19	410	654.09
3-m smooth	767.53	734	891.33	447.06	440	629.36

4.3.4 Accuracy-Efficiency Trade-Off Analysis

The selection of suitable DEM for ARA delineation is discussed in terms of ARA accuracy and data processing efficiency. The results of accuracy assessment for different DEM-derived ARA extents, including for user's accuracy, producer's accuracy, and Kappa Coefficients are presented in Appendix D. Generally, the overall accuracy (i.e.

Kappa Coefficient) of ARA delineation is subject to the DEM quality (i.e. RMSE); the correlation coefficients (R^2) between Kappa Coefficient and RMSE are approximately 0.6 and 0.75, respectively, in the Lower St. John River and Miramichi River Basin Watershed, indicating a relative strong relationship (Fig. 4-4). For instance, in the Miramichi River Basin Watershed, the Kappa Coefficients increase from 0.5903 to 0.6789 as the LiDAR DEM RMSE values decrease from 0.8854 (30-m) to 0.4539 (10-m). The correlation between the RMSEs of raw high-resolution LiDAR DEMs (i.e. 3-m and 5-m resolutions) and Kappa Coefficients of raw high-resolution LiDAR-DEM derived ARAs, however, does not fit this trend line (Fig. 4-4), as the creek and headwater basezone extents are grossly inaccurate due to surface roughness. For example, although the RMSE of 3-m LiDAR DEM is 0.2588 in the Lower St. John River Watershed, the Kappa Coefficient calculated for the 3-m LiDAR DEM derived ARA is 0.5252, which is even lower than 30-m LiDAR DEM derived ARA (Table 4-5) (Fig. 4-4). Raw 3-m and 5-m LiDAR DEM based parallel analyses were therefore excluded from the regression analysis to reduce bias. As this accuracy assessment framework applied 3-m smoothed DEM derived ARA as a reference dataset, the Kappa Coefficient of 3-m smoothed DEM derived ARA is 1 in both watersheds (Table 4-5). In addition to the reference ARA, the 5-m smoothed LiDAR DEM-derived ARAs achieved highest overall accuracy in the final ARA output, with Kappa Coefficients at 0.7884 and 0.8247, respectively, in the Lower St. John River Watershed and Miramichi River Basin Watershed (Table 4-5). Besides, since the SRTM-DEM has the highest RMSE value, the Kappa Coefficients of 30-m SRTM-DEM derived ARA are smaller than that of 30-m LiDAR DEM derived ARA in both study watersheds. More specifically, the Kappa Coefficients of 30-m LiDAR DEM

and 30-m SRTM DEM derived ARA are similar in the Lower St. John River Watershed. The difference between Kappa Coefficients of 30-m LiDAR DEM and 30-m SRTM DEM derived ARA, however, is considerable in the Miramichi River Basin Watershed. Accordingly, it is reasonable to suspect that 30-m SRTM DEM and 30-m LiDAR DEM have the similar ability to delineate the ARA in the watershed with flat topography setting (i.e. Lower St. John River Watershed). Further, as the NCC-ARA project were conducted based on a coarse national hydrological network (i.e. 1:50,000 NHN), many creeks and headwaters at the local spatial scale were eliminated, and thus the overall accuracies of NCC-ARA extent are the lowest among all ARA results, with Kappa Coefficients at 0.3530 and 0.3400, respectively, in the Lower St. John River and Miramichi River Basin watersheds (Table 4-5) (Fig. 4-4).

Table 4-5 Kappa Coefficients of different DEMs-derived ARA extent

	Kappa Coefficient	
	Lower St. John River Watershed	Miramichi River Basin Watershed
SRTM 30-m (1:50,000 NHN)	0.3530	0.3400
SRTM 30-m (1:10,000 NBHN)	0.5187	0.4564
30-m	0.5952	0.5903
15-m	0.6251	0.6611
10-m	0.6647	0.6789
5-m	0.6387	0.6092
3-m	0.5252	0.4822
5-m smooth	0.7884	0.8247
3-m smooth	1.0000	1.0000

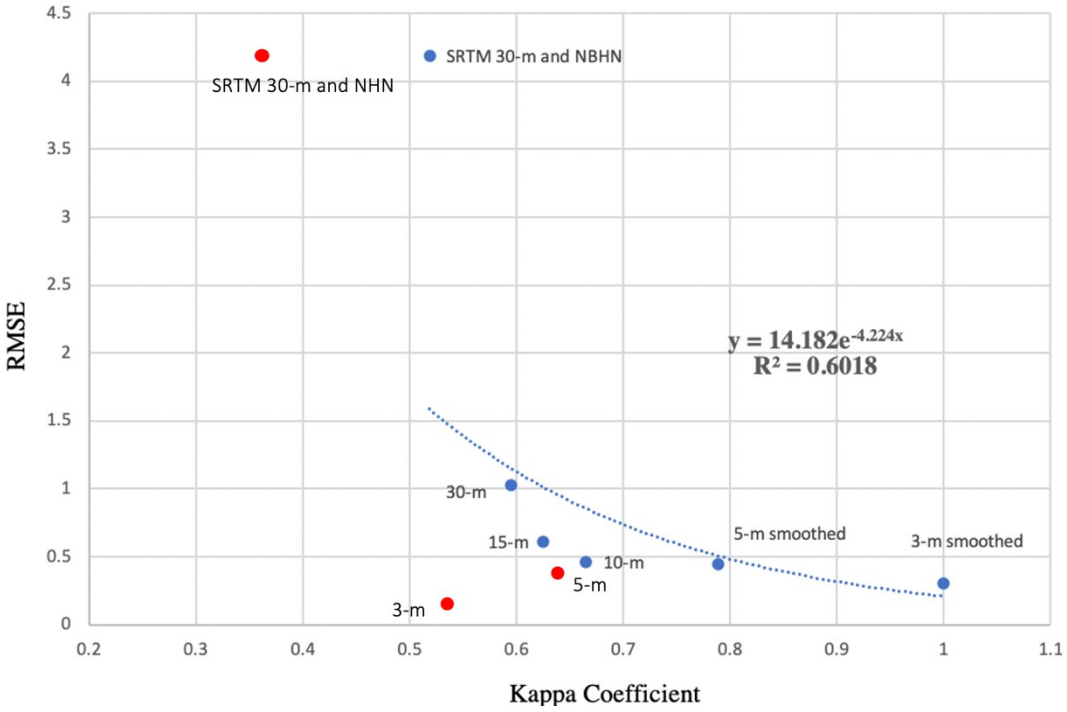

a. Lower St. John River Watershed

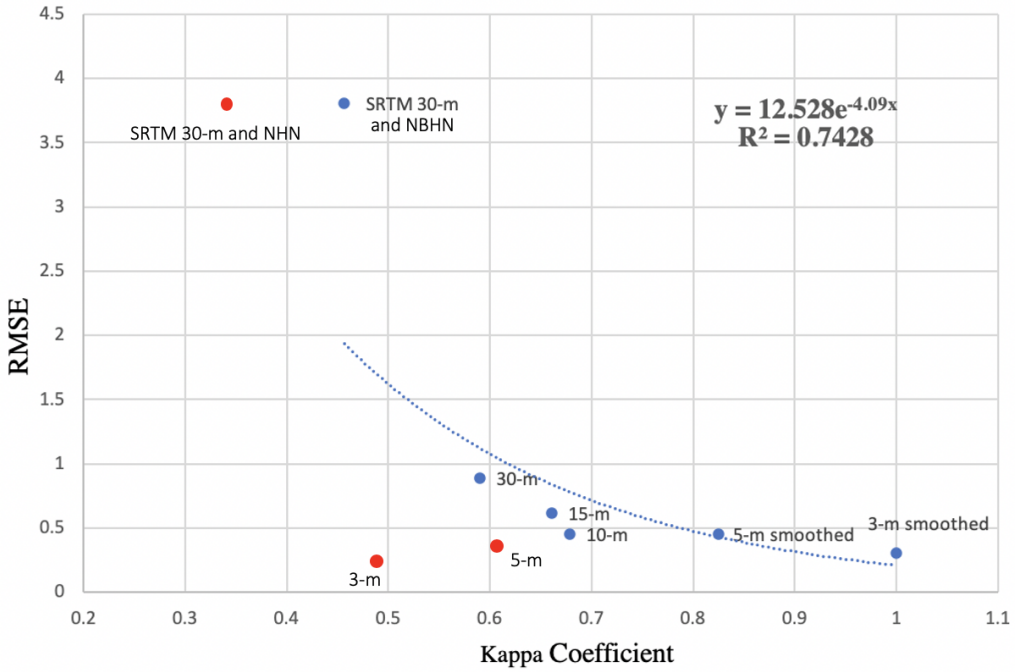

b. Miramichi River Basin Watershed

Figure 4-4 The relationship between DEM RMSE and ARA Kappa Coefficient in the (a) Lower St. John River Watershed and (b) Miramichi River Basin Watershed. Raw 3-m and 5-m DEM derived ARAs and NCC-ARAs based on 1:50,000 NHN (red dots) were excluded from the correlation equation and R^2 calculation to reduce bias

The variation in runtimes of key geoprocessing tools with respect to different DEMs-based ARA analyses is shown in Table 4-6. As shown, the total runtime (i.e. batch cost distance + flow accumulation) for 30-m LiDAR DEM and 30-m SRTM DEM-based analyses are the same in the two study watersheds since the amount of time spent on running geoprocessing tools is highly dependent on the number of computational cells (Fereshtehpour and Karamouz, 2018), which are the same in 30-m LiDAR and 30-m SRTM DEMs. Additionally, there is moderate difference in runtimes among different low-spatial resolution LiDAR DEM-based analyses. For instance, the total runtime increases by approximately 7 times (from 5 minutes to 37 minutes) as the LiDAR DEM resolution increases from 30-m to 10-m in the Lower St. John River Watershed. In contrast, a significant increase in runtime can be detected in both watersheds once the LiDAR DEM spatial resolution reaches 5-m. For example, the total runtime increases to 190 minutes (increase by 38 times) and 601 minutes (increase by120 times), respectively, as the LiDAR DEM spatial resolution increases from 30-m to 5-m and 3-m in the Lower St. John River Watershed (Table 4-6). Accordingly, the 5-m LiDAR DEM can be assumed as a turning point in runtime in both study watersheds. The overall accuracy (Kappa Coefficient) of 5-m LiDAR DEM derived ARA, however, is relatively low due to the inaccurate delineation of creeks and headwaters basezone, and thus raw 5-m LiDAR DEM is not an ideal elevation dataset for ARA delineation. It is interesting to note that the DEM smoothing algorithm can save almost 30% in data processing time by smoothing noisy microtopographic details such as tree mounds. For instance, in the Miramichi River Basin Watershed the total runtime of the two geoprocessing tools in the

3-m LiDAR DEM based analysis is 591 minutes, but decreases to 414 minutes in the 3-m smoothed LiDAR DEM based analysis (Table 4-6).

Table 4-6 Runtime (minutes) of the two geoprocessing tools in different DEMs based parallel analyses

	Lower St. John River Watershed		Miramichi River Basin Watershed	
	Batch Cost Distance	Flow Accumulation	Batch Cost Distance	Flow Accumulation
SRTM 30-m	3 mins	2 mins	4 mins	2 mins
30-m	3 mins	2 mins	4 mins	2 mins
15-m	9 mins	6 mins	12 mins	7 mins
10-m	25 mins	12 mins	25 mins	13 mins
5-m	152 mins	38 mins	141 mins	32 mins
3-m	521 mins	80 mins	516 mins	75 mins
5-m smooth	89 mins	46 mins	73 mins	99 mins
3-m smooth	277 mins	103 mins	261 mins	153 mins

To carry out the accuracy-efficiency trade-off analysis and determine the optimal DEM for ARA delineation with respect to accuracy and efficiency, the accuracy-efficiency curve was created using runtime and Kappa Coefficient as variables (Fig. 4-5). Given that raw 3-m and 5-m LiDAR DEM derived ARAs contain considerable errors in creek and headwater basezones, their Kappa Coefficient can not necessarily reflect the ability of high-resolution LiDAR DEM in terms of ARA delineation and thus they were excluded from the trade-off analysis to reduce bias. Similarly, as the NCC-ARA project were conducted based on coarse national hydrological network (i.e. 1:50,000 NHN) which eliminates lots of creeks and headwaters at the local scale, NCC provided ARAs were also excluded from the trade-off analysis. A strong correlation relationship was detected between the accuracy (Kappa Coefficient) and efficiency (runtime) variables, with the coefficient of 0.91 and 0.92 in the Lower St. John River Watershed and Miramichi River Basin Watershed, respectively (Fig. 4-5). This scenario indicates that

although more time is required to process DEMs with lower RMSE values, they can generally produce more accurate ARA results. It is clear that the inflection point of the accuracy-efficiency curve exists at the 5-m smoothed LiDAR DEM in both study watersheds (Fig. 4-5), which means that 5-m smoothed LiDAR DEMs can achieve relatively high accuracy in ARA results, while allowing data processing within a reasonable time frame. Although 3-m smoothed LiDAR DEMs can achieve more accurate ARA results than 5-m smoothed LiDAR DEMs, the time required to process 3-m smoothed LiDAR DEMs is significantly longer than for 5-m smoothed LiDAR DEMs. Therefore, based on the results of accuracy-efficiency trade-off analyses, 5-m smoothed LiDAR DEMs are recommended to be used in future ARA analyses, especially those applied across multiple watersheds or large study sites.

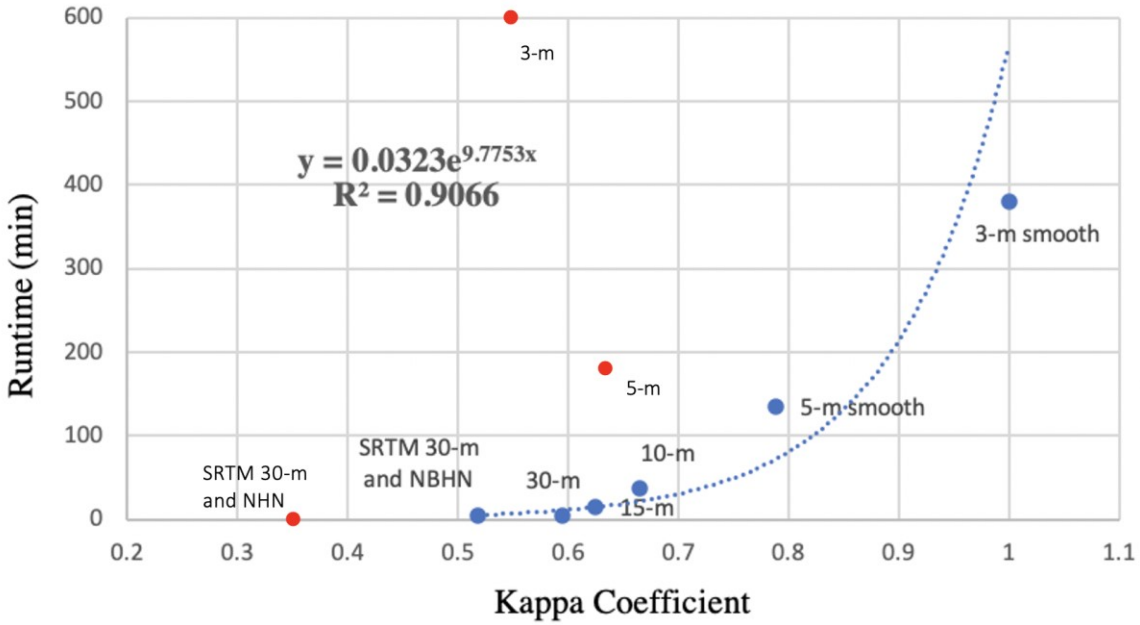

a. Lower St. John River Watershed

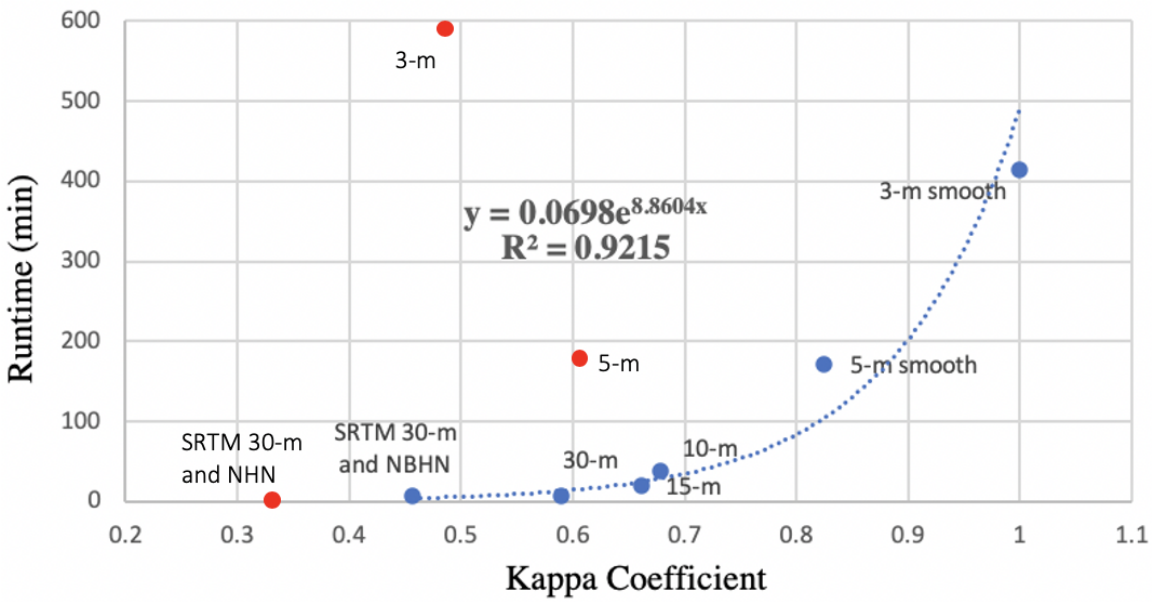

b. Miramichi River Basin Watershed

Figure 4-5 The relationship between total runtime (i.e. batch cost distance + flow accumulation) and Kappa Coefficient of different DEMs based parallel analyses in the (a) Lower St. John River Watershed and (b) Miramichi River Basin Watershed. Raw 3-m and 5-m DEMs based ARA analyses and NCC's ARA analysis (red dots) were excluded from the correlation equation and R^2 calculation

4.4 Discussion

As shown by the results, topographic and hydrological indices and ARA extent derived from DEMs with low RMSE values are generally higher in accuracy than those derived from DEMs with high RMSE values; meanwhile, more time and effort are required to process high-quality DEM data, which makes ARA delineation less efficient. A DEM that balances ARA accuracy and data processing efficiency is needed to achieve effective ARA delineation.

The SRTM DEM and resampled LiDAR DEMs in low resolutions with high RMSE values caused errors and/or uncertainties in topographic and hydrological modelling and ultimately resulted in less accurate ARA extents. LiDAR DEMs at 3-m and/or 5-m resolution with low RMSE values, however, were also found to be unsuitable for ARA analysis due to the effects of surface roughness on creek and headwater

basezone delineation. Fortunately, a DEM smoothing algorithm—FPDEMS method (Lindsay et al., 2019)—was found and tested. The test results show that the FPDEMS method can effectively remove local-scale surface roughness caused by over-detailed microtopographic representation, while preserving important topographic and hydrological features. Moreover, the time spent running the FPDEMS method is acceptable, at approximately 5 minutes and 25 minutes for 5-m LiDAR DEM and 3-m LiDAR DEM, respectively, in both study watersheds, with the aid of a high-end laptop (6-core 2.2 GHz processor and 24 GB of memory). As indicated by Cohen. (1960), Kappa Coefficient greater than "0.8" represents a perfect agreement between delineation and observation (i.e. 3-m smoothed DEM-derived ARA). The 5-m smoothed LiDAR DEMs (with the Kappa Coefficients at approximately 0.8) therefore achieving highly accurate results in terms of ARA delineation in both study watersheds. The times to process 3-m and 5-m smoothed LiDAR DEMs, however, differ greatly (by almost 3 times) in both study watersheds, which means 3-m smoothed LiDAR DEM is less efficient on ARA delineation compared to 5-m smoothed LiDAR DEM. Therefore, to balance accuracy and efficiency, a 5-m smoothed LiDAR DEM is recommended for the future ARA delineation, especially in studies at large spatial extents or across multiple watersheds. It should be noted that 5-m smoothed LiDAR DEM based ARA analyses require more disk storage space (i.e. with 43 GB for the Lower St. John River Watershed and 42.9 GB for the Miramichi River Basin Watershed) as compared to the commonly used SRTM DEM based ARA analyses (i.e. with 0.96 GB for the Lower St. John River Watershed and 1.04 GB for the Miramichi River Basin Watershed). Effective data

storage system therefore should be built before delineating the ARA based on 5-m smoothed LiDAR DEM.

The recommendation on applying 5-m smoothed LiDAR DEM for future ARA studies, however, should be applied carefully since the accuracy-efficiency tradeoff analysis is based on multiple assumptions and has its own limitations. First, the number of ARA parallel analyses (i.e. 6) conducted in this study is relatively small. To get more representative correlation coefficients between runtime and final ARA accuracy (i.e. Kappa Coefficient) and make more robust recommendation on the optimal DEM selection, more ARA parallel analyses based on various DEM spatial resolutions should be accomplished by future studies under the support of more advanced computation power. Moreover, the accuracy-efficiency curves were modelled after Fereshtehpour and Karamouz (2018) who analyzed the relationship between runtime and DEM spatial resolution for efficiency coastal flood vulnerability assessment. Similar to their work, outliers (i.e. raw 3-m and 5-m LiDAR DEM derived ARA and NCC provided ARA) were discarded in order to reduce bias in the regression analysis. It should be note that, however, the removed outliers represent a considerable proportion of the sample (i.e. different ARA parallel analyses), magnifying the small sample size issue. Second, the reliability of the reference ARA (i.e. 3-m smoothed LiDAR DEM derived ARA) needs to be discussed. Although it has been well acknowledged in the literature that high-resolution LiDAR DEMs with low RMSE values can achieve higher accuracy in results in terms of floodplain delineation (Vaze et al., 2010; Saksena and Merwade, 2015; Thomas et al., 2017), there is no reference literature to demonstrate that ARA related studies also fit this trend. It should be noted that the result of tradeoff analyses may differ

if the reference ARA changes. Nevertheless, the proposed computer-based accuracy assessment framework provides a unique lens through which to effectively assess ARA accuracy. In future studies, ground reference surveys are recommended to verify and enhance the reliability of the reference ARA by visually identifying ARA components at specific locations in the field. Additionally, ground reference surveys can enhance the accuracy of RMSE values calculated for different DEMs by replacing the reference elevation values extracted from 1-m LiDAR DEM with the true elevation values measured in the field.

The RMSE was applied as a major index to indicate DEM quality in this study, which allows the reader to know the effect of DEM quality on the accuracy of topographic and hydrological indices and final ARA extent. RMSE is an index to indicate the global accuracy of a DEM, which assumes error to be aspatial (Hunter and Goodchild, 1997). Error related to the DEM, however, varies spatially (Hawker et al., 2018) and cannot be sufficiently assessed by a global metric such as RMSE (Carlisle, 2005). Indeed, scientists have observed that local DEM error can be large and spatially correlated, though global RMSE is small (Holmes et al., 2000; Bater and Coops, 2009), and thus it is possible that the optimal DEM resolution for ARA delineation is landscape specific (Thomas et al., 2017). A more comprehensive way to consider DEM error from a spatial perspective (or landscape perspective), such as Classification and Regression Tree (CART) analysis (Bater and Coops, 2009) and Monte Carlo-based Sequential Gaussian Simulation (SGS) analysis (Fereshtehpour and Karamouz, 2018), is therefore required. Such analyses can allow the DEM user to better understand the relationship between DEM quality and the accuracy of ARA. Optimal DEM for ARA delineation may also

vary within a watershed given differences in landscape features (e.g. slope, land cover, etc.), and thus, ideally, or eventually, it is anticipated that optimal DEM will be identified for specific landscape contexts in future applications (Holmes et al., 2000; Hawker et al., 2018).

4.5 Conclusion

This chapter discussed the consequences of surface roughness inherent to high-spatial resolution LiDAR DEMs, introduced an effective DEM smoothing algorithm called FPDEMS method (Lindsay et al., 2019) and tested its performance on smoothing high-spatial resolution LiDAR DEMs. It also reported global accuracies for DEMs used in different parallel analyses by calculating ME and RMSE values and analyzed the effect of DEM quality on topographic and hydrological modelling. Finally, it introduced an accuracy-efficiency tradeoff analysis framework to help select the optimal DEM for future ARA studies.

The results show that the FPDEMS method can effectively smooth the high-spatial resolution LiDAR DEM surface roughness caused by over-detailed topographic representation at local spatial scales, while preserving topographic and hydrological features important to accurate ARA delineation. Additionally, DEM quality (RMSE) was found to heavily control the value distribution of topographic and hydrological indices: DEMs with low RMSE values tend to result in wider slope value ranges and normally distributed TMI values; in contrast, DEMs with high RMSE values tend to produce narrower slope value ranges and positively skewed TMI values. The results of the accuracy-efficiency tradeoff analysis reveal that 5-m smoothed LiDAR DEM is best able

to balance ARA output accuracy and data processing efficiency, and thus 5-m smoothed LiDAR DEM is identified as the optimal elevation dataset for future ARA delineation. This finding is particularly important in ARA studies that cover large spatial extents and/or multiple watersheds, where accuracy remains important but changes in effort would be multiplied.

This finding, however, is based on several assumptions and should be interpreted with caution and updated by future studies. To make the result of tradeoff analysis more robust, more ARA parallel analyses based on more dataset combinations are expected to be accomplished with the aid of more advanced computation power in the future. Additionally, ground reference surveys are recommended to be conducted to enhance the reliability of the reference ARA. With ground truthing, reference ARA components at specific locations would be visually identified in the field rather than extracted from the 3-m smoothed LiDAR DEM derived ARA. Additionally, DEM error (quality) should be assessed under the spatial (i.e. landscape) perspective with the aid of more advanced techniques, such as CART analysis (Bater and Coops, 2009) and/or SGS analysis (Fereshtehpour and Karamouz, 2018), in order to let the DEM user better understand the effect of input DEM quality on ARA delineation. Landscape specific optimal DEMs for ARA delineation are expected to be found and recommended by future studies.

Chapter 5. Conclusion and Discussion

5.1 Revisiting Research Goals and Objectives

The primary objectives of this research were to address limitations identified in contemporary spatial ARA methodology and determine the optimal DEM spatial resolution for future ARA studies across broad (eco-) regions. One limitation of the current ARA framework is that the floodplain and terrace separation methodology has not been fully developed because the commonly applied 30-m and 10-m SRTM elevation data does not allow the user to explicitly identify subtle topographic transitions between floodplains and terraces (Marangelo and Farrell, 2010). To address this limitation, this study developed and tested an ARA-based floodplain and terrace separation framework for two watersheds with different topographic relief settings in New Brunswick with the aid of high-spatial resolution (i.e. 3-m and 5-m) resampled LiDAR DEMs. Second, a robust ARA-based meander belt delineation framework remains elusive as there is no existing standard or ARA-specific assessment tool allowing the user to delineate meander belt extent (Marangelo and Farrell, 2010), making the ARA framework unsuitable for informing fluvial erosion management practices (Rapp and Abbe, 2003; Smith et al., 2008). To address this weakness, this study developed an ARA-based meander belt delineation framework that considers the differences in physical characteristics between reaches along the watercourse. Third, in order to determine the effect of DEM source and spatial resolution on the area and spatial extent of the ARA, this study delineated ARA extent based on multi-resolution resampled LiDAR DEMs and SRTM DEM and compared the results with each other and to those derived from 30-m SRTM DEM and 1:50,000 NHN as delineated by NCC. Fourth, to allow the ARA framework to take

advantage of high-spatial resolution LiDAR DEMs and reduce noise-induced biases in the optimal DEM determination step, this study found and tested a smoothing algorithm developed by Lindsay et al. (2019) to apply to the elevation data. Fifth and finally, to explicitly determine the optimal DEM spatial resolution for future ARA studies across large regions and multiple watersheds, this study comparatively analyzed various DEMs for ARA output accuracy and the time and effort spent on data processing. To do so, the effects of DEM quality on the accuracy of topographic and hydrological indices and final ARA extent were identified, and an accuracy-efficiency tradeoff analysis framework was developed.

5.2 Key Findings

The key findings about the performance of high-spatial resolution LiDAR DEMs in terms of floodplains and terraces separation, and ARA delineation are presented, followed by the performance of the smoothing algorithm in preserving important topographic and hydrological features. The effects of DEM quality on the accuracy of topographic and hydrological indices and final ARA extent are then illustrated. Finally, the finding related to optimal DEM source and spatial resolution for future ARA studies is discussed.

Finding 1: The resampled high-spatial resolution LiDAR DEMs (i.e. 3-m and 5-m) can allow the user to separate terraces from modern floodplains for great, medium and small rivers based on the developed separation methodology.

High-resolution LiDAR DEM data can provide enough detail about the elevational and horizontal distance changes in river valleys, which allows users to

analyze the valley morphology of rivers (i.e. great, medium and small rivers) and visually differentiate terraces from modern floodplains for the rivers in those size classes. High-spatial resolution LiDAR DEM data, however, failed at extracting valley morphology information for small streams (i.e. creeks and headwaters) due to the appearance of excessive surface roughness ("*padi terraces*") at local spatial scales caused by over-detailed topographic representation, which introduced errors in identifying floodplain-terrace transition lines in slope and planform.

Finding 2: The area and spatial extent of different ARA components are largely affected by the source and spatial resolution of DEMs, and/or the spatial resolution of input hydrological networks.

High-spatial resolution DEM data can accurately summarize the area of openwater across the study watersheds, as the first step in the ARA delineation process. The extent of riparian wetland derived from high-spatial resolution LiDAR DEMs match better with the extent of provincial wetland and the hydric soil inventory, allowing for accurate identification of overlapping areas between riparian basezones and riparian wetlands, which are typically areas of conservation priority. Additionally, this study found that high-spatial resolution LiDAR DEMs can more precisely but not more accurately delineate the riparian basezones for great, medium and small rivers as compared to low spatial resolution LiDAR and SRTM DEMs; high-spatial resolution LiDAR DEM can also create more detailed slope grids and pick up flood-free areas, and incorporate more steep-slope MCZs into the final ARA output. Further, the low-spatial resolution, national-scale hydrological network eliminates many creeks and headwaters that are apparent at local spatial scales, thereby excluding these small streams from the

ARA delineation, which makes the area of NCC-derived ARA (based on 1:50,000 NHN) generally smaller than the area of the ARA derived from the 1:10,000 NBHN.

Finding 3: Raw high-spatial resolution LiDAR DEMs (i.e. 3-m and 5-m) are not suitable for ARA delineation.

Topographic surfaces are highly complex at local spatial scales (Lindsay et al., 2019); with the ability to represent local scale topographic variation, raw high-spatial resolution LiDAR DEMs always have a rough appearance, which inevitably affects the characterization of macro-scale topography (Lindsay et al., 2019). The rough appearance consists of multiple cut-off planforms, or so-called "*padi terraces,"* on the DEM surface. *"Padi terraces"* are typical in areas of closed contours, where all the surrounding pixels have the same elevation and/or slope value. Accordingly, all the pixels inside the closed contours are assigned similar cost distance values, and thus the determined cost-distance thresholds necessarily cannot cut-off an accurate basezone extent for creeks and headwaters, which results in extremely wide creek and headwater basezones and grossly inaccurate ARA extents.

Finding 4: FPDEMS method can effectively smooth the high-spatial resolution DEM surface roughness at local spatial scales and generate more accurate ARA extents within an acceptable time frame.

The edge preserving nature of the FPDEMS method is able to effectively subdue topographic complexity at local spatial scales in both 3-m and 5-m LiDAR DEMs, while not significantly impacting the complexity of macro-scale landforms. As the FPDEMS method successfully removes cut-off planforms (i.e. *padi terraces*) from the high-spatial resolution LiDAR DEM surface, pixels can therefore receive accurate cost distance

values given their relative location to source cells (i.e. creeks and headwaters grids). As a result, the determined cost distance thresholds can detect spatially explicit creek and headwater basezones. The time required to run the FPDEMS method is acceptable, at approximately 5 minutes and 25 minutes for 5-m LiDAR DEM and 3-m LiDAR DEM, respectively, in both study watersheds.

Finding 5: The value distributions of topographic and hydrological indices, and final ARA accuracy are heavily controlled by the input DEM quality (RMSE).

The comparison of value distributions of slope grids and TMI derived from different sources and spatial resolutions of DEMs shows that high-quality DEMs (with low RMSE values) tend to result in wider slope value ranges and normally distributed TMI values; in contrast, low-quality DEMs (with high RMSE values) tend to produce narrower slope value ranges and positively skewed TMI values. Besides, relative strong negative relationships are found between DEM quality (RMSE) and final ARA accuracy (Kappa Coefficient) (i.e. the higher the RMSE value of the input DEM, the lower the Kappa Coefficient of the final ARA) in both study watersheds, indicating the importance of input DEM quality in ARA delineation.

Finding 6: FPDEMS smoothed-LiDAR DEM in 5-m resolution best balances ARA output accuracy and data processing efficiency.

Inflection points of the accuracy-efficiency curves exist at 5-m smoothed LiDAR DEMs in both study watersheds, indicating that 5-m smoothed LiDAR DEMs can achieve relatively high accuracy in ARA results, while allowing data processing within a reasonable time frame. Although 3-m smoothed LiDAR DEMs can achieve more accurate ARA results than 5-m smoothed LiDAR DEMs, the time required to process 3-

m smoothed LiDAR DEMs is almost 3 times longer than that for 5-m smoothed LiDAR DEMs. Therefore, to balance accuracy and efficiency, a 5-m smoothed LiDAR DEM is recommended for future ARA delineations in studies at large spatial extents or across multiple watersheds.

5.3 Limitations and Implications for Future Studies

This research has addressed major limitations in the current ARA framework by developing floodplain and terrace separation and meander belt delineation frameworks and made a clear recommendation for future ARA studies in terms of optimal DEM selection. Nonetheless, there remain limitations and challenges to be addressed by future studies.

Firstly, the satellite-derived flood extent applied for cost-distance threshold calibration shows the extents of known historical flood events as well as areas that have a probability of flooding as determined from historical records (GeoNB , 2011), while terraces under the ARA framework refer to land areas that are likely to be inundated during vary large flood events (e.g. 1:100 year floods). There is no reference source, however, to demonstrate that the applied satellite-derived flood extent completely covers the entire 1:100-year flood extent. As a result, the riparian basezone extent (i.e. floodplain and terrace) calibrated by the existing satellite-derived flood extent may underestimate true basezone and terrace extents. In future studies, more up-to date 1:100-year flood-extent and/or field verification data should be applied to update the results of riparian basezone delineation and floodplains and terraces separation, as also indicated by Nussey and Noseworthy (2020).

Secondly, the performance of the developed meander belt delineation framework in terms of predicting future meander positions is restricted by limited knowledge regarding future climate changes, which could conceivably cause significant changes to flow discharge to cause a morphological channel response. To enable precise future prediction of meander migration extent for a given watercourse, thereby understanding future erosion risk, more accurate predictive models of future controlling variables and meander patterns should be developed by future studies, as also recommended by Parish Geomorphic (2004). Additionally, completely constraining the river meander belt to the extent of the riparian basezone may underpredict the actual meander migration extent, which is an undesirable scenario for both conservation planning and risk-hazard prevention purposes (Parish Geomorphic, 2004). Future methodological refinements in terms of meander boundary adjustments for river reaches situated in confined or partially confined river valleys comprised of highly erodible materials are expected to occur in accordance with geotechnical slope stability considerations (Parish Geomorphic, 2004).

Finally, the recommendation of optimal DEM selection for future ARA studies should be applied carefully. Given the absence of field verification data and high-resolution aerial imagery for both study watersheds, the reference ARA applied for the ARA accuracy assessment was extracted from the 3-m smoothed LiDAR DEM derived ARA. There are no previous studies, however, to demonstrate that 3-m smoothed LiDAR DEM can achieve the most accurate ARA results. It should be noted that the results of ARA accuracy assessment and accuracy-efficiency tradeoff analysis may differ if the reference ARA changes. In future studies, ground reference surveys are recommended to verify and enhance the reliability of the reference ARA by visually identifying ARA

components at specific locations in the field. Moreover, given limited computing power (i.e. 6-core 2.2 GHz processor and 24 GB of memory), this study failed to test the performance of 1-m LiDAR DEM data on ARA delineation as the laptop memory use continued to increase during operation and the process was terminated after more than five hours once the data volume reach the maximum capacity of the hard drive (i.e. 256 GB). It is expected that the 1-m (smoothed) LiDAR DEM will result in more accurate ARA result than 3-m smoothed LiDAR DEM, though the processing time is also expected to be longer than 3-m smoothed LiDAR DEM. In future studies, with the support of more advanced computation power, it would be valuable to incorporate 1-m LiDAR DEM and 1-m smoothed LiDAR DEM derived ARA into the tradeoff analysis.

5.4 Final Remarks

Riparian areas are important aquatic-terrestrial interfaces. They maintain water quality, provide habitat and migration corridors for species, and transport energy and organic materials (Smith et al., 2008). Therefore, effective conservation of riparian areas is important and should include the maintenance and restoration of physical and ecological processes of the river and its adjacent land area in order to accommodate its important ecological functions (Smith et al., 2008). The initial stage of effective riparian area management, conservation and restoration is to define and delineate the functional riparian area (Ilhart et al., 2000). However, it is not a straitforward task and may require the understanding of site-specific attributes such as landscape composition and the local environmental setting (Naiman & Décamps, 1997). Because of these challenges, riparian area management and conservation projects apply a “fixed-width buffer guideline”.

Unfortunately, fixed-width buffers may ultimately fail in meeting conservation goals as they do not include variations in site-specific attributes, such as river slope, bank topography, and likely under-estimate the full extent of riparian areas (Kuglerová et al., 2014).

The ARA framework was developed because of challenges associated with the status quo of functional riparian area delineation, which provides a lens through which to effectively address long-recognized shortcomings in standard riparian buffer-width guidelines. The ARA framework, to date, has been widely applied by scientists from TNC and NCC for the Northern Appalachian / Acadian Ecoregion in northeastern U.S. and southeastern Canada with the aid of 30-m SRTM DEM and national scale hydrological network (i.e. NHD and NHN) (TNC, 2015; Nussey and Noseworthy, 2020). Although laudable for the ability of ARA framework in terms of providing a visualization of the riparian area as an interconnected system and highlighting where and how key physical and ecological processes occur within riparian areas, its limitations in terms of accuracy and confidence in terraces and meander belt delineation are well acknowledged (Smith et al., 2008; Marangelo and Farrell, 2010; Nussey and Noseworthy, 2020). The limited knowledge in terms of optimal DEM and hydrological network for ARA delineation further restricts the efficiency of the ARA framework and confidence in applying modelled outputs for riparian conservation and management (Smith et al., 2008; Nussey and Noseworthy, 2020). Methodological refinements and studies on selecting optimal input datasets (i.e. DEM and hydrological network) are therefore required to make the model more reliable for guiding riparian conservation planning actions and fluvial hazard risk assessments and mitigation practices across boarder (eco-) regions.

This study directly addressed this need by developing (1) a floodplain and terrace separation framework designed to take advantage of high-spatial resolution LiDAR DEM to identify subtle transitions between floodplains and terraces in slope and planform, and (2) a meander belt delineation framework which takes into consideration the differences in physical characteristics between reaches along the watercourse. Moreover, to determine the optimal input datasets (i.e. DEM and hydrological network) for future ARA studies, this study (i) applied high-spatial resolution 1:10,000 NBHN to conduct the entire ARA delineation; (ii) found and tested a novel DEM smoothing algorithm to allow the ARA framework to take the advantage of high-spatial resolution LiDAR DEM; (iii) analyzed the effect of input DEM quality (RMSE) on the accuracy of topographic and hydrological indices and final ARA extent; and (iv) developed an accuracy-efficiency tradeoff analysis framework and assessed outputs derived from a range of DEM inputs for accuracy and efficiency. It has been found that 5-m smoothed LiDAR DEM can achieve relatively high accuracy in ARA results, while allowing data processing within a reasonable time frame. Additionally, provincial-scale hydrological network can represent spatial explicit creeks and headwaters at local spatial scales and incorporate them into the ARA delineation and ultimately riparian conservation planning. Given these facts, the combination of 5-m smoothed LiDAR DEM and high-resolution provincial hydrological network (e.g. 1:10,000 NBHN) is recommended for future ARA delineations, especially those applied across multiple watersheds or large (eco-)regions.

The applicability of novel terraces and meander belt delineation frameworks was tested in two study watersheds with different topographic relief settings in New Brunswick. It is believed that they can enhance the ability of ARA framework in terms of

informing flood control and management, and fluvial hazard risk assessment and mitigation practices across boarder (eco-) regions by allowing conversation planners to identify the former floodplain and channel migration extents.

As discussed earlier, effective conservation of riparian areas is important; accurate delineation of functional riparian extent is an irreplaceable prerequisite to this initiative. However, functional riparian delineation framework, to date, is still an open research topic, since features of riparian areas, such as spatial complexity within the landscape as transitional zones and sensitivity to disturbance, make their integration for management and delineation challenging (Salo et al., 2016; De Sosa et al., 2018). This study contributes to functional riparian area delineation initiatives by testing and refining a relatively new spatial methodology at the sub-watershed level. The findings and recommendations provided by this study further enhance the efficacy of the ARA framework, and ultimately the confidence in modelled ARA outputs for application in riparian conservation and fluvial hazard risk mitigation contexts across the entire Northern Appalachian / Acadian Ecoregion and/or other broad geographic regions in the future.

References

Abood, S. A., Maclean, A. L., & Mason, L. A. (2012). Modeling Riparian Zones Utilizing DEMS and Flood Height Data. *Photogrammetric Engineering & Remote Sensing*, *78*(3), 259–269.

Alber, A., & Piégay, H. (2011). Spatial disaggregation and aggregation procedures for characterizing fluvial features at the network-scale: Application to the Rhône basin (France). *Geomorphology*, *125*(3), 343–360.

Anderson RS, Anderson SP. (2010). Geomorphology: The Mechanics and Chemistry of Landscapes. Cambridge University Press: Cambridge.

Andrle, R. (1996). Measuring channel planform of meandering rivers. *Physical Geography*. 17(3): 270-281.

Aunan, T., Palik, B., & Verry, S. (2005). A GIS approach for delineating variable-width riparian buffers based on hydrological function. *Minnesota Department of Natural Resources*, 1–14. Retrieved from http://mn.gov/frc/documents/council/Variable-Width_Riparian_Buffers_2005-01-26_Report.pdf.

Barber, C. P., & Shortridge, A. (2005). Lidar Elevation Data for Surface Hydrologic Modeling: Resolution and Representation Issues. *Cartography and Geographic Information Science*, *32*(4), 401–410.

Barash, D. (2002). A fundamental relationship between bilateral filtering, adaptive smoothing, and the nonlinear diffusion equation. IEEE Trans. Pattern Anal. Mach. Intell. 26, 844–847.

Barnett, A. (2011). Active River Area (ARA) Three Stream Class (3SC) Toolbox and Toolbox Documentation. The Nature Conservancy Eastern Division.

Bater, C. W., & Coops, N. C. (2009). Evaluating error associated with lidar-derived DEM interpolation. *Computers & Geosciences*, 35(2), 289-300.

Benda. L., Hassan. A.M., Church. M., May. L.C. (2007). Geomorphology of Steepland Headwaters: The Transition from Hillslopes to Channels. *Journal of the American Water Resources Association.*41(4): 835-851.

Benda, L., Miller, D., & Barquän, J. (2011). Creating a catchment scale perspective for river restoration. *Hydrology and Earth System Sciences*, *15*(9), 2995–3015.

Biron, P.M., Buffin-Bélanger, T., Larocque, M. et al. (2014). Freedom Space for Rivers: A Sustainable Management Approach to Enhance River Resilience. Environmental Management 54, 1056–1073

Bridge JS. (2003). Rivers and Floodplains Forms, Processes, and Sedimentary Record (1st edn). Blackwell Science: Oxford.

Burns CE, C Peoples, M Fields, A Barnett (2012). Protecting North Carolina's freshwater systems: A state-wide assessment of biodiversity, condition and opportunity. The Nature Conservancy.

Callow, J.N., van Niel, K.P. and Boggs, G.S. (2007): How does modifying a DEM to reflect known hydrology affect subsequent terrain analysis? Journal of Hydrology 332, 30-39.

Cameron, H. and Bauer, B. (2014). River Bank Erosion Processes along the Lower Shuswap River (Final Project Report submitted to Regional District of North Okanagan). University of British Columbia Okanagan. Retrieved from: http://www.rdno.ca/docs/RIVER_BANK_EROSION_PROCESSES_ALONG_THE_LOWER_SHUSWAP_RIVER.pdf

Campbell, J. B., & Wynne, R. H. (2011). Introduction to remote sensing. Guilford Press.

Carlisle, B. H. (2005). Modelling the spatial distribution of DEM error. *Transactions in GIS,* 9(4), 521–540.

Carson, M.A. and Lapointe M.F. (1983). The inherent asymmetry of river meander planform. *Journal of Geology*, 91: 41-55.

Charlton, R. (2008). Fundamentals of fluvial geomorphology. Oxon, UK: Routledge.

Clubb. J. F. Mudd. M. S., Milodowski T.D., Valters.A.D., Slater.J.L, Hurst D.M. and Limaye.B.A. (2017). Geomorphometric delineation of floodplains and terraces from objectively defined topographic thresholds. *Earth Surf. Dynam*. 5, 369–385.

Cohen, J. (1960). A coefficient of agreement for nominal scales. *Educational and psychological measuremen*t, 20(1), 37-46.

Colpitts, M.C., Fahmy, S.H., MacDougall.J.E (1995). Forest Soils of New Brunswick. (No. 95-38). Fredericton, NB: New Brunswick Department of Natural Resources and Energy Timber Management Branch

Connors. B. (2019, November 29). Email interview.

Conservation Gateways (n.d.). North America Headwaters and Creeks. Retrieved from https://www.conservationgateway.org/ConservationByGeography/NorthAmerica/UnitedStates/edc/reportsdata/hg/fw/Pages/headwaters.aspx

Crawford, J. A., & Semlitsch, R. D. (2007). Estimation of core terrestrial habitat for stream-breeding salamanders and delineation of riparian buffers for protection of biodiversity. *Conservation Biology*, *21*(1), 152–158.

DataQC (2009). NB Spatial Data Standards Evolution-Proprity Updates. DataQC. Fredericton, NB.

Demoulin A, Bovy B, Rixhon G, Cornet Y. (2007). An automated method to extract fluvial terraces from digital elevation models: the Vesdre valley, a case study in eastern Belgium. *Geomorphology* 91(1–2): 51–64.

De Sosa, L. L., Glanville, H. C., Marshall, M. R., Abood, S. A., Williams, A. P., & Jones, D. L. (2018). Delineating and mapping riparian areas for ecosystem service assessment. Ecohydrology, 11(2), e1928.

Donovan, S. K. (2015). Landmarks by Robert McFarlane. Hamish Hamilton, London, Geological Journal, 50(5), 705-705.

Dorren. L. K.A., Frederic Berger, Anton C. Imeson, Bernhard Maier, Freddy Rey (2004). Integrity, stability and management of protection forests in the European Alps. *Forest Ecology and Management,* 195 (2004): 165–176.

Environment Canada (n.d.). Canadian Climate Normals, 1971-2000 [online]. Retrieved from www.climate.weatheroffice. ec.gc.ca/climate_normals/index_e.html.

Environmental Law Institute. (2003). Conservation Thresholds for Land Use Planners. Washington D.C. Retrieved from: https://www.eli.org/sites/default/files/eli-pubs/d13-04.pdf

Environmental Systems Research Institute (ESRI). (2018). ArcGIS Pro Release 2.2. Redlands, CA.

Environmental Systems Research Institute (ESRI) (2018). ArcGIS Pro Tool Reference-Cost Distance. Retrieved from: https://pro.arcgis.com/en/pro-app/tool-reference/spatial-analyst/cost-distance.htm

Environmental Systems Research Institute (ESRI) (2018). ArcGIS Pro Tool Reference-Compute Confusion Matrix. Retrieved from: https://pro.arcgis.com/en/pro-app/tool-reference/image-analyst/compute-confusion-matrix.htm

Environmental Systems Research Institute (ESRI) (2016). ArcGIS Pro Tool Reference-Resample. Retrieved from: https://pro.arcgis.com/en/pro-app/tool-reference/data-management/resample.htm

Erin Swansburg, Nassir El-Jabi, Daniel Caissie, Gérald Chaput (2004). Hydrometeorological Trends in the Miramichi River, Canada: Implications for Atlantic Salmon Growth. *North American Journal of Fiseeries Management.* 24: 561-576.

Faustini.M.J, Kaufmann.R.P, Herlihy.T.A (2009). Downstream variation in bankfull width of wadeable streams across the conterminous United States. *Geomorphology*. 108(3-4): 292-311.

Fereshtehpour, M., & Karamouz, M. (2018). DEM resolution effects on coastal flood vulnerability assessment: Deterministic and probabilistic approach. *Water Resources Research*, 54, 4965–4982.

Ferguson, R. I. (1975). Meander irregularity and wavelength estimation. *Journal of Hydrology*, 26(3-4), 315-333.

Fernández, D., Barquín, J., Álvarez-Cabria, M., & Peñas, F. J. (2012). Quantifying the performance of automated GIS-based geomorphological approaches for riparian zone delineation using digital elevation models. *Hydrology and Earth System Sciences*, *16*(10), 3851–3862.

Finnegan NJ, Dietrich WE (2011). Episodic bedrock strath terrace formation due to meander migration and cutoff. *Geology* 39(2): 143–146.

Fisher, P. F., & Tate, N. J. (2006). Causes and consequences of error in digital elevation models. *Progress in physical Geography*, 30(4), 467-489.

Foody, G. M. (2002). Status of land cover classification accuracy assessment. *Remote sensing of environment*, 80(1), 185-201.

GeoNB (2019). LiDAR Digital Elevation Model [Data File]. Retireved from http://geonb.snb.ca/nbdem/

GeoNB (2018). New Brunswick Hydrographic Network [Data File]. Retireved from http://geonb.snb.ca/downloads/nbhn/geonb_nbhn-rhnb_shp.zip

GeoNB (2015). Forest Soils [Data File]. Retiredved from http://www.snb.ca/geonb1/e/DC/forestsoils.asp

GeoNB (2011). Flood Risk Areas and Historical Floods [Data File]. Retiredved from http://geonb.snb.ca/downloads/flood/geonb_floodriskareas-zonesinondables_shp.zip

GeoNB (2016). 2016 Digital Elevation Model. Retrieved from: https://geonb.snb.ca/downloads2/elevation/2016/dem/meta/2016_dem_metadata.html

GeoNB (2018). 2018 Digital Elevation Model. Retrieved from: https://geonb.snb.ca/downloads2/elevation/2018/dem/meta/2018_dem_metadata_aoi1.html

Geotech. org (n.d.) Dictionary of Geological Terms. Retrieved from https://web.archive.org/web/20110501155938/http://www.geotech.org/survey/geotech/dictiona.html

Government of New Brunswick (2013). New Brunswick Hydrographic Network initiative nominated for national award. Retrieved from: https://www2.gnb.ca/content/gnb/en/news/news_release.2013.10.0987.html

Gurnell, A. M. (1997). Channel change on the River Dee meanders, 1946-1992, from the analysis of air photographs. Regulated Rivers: Research and Management 13:13-26.

Habtezion, N.; Tahmasebi Nasab, M.; Chu, X. (2016) How does DEM resolution affect microtopographic characteristics, hydrologic connectivity, and modelling of hydrologic processes? *Hydrological Process*. 30, 4870–4892.

Haile, A. T., & Rientjes, T. H. M. (2005). Effects of LiDAR DEM resolution in flood modelling: a model sensitivity study for the city of Tegucigalpa, Honduras.

Ham, D. G., and M. Church. (2000). Bed-material transport estimated from channel morphodynamics, Chilliwack River, British Columbia. Earth Surface Processes and Landforms 25:1123-1142.

Harvey J, Gooseff M. (2015). Consequences from bedforms to basins. Water Resources Research 51: 6893–6922.

Hawker, L., Bates, P., Neal, J., & Rougier, J. (2018). Perspectives on digital elevation model (DEM) simulation for flood modeling in the absence of a high-accuracy open access global DEM. *Frontiers in Earth Science*, 6, 233.

Hellweger, F. (1997). AGREE - DEM Surface Reconditioning System. Austin, TX: University of Texas Austin.

Hengl Tomislav (2006). Finding the right pixel size. *Computers and Geosciences*. 32(9): 1283-1298.

Hickin, E. J., and G. Nanson. (1975). The character of channel migration on the Beatton River, northeast British Columbia, Canada. Geological Society of America Bulletin 86:487-494.

Holmes, K., & Goebel, P. (2011). A functional approach to riparian area delineation using geospatial methods. *Journal of Forestry*, *109*(4), 233–241.

Holmes, K. W., Chadwick, O. A., and Kydriakidis, P. C. (2000). Error in a USGS 30-meter digital elevation model and its impact on terrain modelling. *Journal of Hydrology*. 233, 154–173.

Hooke, J.M. (1984). Changes in river meanders: a review of techniques and results of analyses. *Progress in Physical Geography*, 8: 473-508.

Hooke, J. and Yorke, L. (2010). Rates, distributions and mechanisms of change in meander morphology over decadal time scales, River Dan, UK. *Earth surface processes and landforms*, 35, 1601-1614.

Howett, Julia (2017). Meander belt delineation: Developing a predictive model for meander belt width. (unpublished master dissertation). The University of Western Ontario. London, ON.

Hudson, P. F., & Colditz, R. R. (2003). Flood delineation in a large and complex alluvial valley, lower Pánuco basin, Mexico. *Journal of Hydrology*, *280*(1–4), 229–245.

Hunter, G. J., and Goodchild, M. F. (1997). Modelling the uncertainty of slope and aspect derived from spatial databases. *Geophys. Anal*. 29, 35–50.

I.A. Thomas, P. Jordan, O. Shine, O. Fenton, P.-E. Mellander, P. Dunlop, P.N.C. Murphy (2017). Defining optimal DEM resolutions and point densities for modelling hydrologically sensitive areas in agricultural catchments dominated by microtopography. *International Journal of Applied Earth Observation and Geoinformation*. 54:38-52.

lhart B.L.,Verry E.S. & Palik B.J. (2000). Defining Riparian Areas. *Forest and the Riparian zone* 7-13.

Ismail, M. H., & Jusoff, K. (2008). Satellite data classification accuracy assessment based from reference dataset. *International Journal of Computer and Information Science and Engineering*, 2(2), 96-102.

Janssen, L. L., & Vanderwel, F. J. (1994). Accuracy assessment of satellite derived land-cover data: a review. *Photogrammetric engineering and remote sensing;(United States),* 60(4).

Jenson, S. K., and J. O. Domingue. (1988). "Extracting Topographic Structure from Digital Elevation Data for Geographic Information System Analysis." Photogrammetric Engineering and Remote Sensing 54 (11): 1593–1600.

Johansen, K., Tiede, D., Blaschke, T., Arroyo, L. A., & Phinn, S. (2011). Automatic geographic object based mapping of streambed and riparian zone extent from LiDAR data in a temperate rural urban environment, Australia. *Remote Sensing*, *3*(6), 1139–1156.

Kidd.S.D., Curry.R.A and Munkittrick.K.R (2011). The Saint John River: A State of the Environment Report. Retrieved from: https://www.unb.ca/research/institutes/cri/_resources/pdfs/criday2011/cri_sjr_soe_final.pdf

Kline, Mike and Dolan, Kari (2008). River Corridor Protection Guide: Montpelier, VT, 2008. Retrieved from the website of Vermont Agency of Natural Resources https://anr.vermont.gov/sites/anr/files/co/planning/documents/guidance/River%20Corridor%20Protection%20Guide.pdf

Kuglerová, L., Ågren, A., Jansson, R., & Laudon, H. (2014). Towards optimizing riparian buffer zones: Ecological and biogeochemical implications for forest management. *Forest Ecology and Management*, *334*, 74–84.

Kusnierz.D. and Wang.B. (2010). Penobscot River Active River Area Pilot Project: Aquatic Conservation Blueprint. Retrieved from: https://www.conservationgateway.org/ConservationByGeography/NorthAmerica/UnitedStates/edc/Documents/ED_freshwater_ARA_Penobscot%20River%20ARA%20Pilot%20Project%20Report%2011-30-10.pdf.

Kuo, W.L., Steenhuis, T.S., McCulloch, C.E., Mohler, C.L., Weinstein, D.A., DeGloria,S.D., Swaney, D.P. (1999). Effect of grid size on runoff and soil moisture for a variable-source-area hydrology model. *Water Resources Research*. 35 (11): 3419–3428.

Lagasse, P., Zevenbergen, L., Spitz, W., & Thorne, C. (2004). Methodology for predicting channel migration. NCHRP Web-Only Document 67 (Project 24-16). Report prepared for TRB (Transportation Research Board of the National Academies of the US). Retrieved from: http://onlinepubs.trb.org/onlinepubs/nchrp/nchrp_w67.pdf.

Lin, S., Jing, C., Chaplot, V., Yu, X., Zhang, Z., Moore, N., & Wu, J. (2010). Effect of DEM resolution on SWAT outputs of runoff, sediment and nutrients. *Hydrology and Earth System Sciences Discussions*, 7(4), 4411-4435.

Lindsay.J.B., Francioni. A., and Cockburn. J.M. (2019). LiDAR DEM Smoothing and the Preservation of Drainage Features. *Remote Sensing*. 11 (16): 1926.

Lindsay, J.B. WhiteboxTools User Manual. Available online: https://jblindsay.github.io/wbt_book/preface.html (accessed on Oct. 16, 2019).

Luke, S. H., Slade, E. M., Gray, C. L., Annammala, K. V., Drewer, J., Williamson, J., & Struebig, M. J. (2019). Riparian buffers in tropical agriculture: Scientific support, effectiveness and directions for policy. *Journal of applied ecology*, 56(1), 85-92.

MacMillan, R.A.; Martin, T.C.; Earle, T.J.; McNabb, D.H. (2003) Automated analysis and classification of landforms using high-resolution digital elevation data: applications and issues. *Canadian Journal of Remote Sensing*. 29, 592–606.

Marangelo.P. and Farrell. D. (2010) A Conservation Blueprint for the Poultney River watershed, VT using the Active River Area conservation framework. Retrieved from:https://www.conservationgateway.org/ConservationByGeography/NorthAmerica/UnitedStates/edc/Documents/ED_freshwater_ARA_Poultney%20River%20Conservation%20Blueprint%2011_30_2010.pdf

Marangelo. P. and Farrell. D. (2010). A Conservation Blueprint for Lewis Creek, VY using the Active River Area conservation framework. Retrieved from https://www.conservationgateway.org/ConservationByGeography/NorthAmerica/UnitedStates/edc/Documents/ED_freshwater_ARA_%20A%20Conservation%20Blueprint%20for%20Lewis%20Creek%2011_30_2010.pdf

Master, L. L., S. R. Flack, and B. A. Stein (Editors), (1998). Rivers of Life: Critical Watersheds for Protecting Freshwater Biodiversity, The Nature Conservancy, Arlington, VA.

Millar, W., Olivero-Sheldon, A., Nussey, P. & Noseworthy, J. (2019). A Stream Classification for the Northern Appalachian–Acadian Region of Canada, Version 2.0. Fredericton, New Brunswick: Nature Conservancy of Canada, Atlantic Regional Office

Miramichi River Envrionemtal Assessment Committee (n.d.). A Multi-Stakeholder ENGO with a focus on science and research on the Miramichi Watershed. Retireved from: https://mreac.org/watershed/

Montgomery, D. R., & Buffington, J. M. (1993). Channel classification, prediction of channel response, and assessment of channel condition. Washington State Timber, Fish & Wildlife.

My New Brunswick (2015). Miramichi River. Retrieved from: https://mynewbrunswick.ca/miramichi-river/

Nagel, David E.; Buffington, John M.; Parkes, Sharon L.; Wenger, Seth; Goode, Jaime R. (2014). A landscape scale valley confinement algorithm: Delineating unconfined valley bottoms for geomorphic, aquatic, and riparian applications. Gen. Tech. Rep. RMRS-GTR- 321. Fort Collins, CO: U.S. Department of Agriculture, Forest Service, Rocky Mountain Research Station. 42 p.

Naiman and, R. J., & Décamps, H. (1997). THE ECOLOGY OF INTERFACES:Riparian Zones. *Annual Review of Ecology and Systematics*, *28*(1), 621–658.

National Research Council. 2002. Riparian Areas: Functions and Strategies for Management. Washington, DC: The National Academies Press.

Nelson, A., Reuter, H. I., & Gessler, P. (2009). DEM production methods and sources. *Developments in soil science*, 33, 65-85.

Neuendorf, K.K.E., J.P. Mehl, Jr., and J.A. Jackson, J.A. (2005) Glossary of Geology (5th edition.). Alexandria, Virginia, American Geological Institute.

Nilsson, C., & Berggren, K. (2000). Alterations of Riparian Ecosystems Caused by River Regulation. BioScience, 50(9), 783–792.

Noe, G. B. and C. R. Hupp, (2005). Carbon, Nitrogen, and Phosphorus Accumulation in Floodplains of Atlantic Coastal Plain Rivers, USA. Ecological Applications 15(4):1178-1190.

Noseworthy, J., Millar, W. & Nussey, P. (2019). An Aquatic Connectivity Tool for the Northern Appalachian–Acadian Region of Canada. Nature Conservancy of Canada, Atlantic Regional Office. Fredericton, New Brunswick.

Nussey, P. & Noseworthy, J. (2020). The Active River Area for the Northern Appalachian–Acadian Region of Canada. Nature Conservancy of Canada. Atlantic Regional Office. Fredericton, New Brunswick

Olivero Sheldon, A., Barnett, A. and Anderson, M.G. (2015). A Stream Classification for the Appalachian Region. The Nature Conservancy, Eastern Conservation Science, Eastern Regional Office. Boston, MA.

Open Oregon (n.d.) Assessing slope of the land. Retrieved from https://openoregon.pressbooks.pub/forestmeasurements/chapter/1-1-assessing-slope-of-the-land/

Palik, B., Tang, S. M., & Chavez, Q. (2004). Estimating riparian area extent and land use in the Midwest, 28.

Parish Geomorphic. (2004). Belt Width Delineation Procedures (Report No. 98-023-Final Report). Toronto and Region Conservation Authority. Retrieved from https://sustainabletechnologies.ca/app/uploads/2013/01/Belt-Width-Delineation-Procedures.pdf

Pazzaglia FJ. (2013. 9.22) Fluvial terraces. In Treatise on Geomorphology, John FS (ed). Academic Press: San Diego; 379–412

Peel, M. C., Finlayson, B. L., and McMahon, T. A. (2007). Updated world map of the Köppen-Geiger climate classification. Hydrol. Earth Syst. Sci. 11, 1633-1644.

Perkins, D. W., & Hunter, Jr., M. L. (2006). Use of amphibians to define riparian zones of headwater streams. *Canadian Journal of Forest Research*, *36*(9), 2124–2130.

Petrasova, A., Mitasova, H., Petras, V., & Jeziorska, J. (2017). Fusion of high-resolution DEMs for water flow modeling. *Open Geospatial Data, Software and Standards*, 2(1), 6.

Petrovszki, J.; Székely, B.; Timár, G. (2012). A systematic overview of the coincidences of river sinuosity changes and tectonically active structures in the Pannonian Basin. *Glob. Planet. Chang*. 98–99, 109–121

Piegay, H., Darby, S., Mosselman, E., & Surian, N. (2005). A review of techniques available for delimiting the erodible river corridor: a sustainable approach to managing riverbank erosion. River Research and Applications, 21, 773-789.

Polvi, L. E., Wohl, E. E., & Merritt, D. M. (2011). Geomorphic and process domain controls on riparian zones in the Colorado Front Range. *Geomorphology*, *125*(4), 504–516.

Poppenga, S.K., Worstell, B.B., Stoker, J.M., and Greenlee, S.K., (2009), Comparison of surface flow features from lidar-derived digital elevation models with historical elevation and hydrography data for Minnehaha County, South Dakota: U.S. Geological Survey Scientific Investigations Report 2009–5065, 24 p.

Rapp, C., & Abbe, T. (2003). A Framework for Delineating Channel Migration Zones (03-06-027). Washington State Department of Transportation. Retrieved from: https://fortress.wa.gov/ecy/publications/documents/0306027.pdf

Richardson, J. S., Naiman, R. J., & Bisson, P. A. (2012). How did fixed-width buffers become standard practice for protecting freshwaters and their riparian areas from forest harvest practices? Freshwater Science, 31(1), 232–238.

Richardson, D. M., Holmes, P. M., Esler, K. J., Galatowitsch, S. M., Stromberg, J. C., Kirkman, S. P. Hobbs, R. J. (2007). Riparian vegetation: Degradation, alien plant invasions, and restoration prospects. *Diversity and Distributions*, *13*(1), 126–139.

Robinson, T. S. (2017). Mapping ecologically functional riparian corridors using LiDAR and hydrologic landscape analysis (unpublished master's thesis), San Francisco State University, San Francisco, U.S.A.

Rosgen, D.L. (1996). Applied River Morphology. Wildland Hydrology, Pagosa Springs, Colorado.

Saddi Mustafa and Athanasopoulos-Zekko Adda (2013). A GIS-Enabled Approach for Assessing DamagePotential of Levee Systems Based on Underlying Geologyand River Morphology. *Mathematical Problems in Engineering.* 2013.

Saksena, S., & Merwade, V. (2015). Incorporating the effect of DEM resolution and accuracy for improved flood inundation mapping. *Journal of Hydrology*, 530, 180–194.

Salo, J. A., Theobald, D. M., & Brown, T. C. (2016). Evaluation of methods for delineating riparian zones in a semi-arid montane watershed. *JAWRA Journal of the American Water Resources Association*, 52, 632–647.

Sangster, C. (2002). Validating LiDAR – evaluating LiDAR accuracy using GPS. Lawrencetown, Nova Scotia: Applied Geomatics Research Group, Centre of Geographic Science.

Shoutis, L., Patten, D. T., & McGlynn, B. (2010). Terrain-based predictive modeling of riparian vegetation in a northern rocky mountain watershed. *Wetlands*, *30*(3), 621–633.

Shumilova, O., Tockner, K., Thieme, M., Koska, A. & Zarfl, C. (2018) Global water transfer megaprojects: a potential solution for the water-food-energy nexus? Front. Environ. Sci. 6, 150.

Smith, M.P., Schiff, R., Olivero, A. and MacBroom, J.G., (2008). THE ACTIVE RIVER AREA: A Conservation Framework for Protecting Rivers and Streams. The Nature Conservancy, Boston, MA.

Stout JC, Belmont P. (2014). TerEx Toolbox for semi-automated selection of fluvial terrace and floodplain features from lidar. *Earth Surface Processes and Landforms* 39: 569–580.

Strager, J. M., C. B. Yuill, and P. Bohall Wood, (2000). Landscape-Based Riparian Habitat Modeling for Amphibians and Reptiles Using Arc/Info Grid and Arcview. ESRI User Conference 2000, Paper 575. GIS.

Strahler, A.N., (1957). Quantitative Analysis of Watershed Geomorphology. *American Geophysical Union Transactions* 38:913-920.

Suárez, J. C., Ontiveros, C., Smith, S., & Snape, S. (2005). Use of airborne LiDAR and aerial photography in the estimation of individual tree heights in forestry. *Computers and Geosciences*, *31*(2), 253–262.

Su Fanok, Michele DePhilip, Ellen Creveling, Mari-Beth DeLucia, and Tara Moberg (2010). A Freshwater Conservation Assessment for the Upper Delaware River Basin. Retrieved from: https://www.conservationgateway.org/ConservationByGeography/NorthAmerica/UnitedStates/edc/Documents/ED_freshwater_ara_A%20Freshwater%20Conservation%20Assessment%20for%20the%20Upper%20Delaware%20River%20Basin_compressed.pdf

Swansburg. E. El-Jabi.N., Caissie.D.,Chaput.G. (2011). Hydrometeorological Trends in the Miramichi River, Canada: Implications for Atlantic Salmon Growth. *North American Journal of Fisheries Management.* 24: 561-576.

The Nature Conservancy (2015). Conservation Gateway-Floodplain Assessment. Retrieved from https://www.conservationgateway.org/ConservationByGeography/NorthAmerica/UnitedStates/edc/reportsdata/freshwater/floodplains/Pages/default.aspx

Thompson, J.A., Bell, J.C., Butler, C.A. (2001). Digital elevation model resolution: effects on terrain attribute calculation and quantitative soil-landscape modeling. *Geoderma*. 100, 67–89.

USask (University of Saskatchewan, Department of Soil Science).(2010) Undated b. Soils of Canada, Order: Podzolic [online]. Retrieved from: www.soilsofcanada.ca/orders/podzolic/ index.php.

U.S. Environmental Protection Agency (n.d.) Stream Corridor Structure: A Longitude View. Retrieved from Watershed Academy Website: https://cfpub.epa.gov/watertrain/moduleFrame.cfm?parent_object_id=652

Vaze, J., & Teng, J. (2007). High resolution LiDAR DEM–how good is it. Modelling and Simulation, 692-698.

Vaze, J., Teng, J., Spencer, G., (2010). Impact of DEM accuracy and resolution on topographic indices. Environ. *Modell. Softw*. 25, 1086–1098.

Verry, E. S., Dolloff, C. A., & Manning, M. E. (2004). Riparian ecotone: A functional definition and delineation for resource assessment. *Water, Air, and Soil Pollution: Focus*, *4*(1), 67–94.

Wang Suiji and Ni Jinren (2002). Straight rivers: its formation and speciality. *Journal of Geographical Sciences*. 12(1): 72-80.

Ward, J. V., K. Tockner, D. B. Arscott, and C. Claret, 2002. Riverine Landscape Diversity. Freshwater Biology 47(4):517-539.

Wechsler, S. P. (2007). Uncertainties associated with digital elevation models for hydrologic applications: A review. *Hydrology and Earth System Sciences,* 11(4), 1481–1500.

Wikipedia (n.d.). Miramichi River. Retrieved from https://en.wikipedia.org/wiki/Miramichi_River#See_also

Williams, G.P. (1986). River Meanders and Channel Size. *Journal of Hydrology* 88:147-164.

Wu, S., Li, J., Huang, G.H. (2008). A study on DEM-derived primary topographic attributes for hydrologic applications: sensitivity to elevation data resolution. *Applied Geography*. 28, 210–223.

Yan.Q., Iwasaki.T., Stumpf.A., Belmont.P., Parker.G., Kuma.P. (2017). Hydro-geomorphological differentiation between floodplains and terraces. *Earth Surf. Process. Landforms*. 43, 218-228.

Yang, X. (2007). Integrated use of remote sensing and geographic information systems in riparian vegetation delineation and mapping, *1161*.

Zaimes, G.N.; Schultz, R.C.; Isenhart, T.M. (2004). Stream bank erosion adjacent to riparian forest buffers, row-crop fields, and continuously grazed pastures along Bear Creek in central Iowa. *Journal of Soil Water Conservation*. 59: 19–27.

Zarfl, C., Lumsdon, A. E., Berlekamp, J., Tydecks, L. & Tockner, K. (2015). A global boom in hydropower dam construction. Aquat. Sci. 77, 161–170

Zelazny, V. (2007). Our landscape heritage – The story of ecological land classification in New Brunswick (2nd ed.). New Brunswick Dept. of Natural Resources, Fredericton, NB

Zhang Bin, Al Nanshan, Huang Zhnegwen, Yi ChengBo, Qin FaCao (2008). Meanders of the Jialing River in China: Morphology and formation. *Chinese Science Bulletin*. 53(2):267-281

Zhang, W., & Montgomery, D. R. (1994). Digital elevation model grid size, landscape representation, and hydrologic simulations. *Water resources research*, 30(4), 1019-1028.

Ziadat, F.M. (2007) Effect of contour intervals and grid cell size on the accuracy of DEMs and slop derivatives. *Transactions in GIS* 11, 67–81.

Appendix A. Cost Distance Thresholds

Table A.1 Lower Saint John River Watershed Cost Distance Thresholds

	Great Basezone (Terraces)	Medium Basezone (Terraces)	Small Basezone (Terraces)	Creeks Basezone	Headwaters Basezone
SRTM 30-m	1000	450	350	100	75
30-m LiDAR	600	450	350	100	75
15-m LiDAR	600	450	350	100	75
10-m LiDAR	600	450	350	80	50
5-m LiDAR	550 (260)	450 (220)	300 (160)	80	40
3-m LiDAR	500 (250)	400 (170)	300 (150)	80	40
5-m (smooth) LiDAR	700 (300)	600 (270)	300 (140)	80	40
3-m (smooth) LiDAR	750 (400)	500 (290)	400 (230)	80	40

Table A.2 Miramichi River Basin Watershed Cost Distance Thresholds

	Slope Class	Great Basezone (Terraces)	Medium Basezone (Terraces)	Small Basezone (Terraces)	Creeks Basezone	Headwaters Basezone
SRTM 30-m	SC-1		600	400	100	100
	SC-2	500	450	350	100	75
30-m LiDAR	SC-1	500	550	400	100	100
	SC-2		450	350	100	75
15-m LiDAR	SC-1		600	400	100	100
	SC-2	500	500	350	100	75
10-m LiDAR	SC-1		450	350	100	75
	SC-2	450	450	350	80	50
5-m LiDAR	SC-1		400 (200)	350 (100)	80	60
	SC-2	400 (230)	400 (220)	300 (180)	80	50
3-m LiDAR	SC-1		400 (220)	350 (135)	80	60
	SC-2	400 (300)	350 (140)	300 (120)	80	50
5-m (smooth) LiDAR	SC-1		400 (220)	400 (190)	80	60
	SC-2	450 (230)	400 (190)	350 (180)	80	50
3-m (smooth) LiDAR	SC-1		450 (270)	400 (150)	100	60
	SC-2	500 (200)	400 (150)	350 (140)	100	50

Appendix B. Riverbank Lithology Types

Table B. Full list of riverbank lithology types

Primary Lithology	Soil Unit	Mode of Deposition
Argillaceous limestones	Siegas (SE)	Compact till
	Caribou (CA)	Non-compact till
	Undine (UN)	Residual
Calcareous siltstones, calcareous sandstones and/or calcareous slates	Kedgwick (KE)	Compact till
	Carleton (CR)	
	Thibault (TH)	Non-compact till
	Muniac (MU)	Glaciofluvial
Grey calcareous mudstones and/or feldspathic to lithic sandstones	Saltsprings (SS)	Compact till
	Erb Settlement (EB)	Non-compact till or residual
Red polymictic conglomerates, feldspathic to lithic sandstones and/or mud stones	Salisbury (SA)	Compact till
	Parry (PR)	
	Cornhill (CH)	Residual
	Parleeville Tobique (PT)	Non-compact till
	Kennebecasis (KN)	Glaciofluvial
	Tracadie (TD)	Glaciomarine or lacustrine
Metaquartzites, slates, metasiltstones, metasandstones, metaconglomerates and/or metawackes	Holmesville (HM)	Compact till
	Victoria (VI)	Non-compact till
	McGee (MG)	
	Glassville (GE)	Residual
	Grand Falls (GF)	Glaciofluvial
Red mudstones (weathered)	Stony Brook (SB)	Compact till
	Tracy (TR)	
	Harcourt (HT)	
	Bacaguimec (BE)	Non-compact till
	Barrieau-Buctouche (BB)	Glaciomarine/compact till
Grey lithic-feldsapthic sandstones	Reece (RE)	Compact till
	Sunbury (SN)	Non-compact till
	Fair lsle (FA)	Residual
	Riverbank (RI)	Glaciofluvial, marine or eolian
Mafic volcanic rocks, gabbro and/or diorites	Tetagouche (TT)	Compact till
	Kingston (KI)	
	Mafic Volcanic (MV)	Residual or non-compact till
Gneiss, granites, alkali granites, granodiorites and/or quartz diorites	Tuadook (TU)	Compact till
	Juniper (JU)	Non-compact till
	Big Baid Mountain (BD)	Residual

Primary Lithology	Soil Unit	Mode of Deposition
Felsic volcanic or mixed igneous rocks and/or felsic pebble conglomerates	Popple Depot (PD)	Compact till
	Jacquet River (JR)	Non-compact till
	Lomond (LO)	Non-compact till or residual
	Gagetown (GG)	Marine or glaciofluvial
Metasedimentary rocks mixed with igneous rocks	Long Lake (LL)	Compact till
	Britt Brook (BR)	Non-compact till
	Serpentine (SP)	Residual
Igneous rocks mixed with metasedimentary rocks	Catamaran (CT)	Compact till
	Irving (IR)	Non-compact till
	Pinder (PI)	Residual
Grey-red sandstones or mudstones mixed with igneous rocks	Rogersville (RG)	Compact till
Undifferentiated	Interval (IN)	Alluvial
	Acadia (AC)	Tidal
	Organic Soil (OS)	Paludification
	Mining Debris (MD)	Anthropogenic

Appendix C. River Meander Reaches Information

Table C.1a Soil lithology legend (Lower St. John River Watershed)

1. Undifferentiated
2. Grey-red sandstones or mudstones mixed with igneous rocks
3. Igneous rocks mixed with metasedimentary rocks
4. Metasedimentary rocks mixed with igneous rocks
5. Felsic volcanic or mixed igneous rocks and/or felsic pebble conglomerates
6. Gneiss, granites, alkali granites, granodiorites and/or quartz diorites
7. Mafic volcanic rocks, gabbro and/or diorites
8. Grey lithic-feldsapthic sandstones
9. Red mudstones (weathered)
10. Metaquartzites, slates, metasiltstones, metasandstones, metaconglomerates and/or metawackes
11. Red polymictic conglomerates, feldspathic to lithic sandstones and/or mud stones
12. Grey calcareous mudstones and/or feldspathic to lithic sandstones
13. Calcareous siltstones, calcareous sandstones and/or calcareous slates

Table C. 1b River reaches information

Nashwaak River

	Soil lithology	**Gradient**	**Confinement**	**Sinuosity**
Reach 1	5	Moderate	Confine	Moderate
Reach 2	3	Moderate	Confine	Moderate
Reach 3	4	Moderate	Confine	Moderate
Reach 4	10	Moderate	Confine	Moderate
Reach 5	1	Low	Unconfine	Moderate

West Branch Nashwaak River

	Soil lithology	**Gradient**	**Confinement**	**Sinuosity**
Reach 1	3	Moderate	unconfine	Moderate

Mcbean Brook

	Soil lithology	**Gradient**	**Confinement**	**Sinuosity**
Reach 1	6	Moderate	Unconfine	High
Reach 2	3	Moderate	Unconfine	Moderate
Reach 3	5	Moderate	Unconfine	High

Napadogan Brook

	Soil lithology	**Gradient**	**Confinement**	**Sinuosity**
Reach 1	5	Moderate	Unconfine	Moderate
Reach 2	3	Moderate	Unconfine	Moderate

West Branch Napadogan Brook

	Soil lithology	Gradient	Confinement	Sinuosity
Reach 1	3	Moderate	Unconfine	Moderate
Reach 2	3	Moderate	Confine	Moderate

Cross Creek

	Soil lithology	Gradient	Confinement	Sinuosity
Reach 1	13	Moderate	Unconfine	High
Reach 2	8	Moderate	Unconfine	Moderate
Reach 3	8	Moderate	Confine	Moderate

Five Mile Brook

	Soil lithology	Gradient	Confinement	Sinuosity
Reach 1	8	Moderate	Unconfine	High

Mcgivney Brook

	Soil lithology	Gradient	Confinement	Sinuosity
Reach1	10	Moderate	Unconfine	High

Arnold Brook

	Soil lithology	Gradient	Confinement	Sinuosity
Reach 1	13	Moderate	Unconfine	High

Youngs Brook

	Soil lithology	Gradient	Confinement	Sinuosity
Reach 1	8	Moderate	Confine	Moderate

Mckenzie Brook

	Soil lithology	Gradient	Confinement	Sinuosity
Reach 1	8	Moderate	Confine	Moderate

Tay River

	Soil lithology	Gradient	Confinement	Sinuosity
Reach 1	11	Moderate	Unconfine	Moderate
Reach 2	8	Moderate	Unconfine	High
Reach 3	8	Moderate	Confine	Moderate
Reach 4	1	Moderate	Unconfine	Moderate

Limekiln Brook

	Soil lithology	Gradient	Confinement	Sinuosity
Reach 1	11	Moderate	Unconfine	Moderate
Reach 2	8	Moderate	Unconfine	High

South Branch Dunbar Stream

	Soil lithology	Gradient	Confinement	Sinuosity
Reach 1	8	Moderate	Unconfine	Moderate

Dunbar Stream

	Soil lithology	Gradient	Confinement	Sinuosity
Reach 1	8	Moderate	Unconfine	Moderate

Penniac Stream

	Soil lithology	Gradient	Confinement	Sinuosity
Reach 1	9	Moderate	Confine	High
Reach 2	1	Moderate	Unconfine	High

Oromocto River

	Soil lithology	Gradient	Confinement	Sinuosity
Reach 1	1	Low	Unconfine	Moderate

South Branch Oromocto River

	Soil lithology	Gradient	Confinement	Sinuosity
Reach 1	1	Low	Unconfine	High
Reach 2	13	Moderate	Confine	High
Reach 3	3	Moderate	Unconfine	Moderate
Reach 4	1	Moderate	Unconfine	High
Reach 5	3	Moderate	Unconfine	High
Reach 6	4	High	Unconfine	High

Sand Brook

	Soil lithology	Gradient	Confinement	Sinuosity
Reach 1	13	Moderate	Unconfine	High
Reach 2	4	Moderate	Unconfine	Moderate
Reach 3	4	high	Unconfine	High

Shin Creek

	Soil lithology	Gradient	Confinement	Sinuosity
Reach 1	5	Moderate	Unconfine	Moderate
Reach 2	11	Moderate	Confine	Moderate

Back Creek

	Soil lithology	Gradient	Confinement	Sinuosity
Reach 1	1	Low	Unconfine	High
Reach 2	5	Moderate	Unconfine	Moderate
Reach 3	10	Low	Unconfine	High

Mersereau Stream

	Soil lithology	Gradient	Confinement	Sinuosity
Reach 1	8	Moderate	Unconfine	High
Reach 2	9	Moderate	Unconfine	High
Reach 3	1	Low	Unconfine	High

Rusagonis Stream

	Soil lithology	Gradient	Confinement	Sinuosity
Reach 1	1	Low	Unconfine	High

North Branch Rusagonis Stream

	Soil lithology	Gradient	Confinement	Sinuosity
Reach 1	9	Moderate	Unconfine	Moderate

South Branch Rusagonis Stream

	Soil lithology	Gradient	Confinement	Sinuosity
Reach 1	8	Moderate	Unconfine	Moderate
Reach 2	9	Moderate	Unconfine	High

Brizley Stream

	Soil lithology	Gradient	Confinement	Sinuosity
Reach 1	9	Moderate	Unconfine	High
Reach 2	8	Moderate	Unconfine	High

Rockwell Stream

	Soil lithology	Gradient	Confinement	Sinuosity
Reach 1	9	Moderate	Unconfine	High
Reach 2	1	Low	Unconfine	Moderate

Three Tree Creek

	Soil lithology	Gradient	Confinement	Sinuosity
Reach 1	9	Moderate	Unconfine	High
Reach 2	1	Low	Unconfine	High

North Branch Oromocto River

	Soil	Gradient	Confinement	Sinuosity
Reach 1	8	Moderate	Unconfine	High
Reach 2	9	Moderate	Confine	High
Reach 3	1	Moderate	Unconfine	Moderate

Lyons Stream

	Soil lithology	Gradient	Confinement	Sinuosity
Reach 1	1	Low	Unconfine	High
Reach 2	8	Moderate	Unconfine	High

Yoho Stream

	Soil lithology	Gradient	Confinement	Sinuosity
Reach 1	9	Moderate	Unconfine	High

Porcupine Stream

	Soil lithology	Gradient	Confinement	Sinuosity
Reach 1	9	Moderate	Unconfine	High
Reach 2	1	Low	Unconfine	High
Reach 3	1	Moderate	Unconfine	High
Reach 4	9	Moderate	Unconfine	Moderate

Little Yoho Brook

	Soil lithology	Gradient	Confinement	Sinuosity
Reach 1	9	Moderate	Unconfine	High
Reach 2	1	Moderate	Unconfine	High

Little River

	Soil lithology	Gradient	Confinement	Sinuosity
Reach 1	8	Moderate	Confine	Moderate
Reach 2	9	Moderate	Confine	Moderate
Reach 3	8	Moderate	Confine	Moderate
Reach 4	1	Low	Unconfine	Moderate

Portobello Stream

	Soil lithology	Gradient	Confinement	Sinuosity
Reach 1	1	Low	Unconfine	High

Gaspereau River

	Soil lithology	Gradient	Confinement	Sinuosity
Reach 1	8	Low	Unconfine	High
Reach 2	8	Moderate	Confine	Moderate
Reach 3	8	Moderate	Unconfine	Moderate

Salmon River

	Soil lithology	Gradient	Confinement	Sinuosity
Reach 1	9	Moderate	Unconfine	High
Reach 2	9	Low	Unconfine	Moderate
Reach 3	9	Low	Confine	Moderate
Reach 4	1	Low	Unconfine	Moderate

Lake Stream

	Soil lithology	Gradient	Confinement	Sinuosity
Reach 1	9	Moderate	Unconfine	High

Big Forks Stream

	Soil lithology	Gradient	Confinement	Sinuosity
Reach 1	8	Moderate	Confine	Moderate
Reach 2	8	Moderate	Unconfine	High

East Branch Little Forks Stream

	Soil lithology	Gradient	Confinement	Sinuosity
Reach 1	9	Moderate	Confine	Moderate
Reach 2	9	Moderate	Unconfine	High

Little Forks Stream

	Soil lithology	Gradient	Confinement	Sinuosity
Reach1	9	Moderate	Unconfine	Moderate
Reach 2	9	Moderate	Confine	High
Reach 3	9	Low	Unconfine	Moderate

Pleasant Brook

	Soil lithology	Gradient	Confinement	Sinuosity
Reach1	9	Moderate	Unconfine	High
Reach2	8	Moderate	Confine	High

Coal Creek

	Soil lithology	Gradient	Confinement	Sinuosity
Reach 1	9	Moderate	Confine	Moderate
Reach 2	1	low	Confine	Moderate

Newcastle Creek

	Soil lithology	Gradient	Confinement	Sinuosity
Reach1	8	Moderate	Unconfine	High
Reach2	8	Moderate	Confine	High
Reach3	1	Moderate	Unconfine	High

Canaan River

	Soil lithology	Gradient	Confinement	Sinuosity
Reach 1	9	Moderate	Unconfine	Moderate
Reach 2	9	Moderate	Confine	Moderate
Reach 3	1	Low	Unconfine	Moderate
Reach 4	9	Low	Confine	Moderate
Reach 5	1	Low	Unconfine	Moderate

Forks Stream

	Soil lithology	Gradient	Confinement	Sinuosity
Reach 1	9	Moderate	Confine	Moderate
Reach 2	1	Moderate	Unconfine	High
Reach 3	9	Moderate	Confine	Moderate

Lower North Branch Canaan River

	Soil lithology	Gradient	Confinement	Sinuosity
Reach 1	9	Moderate	Unconfine	High

Ridge Brook

	Soil lithology	Gradient	Confinement	Sinuosity
Reach 1	9	Moderate	confine	High
Reach 2	11	Moderate	Un	High
Reach 3	1	Moderate	un	High

Thornes Brook

	Soil lithology	Gradient	Confinement	Sinuosity
Reach 1	9	Moderate	Unconfine	High
Reach 2	9	Moderate	Confine	High
Reach 3	9	High	Unconfine	High

Miller Brook

	Soil lithology	Gradient	Confinement	Sinuosity
Reach 1	9	Low	Unconfine	High
Reach 2	9	High	Unconfine	High

Long Creek

	Soil lithology	Gradient	Confinement	Sinuosity
Reach 1	9	Moderate	Unconfine	High
Reach 2	8	Moderate	Unconfine	Moderate
Reach 3	9	Low	Unconfine	Moderate

Salmon Creek

	Soil lithology	Gradient	Confinement	Sinuosity
Reach 1	9	Moderate	Unconfine	Moderate

Kennebecasis River

	Soil lithology	Gradient	Confinement	Sinuosity
Reach 1	1	Moderate	Confine	Moderate
Reach 2	1	Low	Unconfine	High
Reach 3	1	Low	Confine	Moderate
Reach 4	1	Low	Unconfine	Moderate
Reach 5	5 and 11	Low	Confine	Moderate

Smith's Creek

	Soil lithology	Gradient	Confinement	Sinuosity
Reach 1	1	Low	Unconfine	High
Reach 2	11	Moderate	Confine	Moderate
Reach 3	1	Low	Unconfine	High
Reach 4	11	Low	Unconfine	High

Millstream River

	Soil lithology	Gradient	Confinement	Sinuosity
Reach 1	11	Moderate	Unconfine	High
Reach 2	1	Low	Unconfine	High

Trout Creek

	Soil lithology	Gradient	Confinement	Sinuosity
Reach 1	11	Moderate	Unconfine	Moderate
Reach 2	11	Moderate	Confine	Moderate
Reach 3	11	Moderate	Unconfine	Moderate

Wards Creek

	Soil lithology	Gradient	Confinement	Sinuosity
Reach 1	11	Moderate	Unconfine	Moderate
Reach 2	1	Moderate	Unconfine	Moderate
Reach 3	11	Moderate	Unconfine	High

Hammond River

	Soil lithology	Gradient	Confinement	Sinuosity
Reach 1	1	Moderate	Unconfine	Moderate
Reach2	11and 4	Low	Unconfine	Moderate
Reach 3	11 and 6	Moderate	Confine	Moderate
Reach 4	11 and 5	Moderate	Confine	Moderate
Reach 5	11	Low	Confine	Moderate
Reach 6	1	Low	Unconfine	Moderate

Nerepis River

	Soil lithology	Gradient	Confinement	Sinuosity
Reach 1	11	Moderate	Unconfine	Moderate
Reach2	7	Moderate	Unconfine	Moderate
Reach3	13	Moderate	Confine	Moderate
Reach4	1	Moderate	Unconfine	Moderate
Reach5	4	Moderate	Confine	Moderate
Reach6	1	Low	Unconfine	High
Reach7	5 and 3	Moderate	Confine	Moderate
Reach 8	5	Moderate	Unconfine	Moderate
Reach 9	4 and 1	Low	Unconfine	Moderate

Burpee Millstream

	Soil lithology	Gradient	Confinement	Sinuosity
Reach 1	8	Moderate	Unconfine	High
Reach 2	9	Moderate	Unconfine	High
Reach 3	8	Moderate	Unconfine	High

Noonan Stream

	Soil lithology	Gradient	Confinement	Sinuosity
Reach 1	8	Moderate	Unconfine	High
Reach 2	1	Moderate	Unconfine	High
Reach 3	1	Low	Unconfine	high

Coal Creek

	Soil lithology	Gradient	Confinement	Sinuosity
Reach1	9	Moderate	Unconfine	Moderate
Reach 2	9	Moderate	Confine	Moderate
Reach 3	1	low	Confine	Moderate

Otnabog Stream

	Soil lithology	Gradient	Confinement	Sinuosity
Reach1	9	Moderate	Unconfine	High
Reach2	9	Moderate	Confine	Moderate
Reach3	8	Moderate	Confine	High
Reach4	8	Moderate	Unconfine	High
Reach5	1	Low	Unconfine	Moderate

Jones Creek

	Soil lithology	Gradient	Confinement	Sinuosity
Reach 1	4	Moderate	Unconfine	Moderate
Reach 2	3	Moderate	Unconfine	High
Reach 3	4	Moderate	Unconfine	High
Reach 4	10	Moderate	Unconfine	High

Cumberland Bay Stream

	Soil lithology	Gradient	Confinement	Sinuosity
Reach 1	9	Moderate	Unconfine	Moderate
Reach 2	9 and 8	Moderate	Unconfine	Moderate

Wasson Brook

	Soil lithology	Gradient	Confinement	Sinuosity
Reach 1	9	Moderate	Unconfine	High

Youngs Creek

	Soil lithology	Gradient	Confinement	Sinuosity
Reach 1	9	Moderate	Unconfine	High
Reach 2	1	Low	Unconfine	High

South Branch

	Soil lithology	Gradient	Confinement	Sinuosity
Reach 1	1	Moderate	Unconfine	Moderate
Reach 2	1	Moderate	Unconfine	High

Parlee Brook

	Soil lithology	Gradient	Confinement	Sinuosity
Reach1	11	Moderate	Unconfine	Moderate

Mill Brook

	Soil lithology	Gradient	Confinement	Sinuosity
Reach 1	11	Moderate	Confine	Moderate
Reach 2	11	Moderate	Unconfine	High

Musquash Brook

	Soil lithology	Gradient	Confinement	Sinuosity
Reach1	12	Moderate	Unconfine	High
Reach 2	11	Moderate	Unconfine	High

Almshouse Brook

	Soil lithology	Gradient	Confinement	Sinuosity
Reach 1	1	Moderate	confine	Moderate
Reach 2	1	Moderate	Unconfine	Moderate
Reach 3	11	Moderate	Unconfine	Moderate

Moosehorn Creek

	Soil lithology	Gradient	Confinement	Sinuosity
Reach 1	11	Moderate	Unconfine	Moderate
Reach 2	12	Moderate	Unconfine	Moderate
Reach 3	12	High	Confine	Moderate
Reach 4	12	High	Unconfine	High

Pascobac Brook

	Soil lithology	Gradient	Confinement	Sinuosity
Reach1	11	Moderate	Unconfine	High

Belleisle Creek

	Soil lithology	Gradient	Confinement	Sinuosity
Reach 1	11	Moderate	Unconfine	Moderate
Reach 2	1	Low	Unconfine	High

Midland Brook

	Soil lithology	Gradient	Confinement	Sinuosity
Reach 1	11	Moderate	Unconfine	High

Sucker Brook

	Soil lithology	Gradient	Confinement	Sinuosity
Reach1	7	Moderate	Unconfine	High
Reach 2	7	Moderate	Confine	High

River George

	Soil lithology	Gradient	Confinement	Sinuosity
Reach 1	11	Moderate	Unconfine	Moderate
Reach 2	11	Moderate	Confine	Moderate
Reach 3	11	Moderate	Unconfine	High
Reach 4	11	Moderate	Confine	Moderate
Reach 5	7	Moderate	Confine	High

Kerr Brook

	Soil lithology	Gradient	Confinement	Sinuosity
Reach 1	13	Moderate	Unconfine	High
Reach 1	13	Moderate	Unconfine	Moderate
Reach 2	11	Moderate	Unconfine	High

Queens Brook

	Soil lithology	Gradient	Confinement	Sinuosity
Reach 1	4	Moderate	Confine	Moderate
Reach 2	7	Moderate	Unconfine	Moderate
Reach 3	4	Moderate	Unconfine	Moderate

Saint John River

	Soil lithology	Gradient	Confinement	Sinuosity
Reach 1	1 and 8	Low	Confine	Low
Reach 2	1	Low	Unconfine	Low
Reach 3	10 and 4	Low	Confine	Low
Reach4	3 and 4	Low	Confine	Low
Reach 5	4 and 5	Low	Confine	Low
Reach 6	4 and 7	Low	Confine	Low
Reach 7	5	Low	Confine	Low
Reach 8	3 and 11	Low	Confine	Low
Reach 9	13	Low	Confine	Low
Reach 10	4 and 5	Low	Confine	Low

Flaglor Brook

	Soil lithology	Gradient	Confinement	Sinuosity
Reach 1	4 and 1	Low	Unconfine	Moderate
Reach 2	3	Moderate	Unconfine	Moderate
Reach 3	3	Moderate	Confine	High
Reach 4	4	Moderate	Confine	Moderate
Reach 5	4	Moderate	Unconfine	High

Swan Creek

	Soil lithology	Gradient	Confinement	Sinuosity
Reach 1	9	Moderate	Unconfine	High

Rathburn Brook

	Soil lithology	Gradient	Confinement	Sinuosity
Reach 1	11	Moderate	Unconfine	Moderate
Reach 2	11	Moderate	Confine	High
Reach 3	1	Moderate	Unconfine	Moderate

Marsh Creek

	Soil lithology	Gradient	Confinement	Sinuosity
Reach 1	5	Low	Unconfine	Moderate
Reach 2	4	Low	Unconfine	Moderate
Reach 3	5	Low	Unconfine	Moderate

Windgap Brook

	Soil lithology	Gradient	Confinement	Sinuosity
Reach 1	11	Moderate	Unconfine	Moderate
Reach 2	1	Moderate	Unconfine	High

Mill Brook 2

	Soil lithology	gradient	Confinement	Sinuosity
Reach 1	9	Moderate	Confine	Moderate
Reach 2	9	Moderate	Unconfine	Moderate
Reach 3	1	Low	Unconfine	Moderate

North Branch Hammond River

	Soil lithology	Gradient	Confinement	Sinuosity
Reach 1	11	Moderate	Unconfine	High
Reach 2	1	Moderate	Unconfine	Moderate

Hanford Brook

	Soil lithology	Gradient	Confinement	Sinuosity
Reach 1	5	High	Confine	High
Reach 2	4	High	Confine	High
Reach 3	4	Moderate	Unconfine	High

Big Brook

	Soil lithology	Gradient	Confinement	Sinuosity
Reach 1	1	Moderate	Unconfine	Moderate
Reach 2	8	Moderate	Unconfine	Moderate
Reach 3	8	High	Unconfine	High

Kelly Brook

	Soil lithology	Gradient	Confinement	Sinuosity
Reach 1	9	Moderate	Unconfine	High

Porcupine Brook

	Soil lithology	Gradient	Confinement	Sinuosity
Reach 1	9	Moderate	Unconfine	High

Southbranch Miller Brook

	Soil lithology	Gradient	Confinement	Sinuosity
Reach 1	9	Moderate	Confine	High
Reach 2	9	Moderate	Unconfine	Moderate
Reach 3	9	Moderate	confine	high

Sharpe Brook

	Soil lithology	Gradient	Confinement	Sinuosity
Reach 1	1	Moderate	Unconfine	High
Reach 1	1	Low	Unconfine	High

Peters Brook

	Soil lithology	Gradient	confinement	Sinuosity
Reach 1	5	Moderate	Unconfine	High

Baltimore Stream

	Soil lithology	Gradient	Confinement	Sinuosity
Reach 1	9	Moderate	Unconfine	High
Reach 2	1	Moderate	Unconfine	Moderate

Dingee Millstream

	Soil lithology	Gradient	Confinement	Sinuosity
Reach 1	9	Moderate	Unconfine	high

Elm Stream

	Soil lithology	Gradient	Confinement	Sinuosity
Reach 1	9	Moderate	Unconfine	High

Brown Brook

	Soil lithology	Gradient	Confinement	Sinuosity
Reach 1	9	Moderate	Confine	Moderate
Reach 2	9	Moderate	Unconfine	Moderate
Reach 3	8	Moderate	Confine	Moderate
Reach 4	8	Moderate	Unconfine	Moderate

Patterson Brook

	Soil lithology	Gradient	Confinement	Sinuosity
Reach 1	10	Moderate	Confine	Moderate
Reach 2	1	Moderate	Unconfine	High

North Brook

	Soil lithology	Gradient	Confinement	Sinuosity
Reach 1	8	Moderate	Unconfine	High

Shaw Creek

	Soil lithology	Gradient	Confinement	Sinuosity
Reach 1	1	Low	Unconfine	High

Dunn Brook

	Soil lithology	Gradient	Confinement	Sinuosity
Reach 1	7	Moderate	Unconfine	High

Little River 2

	Soil lithology	Gradient	Confinement	Sinuosity
Reach 1	1	Low	Unconfine	Moderate
Reach 2	1 and 4	Low	Unconfine	Moderate

Bass Creek

	Soil lithology	Gradient	Confinement	Sinuosity
Reach 1	1	Low	Unconfine	Moderate

Salmon Creek 2

	Soil lithology	Gradient	Confinement	Sinuosity
Reach 1	8	Moderate	Unconfine	High
Reach 2	1	Moderate	Unconfine	High

Jemseg River

	Soil lithology	Gradient	Confinement	Sinuosity
Reach 1	1	Low	Unconfine	Moderate

Sucker Brook 2

	Soil lithology	Gradient	Confinement	Sinuosity
Reach 1	9	Moderate	Unconfine	High

Baker Brook

	Soil lithology	Gradient	Confinement	Sinuosity
Reach 1	8	Low	Unconfine	Moderate
Reach 2	1	Low	Unconfine	High

Passekeag Creek

	Soil lithology	Gradient	Confinement	Sinuosity
Reach 1	1	Moderate	Unconfine	High
Reach 2	1	Low	Unconfine	High

Pickwauket Brook

	Soil lithology	Gradient	Confinement	Sinuosity
Reach 1	11	Low	Unconfine	High
Reach 2	1	Moderate	Unconfine	High

Kennebec Brook

	Soil lithology	Gradient	Confinement	Sinuosity
Reach 1	12	Moderate	Unconfine	High
Reach 2	11	Moderate	Unconfine	High

Quinn Brook

	Soil lithology	Gradient	Confinement	Sinuosity
Reach 1	11	Moderate	Unconfine	Moderate
Reach 2	11	Moderate	Unconfine	High

Table C.2a: Soil Lithology Legend (Miramichi River Basin Watershed)

1. Undifferentiated
2. Red mudstones (weathered)
3. Gneiss, granites, alkali granites, granodiorites and/or quartz diorites
4. Metasedimentary rocks mixed with igneous rocks
5. Calcareous siltstones, calcareous sandstones and/or calcareous slates
6. Igneous rocks mixed with metasedimentary rocks
7. Grey lithic-feldsapthic sandstones
8. Metaquartzites, slates, metasiltstones, metasandstones, metaconglomerates and/or metawackes
9. Felsic volcanic or mixed igneous rocks and/or felsic pebble conglomerates
10. Mafic volcanic rocks, gabbro and/or diorites
11. Red polymictic conglomerates, feldspathic to lithic sandstones and/or mud stones
12. Grey-red sandstones or mudstones mixed with igneous rocks

Table C.2b: River reaches information

Elliott Brook

	Soil lithology	Gradient	Confinement	Sinuosity
Reach1	8	Moderate	Unconfine	High

Lake Brook

	Soil lithology	Gradient	Confinement	Sinuosity
Reach 1	5	Moderate	Unconfine	High
Reach2	8	Moderate	Unconfine	High

South Branch Southwest Miramichi River

	Soil lithology	Gradient	Confinement	Sinuosity
Reach 1	1	Moderate	Unconfine	High
Reach 2	8	Moderate	Unconfine	High
Reach 3	9	Moderate	Unconfine	High
Reach 4	1	Low	Unconfine	High

Big Teague Brook

	Soil lithology	Gradient	Confinement	Sinuosity
Reach 1	8	Moderate	Unconfine	High

North Branch Southwest Miramichi River

	Soil lithology	Gradient	Confinement	Sinuosity
Reach 1	10	Moderate	Unconfine	High
Reach 2	4	Moderate	Confine	High
Reach 3	9	Moderate	Unconfine	High
Reach 4	1	Low	Unconfine	High
Reach 5	9	Low	Unconfine	High

Beadle Brook

	Soil lithology	Gradient	Confinement	Sinuosity
Reach 1	3	Moderate	Unconfine	High
Reach 2	9	High	Unconfine	High
Reach 3	3	Low	Unconfine	High
Reach 4	1	Low	Unconfine	High

McKiel Brook

	Soil lithology	Gradient	Confinement	Sinuosity
Reach 1	3	High	Unconfine	High
Reach 2	9	Moderate	Unconfine	High
Reach 3	3	Moderate	Unconfine	High

Southwest Miramichi River

	Soil lithology	Gradient	Confinement	Sinuosity
Reach 1	9	Low	Unconfine	Moderate
Reach 2	3	Moderate	Unconfine	High
Reach 3	4	Moderate	Confine	Moderate
Reach 4	6	Moderate	Confine	Moderate
Reach 5	4	Moderate	Confine	Moderate
Reach 6	5	Moderate	Confine	Moderate
Reach 7	7	Moderate	Confine	Moderate
Reach 8	1	Low	Confine	Moderate
Reach 9	7	Low	Confine	Moderate
Reach 10	2	Low	Confine	Low

Burnthill Brook

	Soil lithology	Gradient	Confinement	Sinuosity
Reach 1	9	Moderate	Unconfine	High
Reach 2	3	Moderate	Unconfine	High
Reach 3	4	Moderate	Confine	mo

North Branch Burnthill Brook

	Soil lithology	Gradient	Confinement	Sinuosity
Reach 1	9	High	Unconfine	High
Reach 2	3	High	Unconfine	High
Reach 3	9	High	Unconfine	High

South Branch Burnthill Brook

	Soil lithology	Gradient	Confinement	Sinuosity
Reach 1	3	Moderate	Unconfine	High

Beaver Brook

	Soil lithology	Gradient	Confinement	Sinuosity
Reach 1	3	Moderate	Unconfine	High

Clearwater Brook

	Soil lithology	Gradient	Confinement	Sinuosity
Reach 1	3	Moderate	Unconfine	High
Reach 2	10	Moderate	Unconfine	High
Reach 3	3	Moderate	Confine	Moderate
Reach 4	4	Moderate	Confine	Moderate

Little Northeast Branch Clearwater Brook

	Soil lithology	Gradient	Confinement	Sinuosity
Reach1	3	High	Unconfine	High

Northeast Branch Clearwater Brook

	Soil lithology	Gradient	Confinement	Sinuosity
Reach 1	10	High	Unconfine	High
Reach 2	3	High	Unconfine	Moderate

Lake Brook 2

	Soil lithology	Gradient	Confinement	Sinuosity
Reach 1	3	High	Unconfine	High
Reach 3	10	High	Unconfine	High

Sisters Brook

	Soil lithology	Gradient	Confinement	Sinuosity
Reach 1	9	High	Unconfine	High
Reach 2	4	High	Confine	High

Rocky Brook

	Soil lithology	Gradient	Confinement	Sinuosity
Reach 1	3	High	Unconfine	High
Reach 2	9	Moderate	Unconfine	Moderate
Reach 3	10	High	Confine	Moderate
Reach 4	9	High	Confine	High

Gulch Brook

	Soil lithology	Gradient	Confinement	Sinuosity
Reach 1	3	Moderate	Unconfine	Moderate

Trout Brook

	Soil lithology	Gradient	Confinement	Sinuosity
Reach 1	6	High	Unconfine	High
Reach 2	1	Moderate	Unconfine	High
Reach 3	4	High	Unconfine	Moderate
Reach 4	8	High	Confine	Moderate
Reach 5	4	High	Confine	Moderate

McBean Brook

	Soil lithology	Gradient	Confinement	Sinuosity
Reach 1	5	High	Unconfine	High

Salmon Brook

	Soil lithology	Gradient	Confinement	Sinuosity
Reach 1	5	High	Confine	High

Porter Brook

	Soil lithology	Gradient	Confinement	Sinuosity
Reach 1	7	Moderate	Confine	High

Taxis River

	Soil lithology	Gradient	Confinement	Sinuosity
Reach 1	8 and 5	Moderate	Unconfine	High
Reach 2	5	Moderate	Confine	Moderate
Reach 3	9	Moderate	Confine	Moderate

South Branch Taxis River

	Soil lithology	Gradient	Confinement	Sinuosity
Reach 1	8	Moderate	Unconfine	High

Jewett Brook

	Soil lithology	Gradient	Confinement	Sinuosity
Reach 1	5	High	Unconfine	Moderate

Hovey Brook

	Soil lithology	Gradient	Confinement	Sinuosity
Reach 1	5	High	Unconfine	High

Burnt Land Brook

	Soil lithology	Gradient	Confinement	Sinuosity
Reach 1	7	Moderate	Unconfine	High
Reach 2	7	Moderate	Confine	High

West Branch Burntland Brook

	Soil lithology	Gradient	Confinement	Sinuosity
Reach 1	7	Moderate	Confine	High

Big Hole Brook

	Soil lithology	Gradient	Confinement	Sinuosity
Reach 1	7	Moderate	Confine	High
Reach 2	7	Moderate	Unconfine	High

Cains River

	Soil lithology	Gradient	Confinement	Sinuosity
Reach 1	7	Moderate	Unconfine	High
Reach 2	1	Moderate	Unconfine	High
Reach 3	7	Moderate	Confine	High
Reach 4	7	Moderate	Unconfine	Moderate
Reach 5	7	Low	Confine	Moderate

Muzroll Brook

	Soil lithology	Gradient	Confinement	Sinuosity
Reach 1	7	Moderate	Confine	High

Six Mile Brook

	Soil lithology	Gradient	Confinement	Sinuosity
Reach 1	2	Moderate	Unconfine	High
Reach 2	2	Moderate	Confine	High

East Branch Six-Mile Brook

	Soil lithology	Gradient	Confinement	Sinuosity
Reach 1	2	Moderate	Confine	High

East Branch Sabbies River

	Soil lithology	Gradient	Confinement	Sinuosity
Reach 1	2	Moderate	Unconfine	High
Reach 2	2	Moderate	Confine	High
Reach 3	7	Moderate	Confine	High

Sabbies River

	Soil lithology	Gradient	Confinement	Sinuosity
Reach1	7	Moderate	Confine	High

Black Brook

	Soil lithology	Gradient	Confinement	Sinuosity
Reach 1	7	Moderate	Unconfine	High
Reach 2	7	Low	Unconfine	High
Reach 3	7	Moderate	Confine	High

Bartholomew River

	Soil lithology	Gradient	Confinement	Sinuosity
Reach 1	7	Moderate	Unconfine	High
Reach 2	7	Moderate	Confine	High
Reach 3	7	Moderate	Unconfine	High
Reach 4	7	Low	Confine	High

South Branch Bartholomew River

	Soil lithology	Gradient	Confinement	Sinuosity
Reach 1	7	Moderate	Unconfine	Moderate

Dungarvon River

	Soil lithology	Gradient	Confinement	Sinuosity
Reach 1	3	Moderate	Unconfine	High
Reach 2	4	Moderate	Confine	Moderate
Reach 3	5	Moderate	Confine	Moderate
Reach4	7	Moderate	Unconfine	Moderate

South Branch Dungarvon River

	Soil lithology	Gradient	Confinement	Sinuosity
Reach 1	3	High	Unconfine	High

Little Dungarvon River

	Soil lithology	Gradient	Confinement	Sinuosity
Reach 1	1	Moderate	Unconfine	High
Reach 2	4	Moderate	Unconfine	Moderate

South Branch Renous River

	Soil lithology	Gradient	Confinement	Sinuosity
Reach 1	3	Moderate	Unconfine	High
Reach 2	6	High	Unconfine	High
Reach 3	8	Moderate	Unconfine	High
Reach 4	8	Moderate	Confine	High
Reach 5	5	Moderate	Confine	High
Reach 6	11	Moderate	Unconfine	High
Reach 7	7	Moderate	Unconfine	High

Renous River

	Soil lithology	Gradient	Confinement	Sinuosity
Reach 1	8	Moderate	Unconfine	Moderate
Reach 2	7	Moderate	Unconfine	High
Reach 3	7	Low	Confine	Moderate

North Branch Renous River

	Soil lithology	Gradient	Confinement	Sinuosity
Reach 1	4	Moderate	Unconfine	High
Reach 2	4	Moderate	Confine	Moderate
Reach 3	8	Moderate	Confine	High

Little Ottawa Branch

	Soil lithology	Gradient	Confinement	Sinuosity
Reach 1	9	Moderate	Unconfine	High
Reach 2	6	High	Confine	Moderate

Lake Brook 3

	Soil lithology	Gradient	Confinement	Sinuosity
Reach 1	9	High	Unconfine	High

Little Southwest Miramichi River

	Soil lithology	Gradient	Confinement	Sinuosity
Reach 1	3	Low	Unconfine	High
Reach 2	9	Low	Unconfine	Moderate
Reach 3	3	Moderate	Confine	Moderate
Reach 4	4	Moderate	Confine	High
Reach 5	9	Moderate	Confine	High
Reach 6	6	Moderate	Confine	High
Reach 7	9	Moderate	Confine	Moderate
Reach 8	9	Moderate	Unconfine	Moderate

North Pole Stream

	Soil lithology	Gradient	Confinement	Sinuosity
Reach 1	3	High	Unconfine	High
Reach 2	9	Moderate	Unconfine	High
Reach 3	9	Moderate	Confine	High
Reach 4	9	Moderate	Unconfine	High
Reach 5	3	Moderate	Unconfine	High

West Branch Little Southwest Miramichi River

	Soil lithology	Gradient	Confinement	Sinuosity
Reach 1	9	Moderate	Unconfine	High

Lower North Branch Little Southwest Miramichi River

	Soil lithology	Gradient	Confinement	Sinuosity
Reach 1	3	Moderate	Unconfine	High
Reach 2	6	Moderate	Unconfine	High
Reach 3	9	Moderate	Unconfine	High
Reach 4	6	Moderate	Confine	Moderate
Reach 5	4	Low	Unconfine	High
Reach 6	6	Moderate	Confine	High
Reach 7	9	High	Confine	High

Fish Brook

	Soil lithology	Gradient	Confinement	Sinuosity
Reach 1	3	High	Unconfine	Moderate
Reach 2	3	Moderate	Unconfine	High
Reach 3	3	High	Unconfine	High

Tuadook River

	Soil lithology	Gradient	Confinement	Sinuosity
Reach 1	6	Low	Unconfine	High
Reach 2	3	Moderate	Unconfine	High

Crooked Brook

	Soil lithology	Gradient	Confinement	Sinuosity
Reach 1	3	High	Unconfine	High
Reach 2	3	Moderate	Unconfine	High

Little Sevogle River

	Soil lithology	Gradient	Confinement	Sinuosity
Reach 1	4	Moderate	Confine	High
Reach 2	10	Moderate	Confine	High
Reach 3	6	Moderate	Unconfine	High
Reach 4	11	Moderate	Unconfine	High
Reach 5	7	Moderate	Confine	High
Reach 6	9	Moderate	Unconfine	High

South Branch Big Sevogle River

	Soil lithology	Gradient	Confinement	Sinuosity
Reach 1	3	High	Unconfine	High
Reach 2	4	Moderate	Unconfine	High
Reach 3	4	Moderate	Confine	High
Reach 4	3	Moderate	Confine	High
Reach 5	4	Moderate	Confine	High

Mullin Stream

	Soil lithology	Gradient	Confinement	Sinuosity
Reach 1	4	Moderate	Unconfine	High
Reach 2	4	Moderate	Confine	High

North Branch Big Sevogle River

	Soil lithology	Gradient	Confinement	Sinuosity
Reach 1	10	Moderate	Unconfine	High
Reach 2	9	Moderate	Unconfine	High
Reach 3	4	Moderate	Confine	High

Big Sevogle River

	Soil lithology	Gradient	Confinement	Sinuosity
Reach 1	9	Moderate	Confine	High

Northwest Miramichi River

	Soil lithology	Gradient	Confinement	Sinuosity
Reach 1	9	Moderate	Unconfine	High
Reach 2	9	Moderate	Confine	High
Reach 3	4	Moderate	Confine	High
Reach 4	4	Moderate	Unconfine	High
Reach 5	8	Moderate	Unconfine	Moderate
Reach 6	11	Moderate	Unconfine	Moderate
Reach 7	9	Low	Confine	Moderate
Reach 8	2 and 7	Low	Confine	Moderate

Little River

	Soil lithology	Gradient	Confinement	Sinuosity
Reach	6	Moderate	Unconfine	High
Reach	10	Moderate	Unconfine	High
Reach	6	Moderate	Unconfine	High
Reach	10	Moderate	Unconfine	High
Reach	4	Moderate	Unconfine	High

Mountain Brook

	Soil lithology	Gradient	Confinement	Sinuosity
Reach 1	9	High	Confine	High
Reach 2	6	High	Confine	Moderate

Little South Branch Tomogonops River

	Soil lithology	Gradient	Confinement	Sinuosity
Reach 1	9	High	Unconfine	High
Reach 2	6	High	Unconfine	High

North Branch Tomogonops River

	Soil lithology	Gradient	Confinement	Sinuosity
Reach 1	6	Moderate	Confine	Moderate
Reach 2	10	Moderate	Confine	Moderate
Reach 3	9	High	Confine	High

Tomogonops River

	Soil lithology	Gradient	Confinement	Sinuosity
Reach 1	9	Moderate	Confine	Moderate
Reach 2	4	Moderate	Unconfine	High

East Branch Portage River

	Soil lithology	Gradient	Confinement	Sinuosity
Reach 1	11	Moderate	Unconfine	High
Reach 2	4	Moderate	Unconfine	High
Reach 3	4	Low	Unconfine	High
Reach 4	2	Low	Unconfine	High
Reach 5	2	Moderate	Unconfine	High

Portage River

	Soil lithology	Gradient	Confinement	Sinuosity
Reach 1	4	Moderate	Unconfine	High

Wildcat Brook

	Soil lithology	Gradient	Confinement	Sinuosity
Reach 1	2	Moderate	Unconfine	High
Reach 2	9	Moderate	Unconfine	High
Reach 3	9	Low	Unconfine	High

North West Millstream

	Soil lithology	Gradient	Confinement	Sinuosity
Reach 1	2	Moderate	Confine	High

Barnaby River

	Soil lithology	Gradient	Confinement	Sinuosity
Reach 1	7	Moderate	Unconfine	High
Reach 2	2	Low	Unconfine	High
Reach 3	9	Low	Unconfine	High
Reach 4	11	Moderate	Unconfine	High
Reach 5	12	Low	Confine	High
Reach 6	1	Low	Confine	High
Reach 7	11	Low	Confine	High

Middle Branch Barnaby River

	Soil lithology	Gradient	Confinement	Sinuosity
Reach 1	7	Moderate	Unconfine	High

Saunders Brook

	Soil lithology	Gradient	Confinement	Sinuosity
Reach 1	2	Moderate	Unconfine	High
Reach 2	11	Moderate	Unconfine	High

Miramichi River

	Soil lithology	Gradient	Confinement	Sinuosity
Reach 1	7	Low	Confine	Moderate

No Name River

	Soil lithology	Gradient	Confinement	Sinuosity
Reach 1	6	Moderate	Unconfine	High
Reach 2	9	Moderate	Unconfine	High
Reach 3	6	Moderate	Unconfine	High
Reach 4	1	Low	Unconfine	High

Lake Brook

	Soil lithology	Gradient	Confinement	Sinuosity
Reach 1	6	Moderate	Unconfine	High
Reach 2	3	Low	Unconfine	High

Libbies Brook

	Soil lithology	Gradient	Confinement	Sinuosity
Reach 1	4	High	Unconfine	High
Reach 2	4	High	Confine	High
Reach 3	9	High	Confine	High

Appendix D. Confusion Matrix for Different ARA Delineation

Table D.1 Lower St. John River Watershed

D.1a: 30-m SRTM DEM and 1:50,000 NHN derived ARA

ARA components	Open water	Floodplain (non-wet)	Terraces (non-wet)	60-m Buffer	Steep slope	Riparian wetland	Flood plain (wet)	Terraces (wet)	Non-ARA	Total	U_Accuracy	Kappa
Openwater	29	3	0	0	5	3	7	0	1	48	0.6041	0
Floodplain (non-wet)	8	9	3	5	4	9	56	6	14	114	0.0789	0
Terraces (non-wet)	0	0	0	0	0	0	0	0	0	0	0	0
60-m Buffer	0	0	1	4	5	0	2	0	4	16	0.25	0
Steep slope	0	1	0	2	16	0	0	0	2	21	0.7619	0
Riparian wetland	1	0	0	1	0	10	11	1	20	44	0.2273	0
Floodplain (wet)	0	0	0	0	0	0	0	0	0	0	0	0
Terraces (wet)	0	0	0	0	0	0	0	0	0	0	0	0
Non-ARA	9	1	2	9	47	45	28	7	609	757	0.8045	0
Total	47	14	6	21	77	67	104	14	650	1000	0	0
P_Accuracy	0.6170	0.6429	0	0.1905	0.2078	0.1493	0	0	0.9369	0	0.677	0
Kappa	0	0	0	0	0	0	0	0	0	0	0	0.3530

D.1b: 30-m SRTM DEM and 1:10,000 NBHN derived ARA

ARA components	Open water	Floodplain (non-wet)	Terraces (non-wet)	60-m Buffer	Steep slope	Riparian wetland	Floodplain (wet)	Terraces (wet)	Non-ARA	Total	U_Accuracy	Kappa
Openwater	45	6	0	0	8	1	22	0	0	82	0.54878	0
Floodplain (non-wet)	1	7	3	0	0	4	16	2	3	36	0.194444	0
Terraces (non-wet)	0	0	0	0	0	0	0	0	0	0	0	0
60-m Buffer	0	0	0	7	5	0	4	0	6	22	0.318182	0
Steep slope	0	0	0	1	27	0	0	0	4	32	0.84375	0
Riparian wetland	0	0	1	2	2	17	8	4	14	48	0.354167	0
Floodplain (wet)	1	1	1	8	5	9	29	3	3	60	0.483333	0
Terraces (wet)	0	0	0	0	0	0	0	0	0	0	0	0
Non-ARA	0	0	1	3	30	36	25	5	620	720	0.861111	0
Total	47	14	6	21	77	67	104	14	650	1000	0	0
P_Accuracy	0.9574	0.5	0	0.3333	0.3506	0.2537	0.2788	0	0.9538	0	0.752	0
Kappa	0	0	0	0	0	0	0	0	0	0	0	0.5187

D.1c: 30-m LiDAR DEM and 1:10,000 NBHN derived ARA

ARA components	Open water	Floodplain (non-wet)	Terraces (non-wet)	60-m Buffer	Steep slope	Riparian wetland	Floodplain (wet)	Terraces (wet)	Non-ARA	Total	U_Accuracy	Kappa
Openwater	45	5	0	0	8	3	16	0	0	77	0.5844	0
Floodplain (non-wet)	0	5	6	3	0	11	26	8	7	66	0.0758	0
Terraces (non-wet)	0	0	0	0	0	0	0	0	0	0	0	0
60-m Buffer	0	0	0	6	7	1	0	0	15	29	0.2069	0
Steep slope	0	0	0	3	40	0	0	0	5	48	0.8333	0
Riparian wetland	0	1	0	4	0	22	2	0	30	59	0.3729	0
Floodplain (wet)	2	3	0	5	0	14	60	6	1	91	0.6593	0
Terraces (wet)	0	0	0	0	0	0	0	0	0	0	0	0
Non-ARA	0	0	0	0	22	16	0	0	592	630	0.9397	0
Total	47	14	6	21	77	67	104	14	650	1000	0	0
P_Accuracy	0.9574	0.3571	0	0.2857	0.5195	0.3284	0.5769	0	0.911	0	0.77	0
Kappa	0	0	0	0	0	0	0	0	0	0	0	0.5952

D.1d: 15-m LiDAR DEM and 1:10,000 NBHN derived ARA

ARA components	Open water	Floodplain (non-wet)	Terraces (non-wet)	60-m Buffer	Steep slope	Riparian wetland	Floodplain (wet)	Terraces (wet)	Non-ARA	Total	U_Accuracy	Kappa
Openwater	45	2	0	0	3	1	6	0	0	57	0.7895	0
Floodplain (non-wet)	1	6	6	4	2	10	16	8	6	59	0.1017	0
Terraces (non-wet)	0	0	0	0	0	0	0	0	0	0	0	0
60-m Buffer	0	0	0	10	3	2	0	0	3	18	0.5556	0
Steep slope	0	0	0	0	42	0	0	0	3	45	0.9333	0
Riparian wetland	0	1	0	5	4	16	0	0	42	68	0.2353	0
Floodplain (wet)	1	5	0	2	0	29	82	6	12	137	0.5985	0
Terraces (wet)	0	0	0	0	0	0	0	0	0	0	0	0
Non-ARA	0	0	0	0	23	9	0	0	584	616	0.9481	0
Total	47	14	6	21	77	67	104	14	650	1000	0	0
P_Accuracy	0.9574	0.4286	0	0.4761	0.5455	0.2388	0.7885	0	0.8985	0	0.785	0
Kappa	0	0	0	0	0	0	0	0	0	0	0	0.6251

D.1e: 10-m LiDAR DEM and 1:10,000 NBHN derived ARA

ARA components	Open water	Floodplain (non-wet)	Terraces (non-wet)	60-m Buffer	Steep slope	Riparian wetland	Floodplain (wet)	Terraces (wet)	Non-ARA	Total	U_Accuracy	Kappa
Openwater	46	3	0	0	3	0	6	0	0	58	0.7931	0
Floodplain (non-wet)	0	7	5	2	0	4	12	6	3	39	0.1795	0
Terraces (non-wet)	0	0	0	0	0	0	0	0	0	0	0	0
60-m Buffer	0	0	0	14	5	2	0	0	4	25	0.56	0
Steep slope	0	0	0	1	50	0	0	0	10	61	0.8197	0
Riparian wetland	0	1	0	2	1	24	0	0	38	66	0.3636	0
Floodplain (wet)	1	3	1	2	0	29	86	8	16	146	0.5890	0
Terraces (wet)	0	0	0	0	0	0	0	0	0	0	0	0
Non-ARA	0	0	0	0	18	8	0	0	579	605	0.9570	0
Total	47	14	6	21	77	67	104	14	650	1000	0	0
P_Accuracy	0.9787	0.5	0	0.6667	0.6494	0.3582	0.8269	0	0.8907	0	0.806	0
Kappa	0	0	0	0	0	0	0	0	0	0	0	0.6647

D.1f: 5-m LiDAR DEM and 1:10,000 NBHN derived ARA

ARA components	Open water	Floodplain (non-wet)	Terraces (non-wet)	60-m Buffer	Steep slope	Riparian wetland	Floodplain (wet)	Terraces (wet)	Non-ARA	Total	U_Accuracy	Kappa
Openwater	46	2	0	0	1	0	2	0	0	51	0.9019	0
Floodplain (non-wet)	0	8	0	4	1	2	4	0	8	27	0.2963	0
Terraces (non-wet)	0	0	4	0	0	0	0	2	0	6	0.6667	0
60-m Buffer	0	0	0	9	5	0	0	0	0	14	0.6429	0
Steep slope	0	1	0	2	53	0	0	0	3	59	0.8983	0
Riparian wetland	0	0	0	4	0	26	0	1	61	92	0.2826	0
Floodplain (wet)	1	3	1	2	0	32	91	2	43	175	0.52	0
Terraces (wet)	0	0	1	0	0	6	7	9	1	24	0.375	0
Non-ARA	0	0	0	0	17	1	0	0	534	552	0.9674	0
Total	47	14	6	21	77	67	104	14	650	1000	0	0
P_Accuracy	0.9787	0.5714	0.6667	0.4286	0.6883	0.3881	0.875	0.6429	0.8215	0	0.78	0
Kappa	0	0	0	0	0	0	0	0	0	0	0	0.6387

D.1g: 3-m LiDAR DEM and 1:10,000 NBHN derived ARA

ARA components	Open water	Floodplain (non-wet)	Terraces (non-wet)	60-m Buffer	Steep slope	Riparian wetland	Floodplain (wet)	Terraces (wet)	Non-ARA	Total	U_Accuracy	Kappa
Openwater	47	0	0	0	0	0	0	0	0	47	1	0
Floodplain (non-wet)	0	10	0	5	2	1	0	0	12	30	0.3333	0
Terraces (non-wet)	0	0	4	0	0	0	0	0	0	4	1	0
60-m Buffer	0	0	0	9	1	0	0	0	0	10	0.9	0
Steep slope	0	0	0	0	37	0	0	0	0	37	1	0
Riparian wetland	0	0	0	3	0	20	0	1	83	107	0.1869	0
Floodplain (wet)	0	3	0	4	0	36	93	2	85	223	0.4170	0
Terraces (wet)	0	1	2	0	0	8	11	11	2	35	0.3143	0
Non-ARA	0	0	0	0	37	2	0	0	468	507	0.9231	0
Total	47	14	6	21	77	67	104	14	650	1000	0	0
P_Accuracy	1	0.7143	0.6667	0.4286	0.4805	0.2985	0.8942	0.7857	0.72	0	0.699	0
Kappa	0	0	0	0	0	0	0	0	0	0	0	0.5252

D.1h: 5-m smoothed LiDAR DEM and 1:10,000 NBHN derived ARA

ARA components	Open water	Floodplain (non-wet)	Terraces (non-wet)	60-m Buffer	Steep slope	Riparian wetland	Floodplain (wet)	Terraces (wet)	Non-ARA	Total	U_Accuracy	Kappa
Openwater	46	2	0	0	1	0	2	0	0	51	0.9019	0
Floodplain (non-wet)	0	7	0	0	2	0	2	0	0	11	0.6364	0
Terraces (non-wet)	0	1	4	0	1	0	0	2	0	8	0.5	0
60-m Buffer	0	0	0	16	5	3	0	0	1	25	0.64	0
Steep slope	0	1	0	2	50	2	0	0	13	68	0.7353	0
Riparian wetland	0	0	0	2	0	39	7	4	6	58	0.6724	0
Floodplain (wet)	1	3	1	1	0	5	85	0	0	96	0.8854	0
Terraces (wet)	0	0	0	0	0	1	6	8	0	15	0.5333	0
Non-ARA	0	0	1	0	18	17	2	0	630	668	0.9431	0
Total	47	14	6	21	77	67	104	14	650	1000	0	0
P_Accuracy	0.9787	0.5	0.6667	0.7619	0.6494	0.5821	0.8173	0.5714	0.9692	0	0.885	0
Kappa	0	0	0	0	0	0	0	0	0	0	0	0.7884

D.2 Miramichi River Basin Watershed

D.2a: 30-m SRTM DEM and 1:50,000 NHN derived ARA

ARA components	Open water	Floodplain (non-wet)	Terraces (non-wet)	60-m Buffer	Steep slope	Riparian wetland	Floodplain (wet)	Terraces (wet)	Non-ARA	Total	U_Accuracy	Kappa
Openwater	12	1	0	0	2	0	20	0	1	36	0.3333	0
Floodplain (non-wet)	1	4	2	5	2	14	50	14	10	102	0.0392	0
Terraces (non-wet)	0	0	0	0	0	0	0	0	0	0	0	0
60-m Buffer	0	0	0	8	2	3	4	0	14	31	0.2581	0
Steep slope	0	0	1	1	21	0	1	1	5	30	0.7	0
Riparian wetland	0	0	0	1	0	4	9	2	10	26	0.1538	0
Floodplain (wet)	0	0	0	0	0	0	0	0	0	0	0	0
Terraces (wet)	0	0	0	0	0	0	0	0	0	0	0	0
Non-ARA	2	0	2	10	38	45	29	4	645	775	0.8323	0
Total	15	5	5	25	65	66	113	21	685	1000	0	0
P_Accuracy	0.8	0.8	0	0.32	0.3231	0.0606	0	0	0.9416	0	0.694	0
Kappa	0	0	0	0	0	0	0	0	0	0	0	0.3399

D.2b: 30-m SRTM DEM and 1:10,000 NBHN derived ARA

ARA components	Open water	Floodplain (non-wet)	Terraces (non-wet)	60-m Buffer	Steep slope	Riparian wetland	Floodplain (wet)	Terraces (wet)	Non-ARA	Total	U_Accuracy	Kappa
Openwater	15	3	0	3	0	0	27	1	0	49	0.3061	0
Floodplain (non-wet)	0	0	2	0	0	3	8	4	1	18	0	0
Terraces (non-wet)	0	0	0	0	0	0	0	0	0	0	0	0
60-m Buffer	0	0	0	5	5	4	4	0	3	21	0.2380	0
Steep slope	0	0	0	2	32	0	1	0	14	49	0.6530	0
Riparian wetland	0	1	0	10	2	8	12	3	23	59	0.1355	0
Floodplain (wet)	0	1	3	5	1	9	37	13	3	72	0.5138	0
Terraces (wet)	0	0	0	0	0	0	0	0	0	0	0	0
Non-ARA	0	0	0	0	25	42	24	0	641	732	0.8756	0
Total	15	5	5	25	65	66	113	21	685	1000	0	0
P_Accuracy	1	0	0	0.2	0.4923	0.1212	0.3274	0	0.9357	0	0.738	0
Kappa	0	0	0	0	0	0	0	0	0	0	0	0.4564

D. 2c:30-m LiDAR DEM and 1:10,000 NBHN derived ARA

ARA components	Open water	Floodplain (non-wet)	Terraces (non-wet)	60-m Buffer	Steep slope	Riparian wetland	Floodplain (wet)	Terraces (wet)	Non-ARA	Total	U_Accuracy	Kappa
Openwater	15	1	0	3	3	1	28	0	0	51	0.2941	0
Floodplain (non-wet)	0	0	2	0	0	2	7	3	4	18	0	0
Terraces (non-wet)	0	0	0	0	0	0	0	0	0	0	0	0
60-m Buffer	0	0	0	8	3	1	1	0	6	19	0.4211	0
Steep slope	0	1	1	1	42	0	1	0	11	57	0.7368	0
Riparian wetland	0	0	0	7	0	22	6	0	31	66	0.3333	0
Floodplain (wet)	0	3	2	4	0	22	70	18	3	122	0.5738	0
Terraces (wet)	0	0	0	0	0	0	0	0	0	0	0	0
Non-ARA	0	0	0	2	17	18	0	0	630	667	0.9445	0
Total	15	5	5	25	65	66	113	21	685	1000	0	0
P_Accuracy	1	0	0	0.32	0.6462	0.3333	0.6195	0	0.9197	0	0.787	0
Kappa	0	0	0	0	0	0	0	0	0	0	0	0.5903

D. 2d:15-m LiDAR DEM and 1:10,000 NBHN derived ARA

ARA components	Open water	Floodplain (non-wet)	Terraces (non-wet)	60-m Buffer	Steep slope	Riparian wetland	Floodplain (wet)	Terraces (wet)	Non-ARA	Total	U_Accuracy	Kappa
Openwater	15	1	0	0	0	0	12	0	0	28	0.5357	0
Floodplain (non-wet)	0	0	3	0	0	3	1	4	4	15	0	0
Terraces (non-wet)	0	0	0	0	0	0	0	0	0	0	0	0
60-m Buffer	0	0	0	17	2	1	0	0	3	23	0.7391	0
Steep slope	0	0	0	2	43	1	1	0	7	54	0.7963	0
Riparian wetland	0	1	0	3	2	24	0	0	41	71	0.3380	0
Floodplain (wet)	0	3	2	3	0	25	99	17	6	155	0.6387	0
Terraces (wet)	0	0	0	0	0	0	0	0	0	0	0	0
Non-ARA	0	0	0	0	18	12	0	0	624	654	0.9541	0
Total	15	5	5	25	65	66	113	21	685	1000	0	0
P_Accuracy	1	0	0	0.68	0.6615	0.3636	0.8761	0	0.9109	0	0.822	0
Kappa	0	0	0	0	0	0	0	0	0	0	0	0.6611

D. 2e: 10-m LiDAR DEM and 1:10,000 NBHN derived ARA

ARA components	Open water	Floodplain (non-wet)	Terraces (non-wet)	60-m Buffer	Steep slope	Riparian wetland	Floodplain (wet)	Terraces (wet)	Non-ARA	Total	U_Accuracy	Kappa
Openwater	15	1	0	0	0	0	8	0	0	24	0.625	0
Floodplain (non-wet)	0	0	1	0	0	2	1	4	1	9	0	0
Terraces (non-wet)	0	0	0	0	0	0	0	0	0	0	0	0
60-m Buffer	0	0	0	18	2	1	0	0	3	24	0.75	0
Steep slope	0	0	0	1	45	0	1	0	5	52	0.8654	0
Riparian wetland	0	0	1	4	1	33	3	0	49	91	0.362637	0
Floodplain (wet)	0	4	2	2	0	25	100	17	9	159	0.6289	0
Terraces (wet)	0	0	0	0	0	0	0	0	0	0	0	0
Non-ARA	0	0	1	0	17	5	0	0	618	641	0.9641	0
Total	15	5	5	25	65	66	113	21	685	1000	0	0
P_Accuracy	1	0	0	0.72	0.6923	0.5	0.8849	0	0.9022	0	0.829	0
Kappa	0	0	0	0	0	0	0	0	0	0	0	0.6789

D. 2f: 5-m LiDAR DEM and 1:10,000 NBHN derived ARA

ARA components	Open water	Floodplain (non-wet)	Terraces (non-wet)	60-m Buffer	Steep slope	Riparian wetland	Floodplain (wet)	Terraces (wet)	Non-ARA	Total	U_Accuracy	Kappa
Openwater	15	0	0	0	0	0	2	0	0	17	0.8824	0
Floodplain (non-wet)	0	2	0	1	0	2	1	1	1	8	0.25	0
Terraces (non-wet)	0	0	3	0	0	1	0	2	1	7	0.4286	0
60-m Buffer	0	0	0	14	1	0	0	0	1	16	0.875	0
Steep slope	0	0	0	1	47	0	0	0	2	50	0.94	0
Riparian wetland	0	0	0	5	1	22	0	0	77	105	0.2095	0
Floodplain (wet)	0	3	0	3	0	35	107	10	43	201	0.5323	0
Terraces (wet)	0	0	1	0	0	3	3	8	0	15	0.5333	0
Non-ARA	0	0	1	1	16	3	0	0	560	581	0.9639	0
Total	15	5	5	25	65	66	113	21	685	1000	0	0
P_Accuracy	1	0.4	0.6	0.56	0.7231	0.3333	0.9469	0.3809	0.8175	0	0.778	0
Kappa	0	0	0	0	0	0	0	0	0	0	0	0.6092

D. 2g:3-m LiDAR DEM and 1:10,000 NBHN derived ARA

ARA components	Open water	Floodplain (non-wet)	Terraces (non-wet)	60-m Buffer	Steep slope	Riparian wetland	Floodplain (wet)	Terraces (wet)	Non-ARA	Total	U_Accuracy	Kappa
Openwater	15	0	0	0	0	0	0	0	0	15	1	0
Floodplain (non-wet)	0	5	0	3	0	3	3	0	3	17	0.2941	0
Terraces (non-wet)	0	0	3	0	0	0	0	2	0	5	0.6	0
60-m Buffer	0	0	0	15	4	1	0	0	0	20	0.75	0
Steep slope	0	0	0	0	29	0	0	0	0	29	1	0
Riparian wetland	0	0	0	2	0	15	1	0	93	111	0.1351	0
Floodplain (wet)	0	0	0	5	0	40	104	9	94	252	0.4127	0
Terraces (wet)	0	0	1	0	0	7	5	10	2	25	0.4	0
Non-ARA	0	0	1	0	32	0	0	0	493	526	0.9373	0
Total	15	5	5	25	65	66	113	21	685	1000	0	0
P_Accuracy	1	1	0.6	0.6	0.4462	0.2273	0.9204	0.4762	0.7197	0	0.689	0
Kappa	0	0	0	0	0	0	0	0	0	0	0	0.4822

D. 2h: 5-m smoothed LiDAR DEM and 1:10,000 NBHN derived ARA

ARA components	Open water	Floodplain (non-wet)	Terraces (non-wet)	60-m Buffer	Steep slope	Riparian wetland	Floodplain (wet)	Terraces (wet)	Non-ARA	Total	U_Accuracy	Kappa
Openwater	15	0	0	0	0	0	2	0	0	17	0.8823	0
Floodplain (non-wet)	0	2	1	0	0	0	1	1	0	5	0.4	0
Terraces (non-wet)	0	0	1	0	0	0	0	1	0	2	0.5	0
60-m Buffer	0	0	0	17	0	0	1	0	1	19	0.8947	0
Steep slope	0	1	0	2	51	0	1	0	9	64	0.7969	0
Riparian wetland	0	0	1	4	1	44	7	0	4	61	0.7213	0
Floodplain (wet)	0	2	0	1	0	5	100	7	0	115	0.8696	0
Terraces (wet)	0	0	1	0	0	0	1	12	0	14	0.8571	0
Non-ARA	0	0	1	1	13	17	0	0	671	703	0.9545	0
Total	15	5	5	25	65	66	113	21	685	1000	0	0
P_Accuracy	1	0.4	0.2	0.68	0.7846	0.6667	0.8849	0.5714	0.9796	0	0.913	0
Kappa	0	0	0	0	0	0	0	0	0	0	0	0.8247